COOLING SYSTEM DESIGN FOR ^{99}MO RESEARCH LOOP

Master's Thesis

Shridhar Pendse

Faculty of Applied Sciences
Chemical Engineering

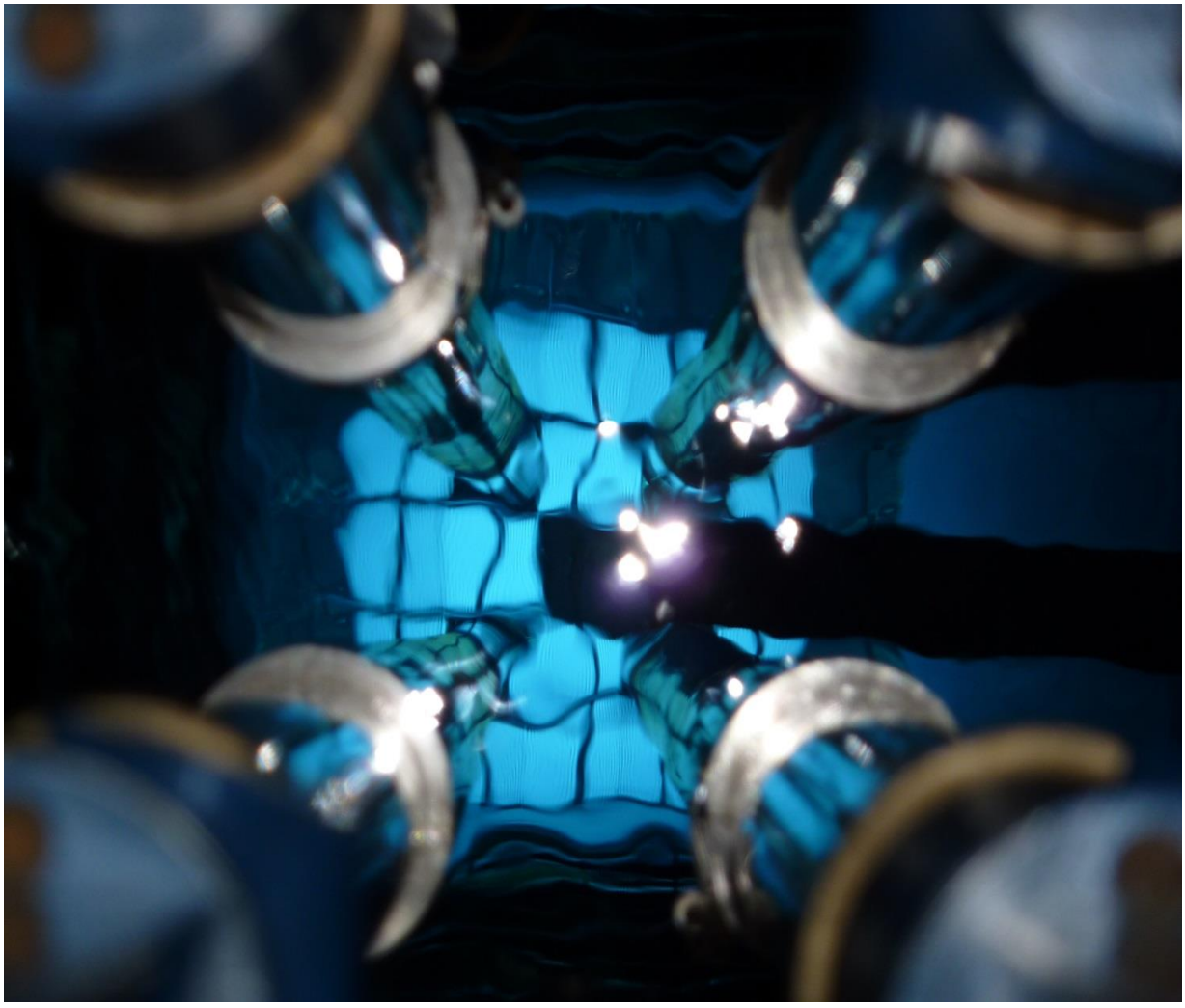

TU Delft

REACTOR INSTITUTE DELFT

COOLING SYSTEM DESIGN FOR ^{99}MO RESEARCH LOOP

By

Shridhar Pendse

Master's Thesis

in partial fulfillment of the requirements for the degree of

Master of Science
In Chemical Engineering

at the Delft University of Technology,
March 28th, 2018

Student number : 4616502
Supervisor : Dr. ir. Martin Rohde
Thesis committee : Dr.ir. Martin Rohde
: Prof. Dr. ir. Jan-Leen Kloosterman
: Dr. Sasa Kenjeres

TU Delft Delft University of Technology

Abstract

Molybdenum-99 is a radionuclide which decays into Technetium-99m. Technetium-99m is used in roughly 80% of medical diagnosis procedures. The current research focuses on the production of Molybdenum-99 in a small irradiation loop placed in the vicinity of Hoger Onderwijs reactor. The prior research states that up to 2.4 mg per week of ^{99}Mo production is possible in this loop, which roughly is 2.4 % of the world's total demand. However, heat transfer is a bottleneck for the ^{99}Mo yield from the irradiated production loop. Nuclear fission heat and gamma heat will result in the temperature of the aqueous solution exceeding its boiling point, leading to a potentially dangerous situation. Therefore, the research work focusses on enhancing the heat transfer process and cooling the loop down more effectively. The research was carried out by computational modelling of the irradiation loop and the cooling system in ANSYS Fluent software.

In an initial non-dimensional number analysis, it was verified that natural convection would be the dominating mechanism of heat transfer in an irradiation loop. However, before modelling the actual irradiation loop with the cooling system, the procedure of modelling natural convection in Fluent was validated with empirical correlation.

As natural convection inside the irradiation loop is a responsive process to temperature gradient, internal heat transfer coefficient of natural convection could limit the heat transfer by demanding larger gradient than the acceptable limit. Hence, a study was performed to ensure that the heat transfer coefficient inside the irradiation loop is not limiting the heat transfer. Along with that, a study was conducted to check the impact of uranium's concentration on limiting heat transfer coefficient using modified Rayleigh number.

For designing the cooling system, a simple shell and tube analogous cooling system without baffle's design was considered. CFD analysis of the system was carried out for varying flowrate of cooling fluid and based on that, an operating point was decided.

The irradiation loop in the initial study had a U-tube shape with a pump monitoring the flow from the open endings. It was decided to redesign the irradiation loop. In new setup, the pump was removed, and the open end of the tube were connected back to the inlet of the irradiation loop in a 180^{o} bend. In such an assembly, the flow field inside the irradiation loop will subject to the natural convection created by the temperature gradient. Like previous study, the CFD analysis of the new system was carried out for varying flowrate of cooling fluid, based on which an operating point for cooling system was envisaged.

To summarize, the thermal-hydraulic analysis showed that with a simple shell and tube type cooling system design an acceptable operational temperature distribution can be achieved in the envisaged irradiation loop.

Acknowledgements

I would first and foremost like to thank my supervisor, Dr. Martin Rohde for his guidance and direction and most importantly, for providing me the opportunity to conduct this research work at RPNM. I would also like to extend my gratitude to my immediate Ph.D. supervisor, M.S. Zheng Liu, who always supported me by sharing his knowhow of previous research work in this area.

It would be remiss of me to not acknowledge the immense help provided to me by M.S. Manu Chakkingal. His proficiency in Natural Convection helped me during my work. My thesis work would have been hampered had it not been for M.S. Dick De Haas's timely provision of his computer resources for my work for ANSYS Fluent. He also helped improve the system configuration per my requirement. I would also sincerely like to thank Prof. Dr. Jan-Leen Kloosterman and Dr. Sasa Kenjeres for taking valuable time off their busy schedule and agreeing to review my final defense.

Moreover, I would like to thank my friends - Kedar Pitke for his Skype discussions that helped me create user defined function for ANSYS in C++, Prasanna, Mehul, Yug and Meera for helping me in proofreading my thesis work. Finally, I would like to acknowledge the encouragement and unconditional support of my family and friends from Delft University, including my peers and colleagues from the RPNM department, without whose company this project would not have been as exciting as it has been.

Shridhar Pendse
Delft, March 2018

Contents

List of Table

List of Figure

Nomenclature

Symbol	Description	Units
A_c	Cross sectional area available for cooling fluid in DLDR	m^2
A_{cs}	Surface area of the cross section of the tube	m^2
A_w	Surface area of the wall interface	m^2
A_{wc}	Outer Surface area of the tube wall which is in contact with the cooling fluid	m^2
A_{wh}	Surface area of the Uranyl nitrate solution wall interface	m^2
Cp	Specific heat	$J.kg^{-1}.K^{-1}$
D	Diameter of tube / characteristic length of system	m
E_d	Energy density	$W.\ m^{-3}$
g	Gravitational acceleration	$m.s^{-2}$
H_v	Volume average heat production rate inside the irradiation loop	$W.m^{-3}$
h	Overall heat transfer coefficient	$W.m^{-2}.K^{-1}$
h_i	Internal heat transfer coefficient	$W.m^{-2}.K^{-1}$
h_e	external heat transfer coefficient	$W.m^{-2}.K^{-1}$
h_c	Heat transfer coefficient in the cooling fluid	$W.m^{-2}.K^{-1}$
$h_{i\_limiting}$	Limiting (Maximum) Internal heat transfer coefficient	$W.m^{-2}.K^{-1}$
k , κ	Thermal conductivity	$W.m^{-1}.K^{-1}$
l	Characteristic length	m
N	Density of uranium nucleus	$\#.m^{-3}$
P_n	Power production	W
ΔP	Pressure drop in across the cooling domain /DLDR	Pa
P	Pressure	Pa
q"	Heat flux coming out from the surface of the domain	$W.m^{-2}$
q''_{wc}	Total heat flux coming out from outer surface of tube wall	$W.m^{-2}$
q'''	heat production rate per unit volume	$W.m^{-3}$
q''_{wh}	Total heat flux coming out from the Uranyl nitrate solution	$W.m^{-2}$
r	Radius of the tube	m
R	Rate of fission reaction	$W.m^{-1}$
R^2	Coefficient of determination	
T	Temperature	K
T_m , T_b	Mean Temperature in the domain	K
T_∞	Temperature of the surrounding	K
T_c	Volume average temperature of cooling fluid	K

T_{Cin}	Cooling fluid temperature at the inlet nozzle	K
$T_{c\,out}$	Bulk temperature of the cooling fluid at the outlet nozzle	K
T_h	Volume average temperature of Uranyl nitrate solution	K
$T_{\max}$	Maximum temperature inside at the setup	K
$\Delta T_{\max}$	Temperature difference between the cold fluid and the hot spot in the domain	K
T_w	Average temperature over wall interface	K
T_{wc}	Average temperature over irradiation loop's outer wall interface	K
T_{wh}	Average temperature over the Uranyl nitrate solution's wall interface	K
t_z	Thickness of zircaloy wall	m
u_x	x-velocity	$m.s^{-1}$
u_y	y-velocity	$m.s^{-1}$
u_z	z-velocity	$m.s^{-1}$
u_{cin}	Cooling fluid average velocity at the inlet nozzle	$m.s^{-1}$
V	Volume of the domain	m^3
x	x- direction	
y	y- direction	
z	z- direction	
α	Thermal diffusivity	$m^2.s^{-1}$
β	Thermal expansion factor	
ε	Level of enrichment	
μ	Dynamic viscosity	$kg.m^{-1}.s^{-1}$
ν	Kinematic viscosity	$m^2.s^{-1}$
ρ	Density of material	$kg.m^{-3}$
σ	Microscopic Neutron cross section	b (10^{-28} m^2)
ϕ_n	Neutron Flux	$\#.m^{-2}.s^{-1}$
ϕ_i	Volumetric flowrate	$m^3.s^{-1}$
ϕ_c	Flowrate of cooling fluid	$m^3.h^{-1}$

Non-Dimensional numbers

$Bi_S = \frac{h_e}{h_{i\_\text{limiting}}}$	Specific Biot Number	$Gr = \frac{g\beta(T_b - T_w)D^3}{\nu^2}$	Grashof number
$Nu = \frac{hl}{k}$	Nusselt Number	$\Pr = \frac{\mu Cp}{k}$	Prandtl number
$Ra = \frac{g\beta(T_b - T_w)D^3}{\nu\alpha}$	Rayleigh Number	$Ra_M = \frac{g\beta H_v D^5}{\kappa\nu\alpha}$	Modified Rayleigh number

$\mathrm{Re} = \frac{\rho u D}{\mu} = \frac{\phi_c D_o \rho}{\mu A_c}$ Reynolds number $Ri = \frac{Gr}{\mathrm{Re}^2}$ Richardson number

Chapter 1

INTRODUCTION

The radioactive isotope Molybdenum-99 (^{99}Mo) naturally decays into Technetium-99m. Technetium-99m is a radionuclide used in medical diagnosis. The traditional way of producing Molybdenum-99 is from irradiation of Uranium-235. From its production facility to its medical diagnosis centre, the traditional transportation process reduces the overall production efficiency of Molybdenum-99 to overcome this transport limitation, a continuous production technique is under study.

Currently, an irradiated loop of an aqueous solution of uranyl nitrate placed inside Hoger onderwijs reactor is under investigation. A continuous process for production and extraction of ^{99}Mo using the neutron flux from Hoger onderwijs reactor (HOR) is developed and studied in prior study. However, heat transfer is a bottleneck for the ^{99}Mo yield from the irradiated production loop. Nuclear fission heat and gamma heating will result in the temperature of the aqueous solution exceeding its boiling point, leading to a potentially dangerous situation. Therefore, the research carried out in the thesis focussed on enhancing the heat transfer process and cooling the loop down more effectively.

1.1 Why Molybdenum 99?

The radioactive Isotope of Molybdenum with atomic number 99 naturally decays to Technetium-99. About 88% of ^{99}Mo decays in to a metastable isomer of Technetium (^{99m}Tc). Technetium-99m decays mainly by emissions of gamma rays into a stable isomer Technetium-99. Energetic gamma radiation (140 keV) emitted by Technetium-99m can be picked by the Gamma cameras. Gamma emission is a desirable property of medical isotopes as other emissions can have higher energies which can harm patients' body. Also, the half-life of metastable Technetium-99 is just 6.0058 hours, making it the perfect radioactive tracer for medical diagnosis as the short half-life ensures a rapid data collection and at the same time, shorter exposure of patient's body to radiation. (1)

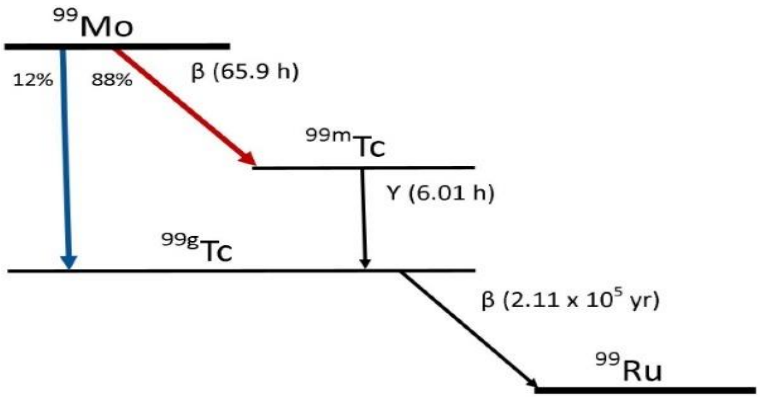

Figure 1-1 ^{99}Mo decay chain (1)

1.1.1 Conventional process of Isotope production to patient

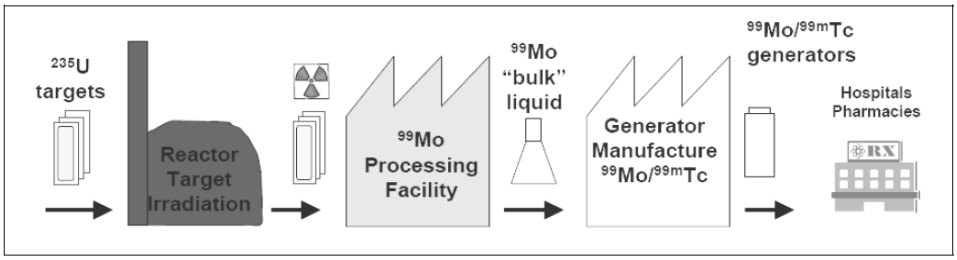

Figure 1-2 Molybdenum-99 production and supply chain (2)

Currently over 95% of the world's demand of ^{99}Mo is produced by nuclear fission of Uranium-235 (3). Either highly enriched or low enriched Uranium-235 targets are irradiated by the neutron flux for 6 to 7 days. The irradiated targets are cooled and shipped for further processing. This takes around 16 hours (4). Generally, further processing facility is built nearby to minimize loss of isotope during transport. Usually this transport takes around 2 to 3 hours. At the isotope processing facility, the ^{99}Mo is separated from the rest of the isotopes. The separation of ^{99}Mo takes around 12 hours. About 6.13% of every nuclear fission reaction produces ^{99}Mo. Extracted ^{99}Mo is in the form of liquid which is then further transported to a generator manufacturing facility, which can take about 36 hours. At the generator plants, ^{99}Mo is absorbed on the Alumina column. This preparation can take up to one day and so does the transport of these generators to hospitals. At the hospital, ^{99m}Tc doses are prepared from the generators for medical imaging and other uses. Usually once brought at the hospital, one generator can last for around 2 weeks (4).

1.1.2 Interruption in ^{99}Mo- ^{99m}Tc supply

There is a weekly worldwide demand of ^{99}Mo of around 12,000 6-day Curie (4). Molybdenum-99 and Technetium-99m both have a very short half-life and therefore cannot be stockpiled. Hence, Molybdenum-99 needs to be generated and delivered on a regular weekly basis. The supply of molybdenum globally relies on a small number of suppliers. As noted in Table 1-1 most of these reactors are very old. As the supply depends on only few reactors, ^{99}Mo supply and production has been interrupted several times by the unforeseen shutdown of these old reactors. Moreover, none of these reactors are entirely dedicated for production of ^{99}Mo and any other radioisotopes. They provide various services as per the users' requirements. These complications have indeed lead to a need of small scale production unit's catering to local demands.

Table 1-1 Major suppliers of Molybdenum-99 (1)

Country	Reactor	Start of Operation	Power (MW)
Belgium	BR-2	1961	100
Netherlands	HFR	1961	45
Czech Republic	LVR-15	1957	10
Poland	Maria	1974	30
Australia	OPAL	2006	20
South Africa	SAFARI-1	1965	20

1.2 Current Research and Literature Survey

The current research studies the feasibility of building an innovative technique of medical isotope production. A small loop filled with uranium salts' aqueous solution shall be placed in the irradiation zone of an existing facility, where the neutron flux from the existing reactor core facilitates the fission reaction inside the loop. Nuclear fission reaction would lead to the formation of medical isotopes which could be extracted from the facility.

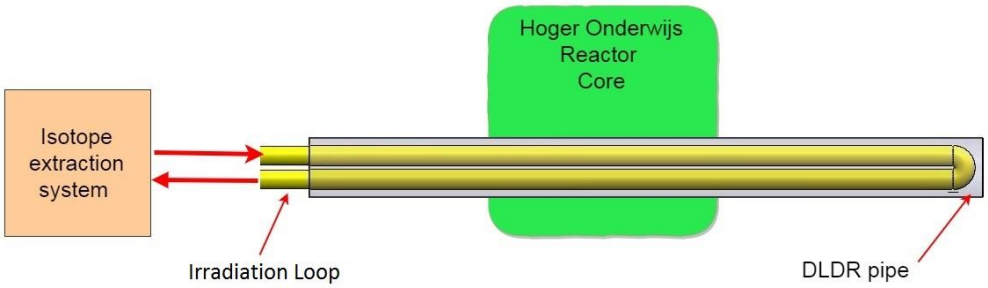

Figure 1-3 Concept drawing of the reactor setup

Kenneth Elgin's (4) studied the feasibility of a U-tube shaped small loop filled with low enriched Uranium. As per his studies, the U-tube shall be placed in the existing DLDR pipe near the Hoger Onderwijs Reactor core, where it will be irradiated with the neutron flux from the Reactor core, leading to a fission chain reaction and the production of ^{99}Mo and other isotopes. Elgin also confirmed for an irradiation cycle of three hours over the reactor loop with a Uranium concentration of 310 g U.L^{-1} and U-235 enrichment of 19.75 % (LEU), a maximum yield of 2.73 mg of ^{99}Mo per week is possible. This is around 2.4% of the weekly world demand. He also analyzed few characteristics of the setup to optimize its performance. It can be seen in Table 1-2

Table 1-2 Kenneth Elgin's findings on the performance of the reactor (4)

Topics	Findings	Conclusions & Recommendations
Impact of irradiation time	It is seen that the rate of fission increases with increasing the irradiation time. However, increasing the irradiation time decreases ^{99}Mo concentration as it naturally decays.	Due to limitation of ^{99}Mo extraction method, a minimum irradiation time of 3 hours is selected as the irradiation time for the irradiation loop.
Impact of the orientation on the irradiation loop	Three different orientations of the irradiation loop with respect to the reactor core or neutron flux were compared to check its impact on the reactor core. It was seen that for more evenly distributed irradiation time, the production of ^{99}Mo increases.	An orientation which will give even distribution of neutron flux over the U-tube should be selected. Hence, the irradiation loop should be placed normal to the direction of the flux, i.e. the two-cylindrical tube shall be placed on top of the each-other, perpendicular to neutron core.

Effect of the salt concentration of the inlet flow on ^{99}Mo production	It was found that an increase in the amount of Uranium in the salt solution leads to an increase in ^{99}Mo production.	Any increase in concentration of ^{99}Mo shall increase the fission reaction. However, the heat produced by the rate of fission & methodology of ^{99}Mo extraction can be limiting for increasing concentration of Uranium.

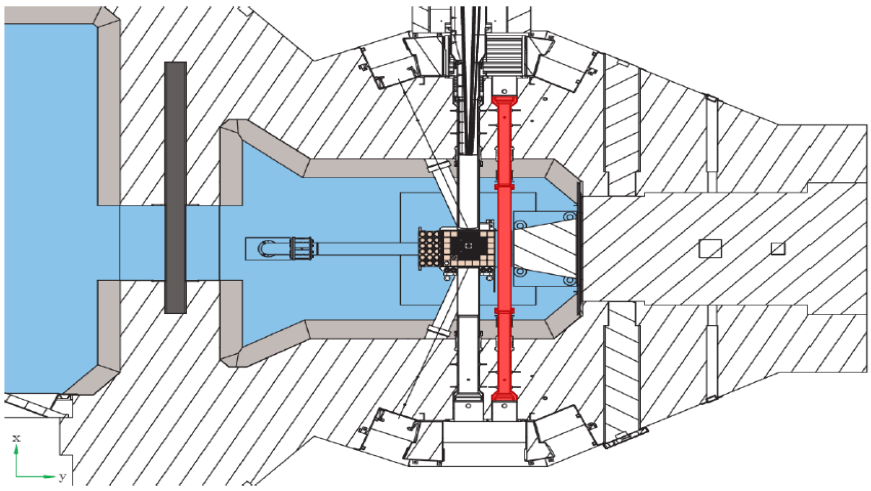

Figure 1-4 Schematic top view of reactor core and pool the U-tube shall be placed inside DLDR pipe highlighted in RED (4)

Huisman preceded Elgin's work, (5) and during his research, he studied heat production & heat transfer by natural convection inside the irradiation loop. He estimated total heat production of 7.87 kW for a concentration of 310 gU.L^{-1} via nuclear fission reaction by analyzing the system in MCNP. Huisman confirmed the material of construction of loop and the safety barrier. Due to very high acidity of Uranyl nitrate solution, irradiation loop would be made up of Zircaloy (Zirconium alloy). During his work, Huisman added an extra tube (indicated in Red in Figure 1-5) outside the U- tube as a flood barrier which will contain any leakage in irradiation loop. This tube is closed at one end and covers the whole DLDR along with the irradiation loop. One of the concerns which Huisman highlighted was regarding heat transfer from the irradiation loop. Moreover, he concluded that only natural convection as the cooling mechanism in the DLDR is not sufficient to cater the heat produced in the irradiation loop without creating any hot spot of more than 100^{o}C. As per his study, the irradiation loop setup working only on natural convection for external cooling will operate below the boiling point of water only if the maximum concentration of Uranium in the loop is 27.6 gU.L^{-1}.

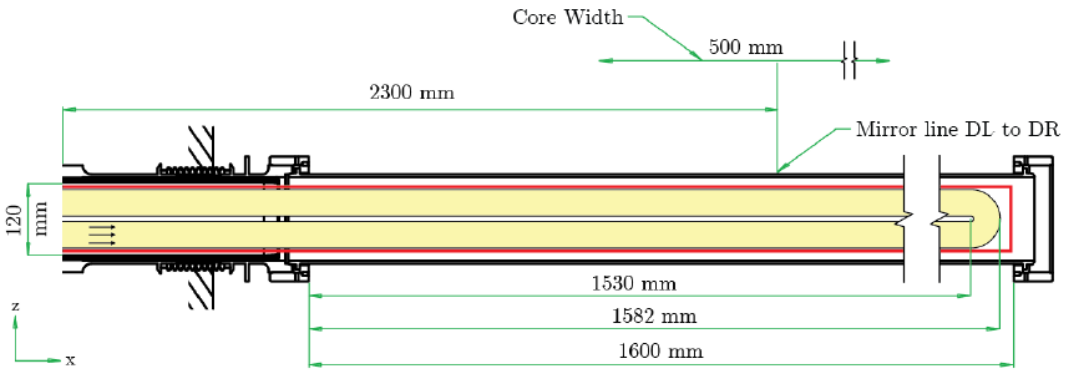

Figure 1-5 Geometry of setup studied by Huisman (5)

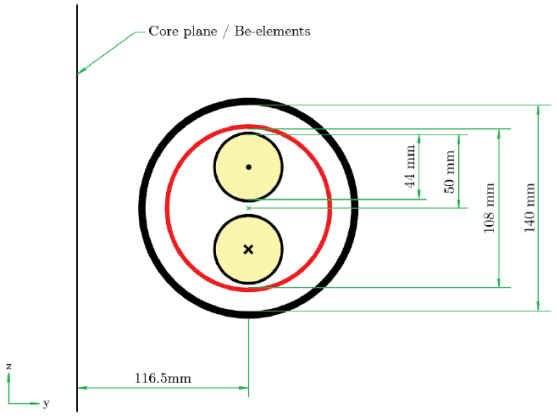

Figure 1-6 Cross sectional geometry of setup studied by Huisman (5)

Egmond studied (6) the impact of temperature rise on the neutron flux and perpetually on the rate of fission. He concluded that the temperature rise inside the loop impacts slightly but inversely to the rise of heat production. Hence for a conservative approach, the impact of rising temperature on the neutron flux and rate of reaction can be neglected.

During all the studies listed above, it was assumed that the concentration inside the loop shall not vary over time. However, in practice, complete fission of all the U-235 inside the loop does not happen in a single cycle. Hence in her research work, Pothoven (7) studied the long-term behavior of the loop content when flow inside the loop is recirculated. Pothoven concluded that the loop could work for 22 years with a mere turndown of 80% to the original starting production rate.

Huisman in his work highlighted the concern regarding heat transfer from the irradiation loop setup. A complete system dependent on natural convection for heat transfer from the irradiation loop to the water pool will create a situation in which the temperature inside the irradiation loop would rise above the boiling point of water. Hence it was decided to apply external cooling mechanism over the entire irradiation loop such that heat produced by nuclear fission and by gamma deposition can be effectively removed and the temperature inside the irradiation loop can be maintained below boiling point of water. In this work, a cooling mechanism over the irradiation loop setup will be designed and optimized by computational fluid dynamics (CFD) in ANSYS fluent 18.1.

Chapter 2

THEORY & UNDERSTANDING OF THE SYSTEM

This chapter starts with an overview of the irradiation loop setup and different heat sources, followed by a summary of the physics used for solving the problem along with the numerical procedures. In last part, an initial analysis of the problem was carried out.

2.1 Irradiation loop setup

Figure 2-1 gives a schematic illustration of the positioning of DLDR beam-tube's central part (in yellow) in the existing Hoger Onderwijs Reactor. The U-tube (irradiation loop) would be placed vertically inside the DLDR beam such that both the legs of the tube would be facing equal neutron flux from the core. As it could be seen in the picture DLDR's beam tube runs through the water pool in front of the HOR Core and has supporting part's in the concreate structures which are made of iron alloys. However, the central part of DLDR is an aluminum alloy pipe of 0.14m diameter, 1.6m length and 5mm thick walls (5). For modelling and ease of understanding throughout the report it was assumed that the irradiation loop is parallel to the x-axis and gravity is acting along the negative y-axis.

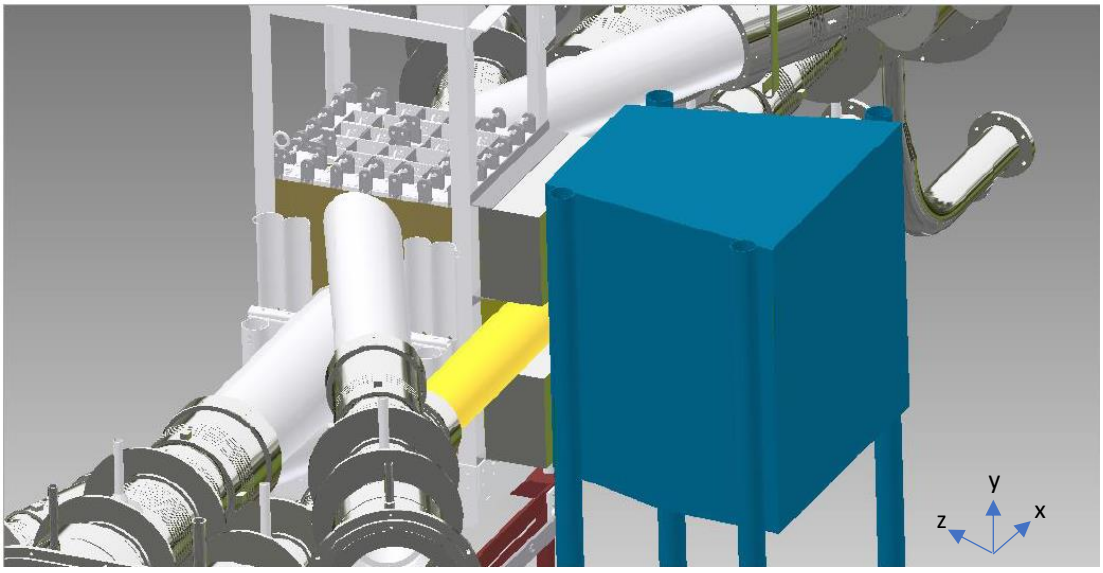

Figure 2-1 DLDR positioning in Hoger Onderwijs Reactor (4)

2.2 Heat generation inside the irradiation loop setup

There are three sources of heat inside the irradiation loop setup. The primary heat source is the nuclear fission of Uranium-235 nuclei. The second source of heat is the heat deposition by the gamma flux approaching from the HOR core. The gamma radiation coming from HOR reactor deposits significant heat over the aluminum and Zircaloy walls of DLDR and irradiation loop. The third source of heat is envisaged from the outer surface of DLDR, the liquid pool outside DLDR is at higher temperature then the coolant anticipated for the process, this temperature difference will lead to some heat flux from the DLDR beam tube's wall.

2.2.1 Heat generation inside the loop by nuclear fission

Nuclear fission of a single uranium nucleus releases around 200 MeV of energy. The total heat production inside the irradiation loop by fission can simply be calculated by calculating the occurrence of each fission reaction and then multiplying it with the typical fission heat. The occurrence of fission reaction depends upon the neutron flux, neutron interaction cross section of the nuclei and the number density of that nucleus in the domain. Duderstadt (8) defines the reaction rate as:

$$R = \varepsilon.\sigma.\phi_n.N \qquad (2.1)$$

Where ε is the level of enrichment

ϕ_n is Neutron flux. ($m^{-2}.s^{-1}$)

N is density of uranium nucleus (#.m^{-3})

σ is microscopic neutron cross section (b)

During earlier studies, August Winkelman (RID, HOR-development) calculated the neutron flux over the setup using the Monte Carlo N-particle 6.1 code (MCNP6.1) developed by the Los Alamos Laboratory. The MCNP6.1 output gave the neutron flux profile over the loop. It was observed that the neutron flux varies slightly due to the self-shielding effect of uranium nitrate solution in the y & z direction or over the cross section (normal to flux) of the loop. For ease of calculation it was decided to assume uniform neutron flux over the cross section normal to the flux of irradiation loop i.e. y & z direction (5). However, over the x-direction the change in flux is significant. Figure 2.1 shows the Gaussian distribution of neutron flux over the x-axis. The different colored line in the figure represents the different energy levels of neutron flux. The heat production inside the irradiation loop will occur mostly by the nuclear fission of U-235 by thermal neutron that is the neutron with energy level from 0 to 625 eV (shown by the blue line in Figure 2-2).

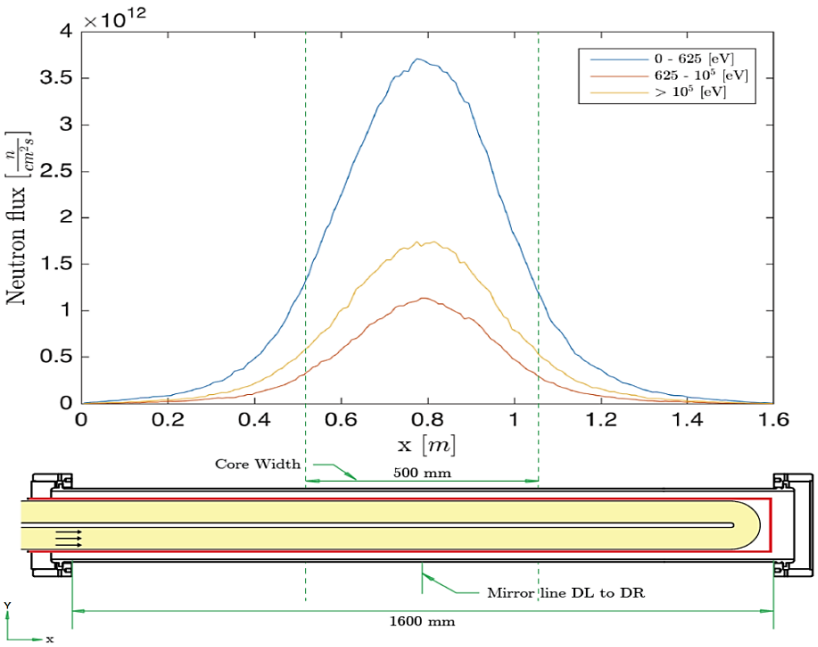

Figure 2-2 Neutron flux profile in the x-direction (5)

Figure 2-3 gives the energy generation profile calculated by Huisman. It is assumed for all time the solution shall remain perfectly mixed with uranium nuclei. As discussed earlier the heat generation inside the irradiation loop shall vary depending upon the neutron flux, neutrons interaction cross section and the number density of Uranium nucleus. Which means the heat production inside the reactor by nuclear fission can be controlled varying the Uranium concentration. The MCNP approach predicted for a irradiation loop filled with uranium nitrate solution at 310 $gU.L^{-1}$ concentration, the total heat production due to nuclear fission would be 7870 W.

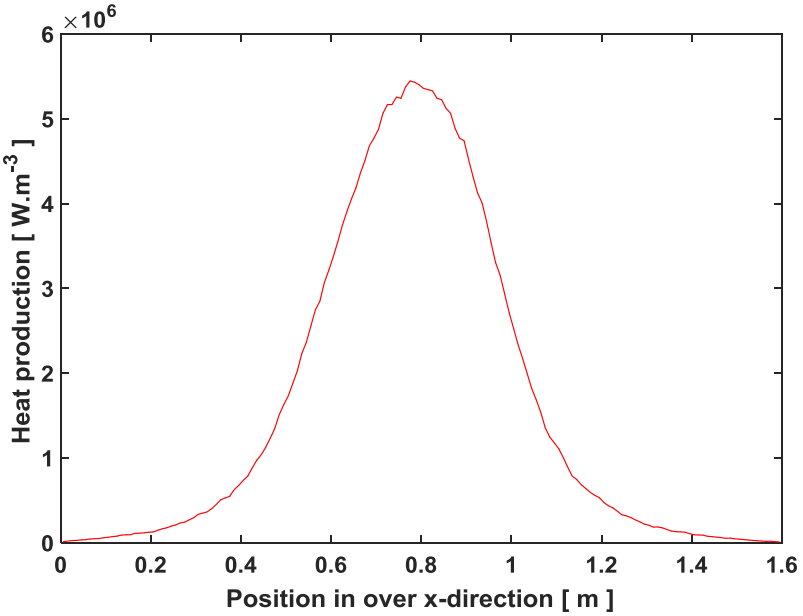

Figure 2-3 Heat production profile over irradiation loop (5)

2.2.2 Heat deposition by gamma flux

Second source of heat is the gamma radiation which interacts with the construction material of irradiation loop and DLDR beam. The absorption of gamma radiation results in deposition of energy into the material, which will increase material temperature. Like nuclear fission heat MCNP was used to calculate gamma heating over the construction material. Figure 2-4 gives gamma heat distribution over the x-direction of the irradiation loop. Like neutron flux, gamma radiation is also assumed to have a very low shielding effect by the feed solution. Hence it is anticipated to be uniform in y & z direction (cross section normal to x-axis).

The power distribution by gamma radiation over the irradiation loop and the DLDR beam can be calculated using equation 2.2 (5)

$$P_n = \iiint_V E_d \rho . dxdydz \qquad (2.2)$$

P_n is power production in [W]

E_d is the energy density calculated by MCNP simulation [$W.m^{-3}$]

ρ is density of material of construction [$kg.m^{-3}$]

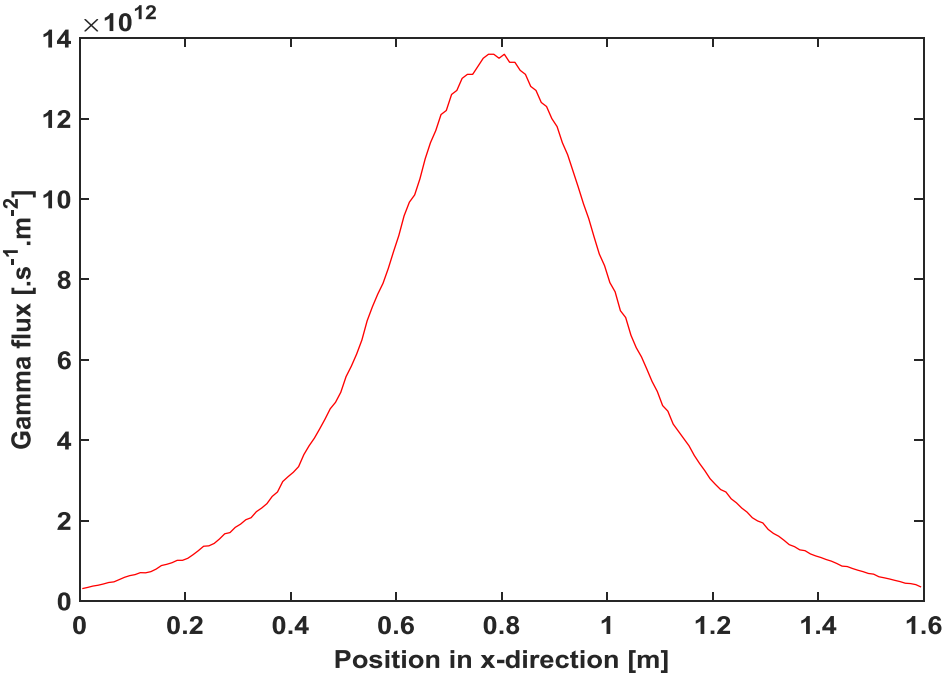

Figure 2-4 Gamma flux distribution over irradiation loop (5)

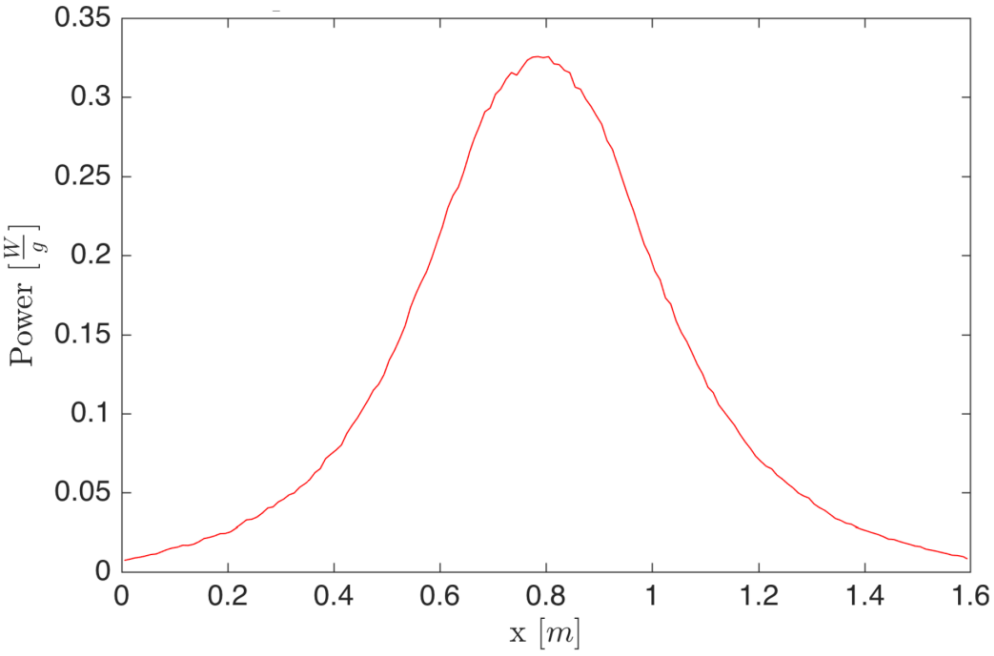

Figure 2-5 Gamma heat deposition over the construction material (5)

2.2.3 Heat gain from water pool

For neutron flux moderation and to control the temperature of the HOR reactor assembly, the HOR reactor core and the DLDR both are kept inside a water pool. The temperature of the water pool is maintained at 313K. However, the temperature of the coolant envisaged to flow inside DLDR would be

less. This temperature difference will result in natural convective flow which would transfer some heat from the water pool to DLDR wall.

2.3 Governing equations

Heat transfer, mass transfer and energy transfer are mutually dependent phenomena. The laws of transport phenomena link's them by the mass, energy, and momentum conservation equations. The temperature and flow distribution inside the irradiation loop can be determined by solving all conservation equation concurrently.

2.3.1 Continuity equation

The Continuity equation ensures that the total mass of fluid would be conserved.

$$\frac{\partial \rho}{\partial t}+\frac{\partial}{\partial x}(\rho u_x)+\frac{\partial}{\partial y}(\rho u_y)+\frac{\partial}{\partial z}(\rho u_z)=0 \qquad (2.3)$$

Where ρ is the density, u_x, u_y, u_z are the velocity components in x, y & z directions.

2.3.2 Navier-Stokes equation

Equation 2.4, 2.5 & 2.6 are the Navier-Stokes equations which ensure the momentum is conserved. In other words, solving the Navier-Stokes equation is balancing all the forces inside the fluid domain.

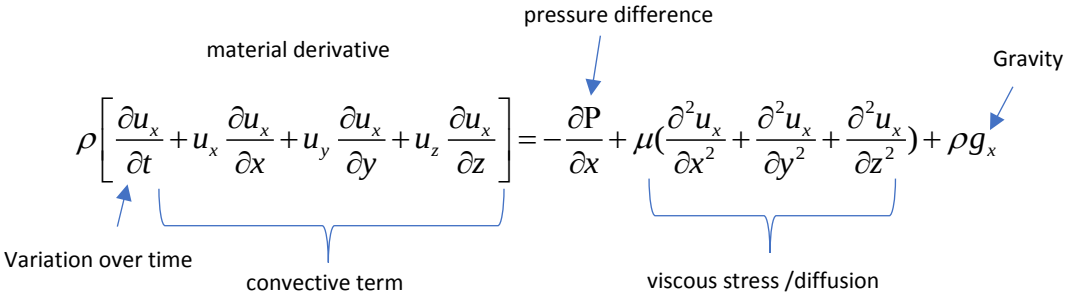

$$\rho\left[\frac{\partial u_x}{\partial t}+u_x\frac{\partial u_x}{\partial x}+u_y\frac{\partial u_x}{\partial y}+u_z\frac{\partial u_x}{\partial z}\right]=-\frac{\partial P}{\partial x}+\mu\left(\frac{\partial^2 u_x}{\partial x^2}+\frac{\partial^2 u_x}{\partial y^2}+\frac{\partial^2 u_x}{\partial z^2}\right)+\rho g_x$$

X-component (equation 2.4)

$$\rho\left[\frac{\partial u_y}{\partial t}+u_x\frac{\partial u_y}{\partial x}+u_y\frac{\partial u_y}{\partial y}+u_z\frac{\partial u_y}{\partial z}\right]=-\frac{\partial P}{\partial y}+\mu\left(\frac{\partial^2 u_y}{\partial x^2}+\frac{\partial^2 u_y}{\partial y^2}+\frac{\partial^2 u_y}{\partial z^2}\right)+\rho g_y$$

Y-component (equation 2.5)

$$\rho\left[\frac{\partial u_z}{\partial t}+u_x\frac{\partial u_z}{\partial x}+u_y\frac{\partial u_z}{\partial y}+u_z\frac{\partial u_z}{\partial z}\right]=-\frac{\partial P}{\partial z}+\mu\left(\frac{\partial^2 u_z}{\partial x^2}+\frac{\partial^2 u_z}{\partial y^2}+\frac{\partial^2 u_z}{\partial z^2}\right)+\rho g_z$$

Z-component (equation 2.6)

2.3.3 Conservation of Energy

Equation 2.7 gives the internal energy balance inside a system

$$\frac{\partial T}{\partial t}+u_x\frac{\partial T}{\partial x}+u_y\frac{\partial T}{\partial y}+u_z\frac{\partial T}{\partial z}=\alpha\left(\frac{\partial^2 T}{\partial x^2}+\frac{\partial^2 T}{\partial y^2}+\frac{\partial^2 T}{\partial z^2}\right)+\frac{H_v}{\rho.C_p} \qquad (2.7)$$

Here T is the temperature of fluid in K, α is the thermal diffusivity $m^2.s^{-1}$, C_P is specific heat in $J.kg^{-1}.K^{-1}$ and H_V Is the heat generation in $W.m^{-3}$.

2.4 Computational fluid dynamics

Velocity and temperature fields inside the domain can be calculated by solving all conservation equation simultaneously. For simple geometries, these equations are solved analytically by finding similarities and by reducing the number of dimension's. However, for a complex geometry such as researched irradiation loops these equation needs to be solved numerically.

In a numerical approach, the partial differential equations are solved by discretizing the domain into finite volumes or points and then by applying the partial differential equations in the form of algebraic equations to each of the discretized fractions. These algebraic equations are then solved numerically. (9)

It was decided to use ANSYS Fluent academic research version 18.1 software package to solve all the conservation equation numerically. ANSYS Fluent can be used to model flow, turbulence, heat transfer, species transport and reactions phenomenon using the inbuilt solvers (10).

Figure 2-7 illustrates the steps followed for carrying out for all the CFD calculation performed in this report. Physical model for each simulation were built in SolidWorks software and then exported to ANSYS workbench. Meshing or grid discretization of the setup was carried out in workbench default software design modular. Later the mesh was exported to ANSYS Fluent where the numerical calculation was performed for defined constrained and physical properties.

2.5 Analysis of the problem

Figure 2.6 shows the cross-sectional view of the system studied by Huisman. Huisman studied the system with natural convection in domain-3 driving the heat transfer to the surrounding water pool. However, cooling mechanism based on natural convection was limiting heat transfer, hence it was decided to use forced convection in domain-3. The required heat transfer mechanism can be provided over the surface of safety barrier using a cooling fluid like water.

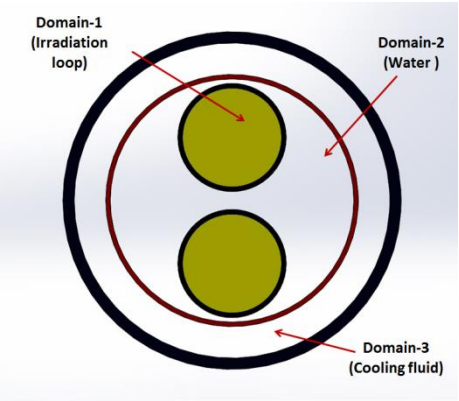

Figure 2-6 cross sectional view of setup

In such setup, due to heat generated by the nuclear fission the temperature of the solution inside the irradiation loop will start to rise. However, the tube wall due to presents of the coolant would be at lower temperature compared to the core. This temperature difference would create density difference between the fluid at wall surface and at loop core. Non-dimensional Rayleigh number is the ratio of buoyant force to the viscous force multiplied by the ratio of movement and thermal diffusivity. For any system, the increase in temperature difference will increase the buoyant force and at certain critical point, the buoyant force will start to impact the flow. i.e. the flow regime will show deviation in flow due to the temperature difference. This is identified by the critical Rayleigh number.

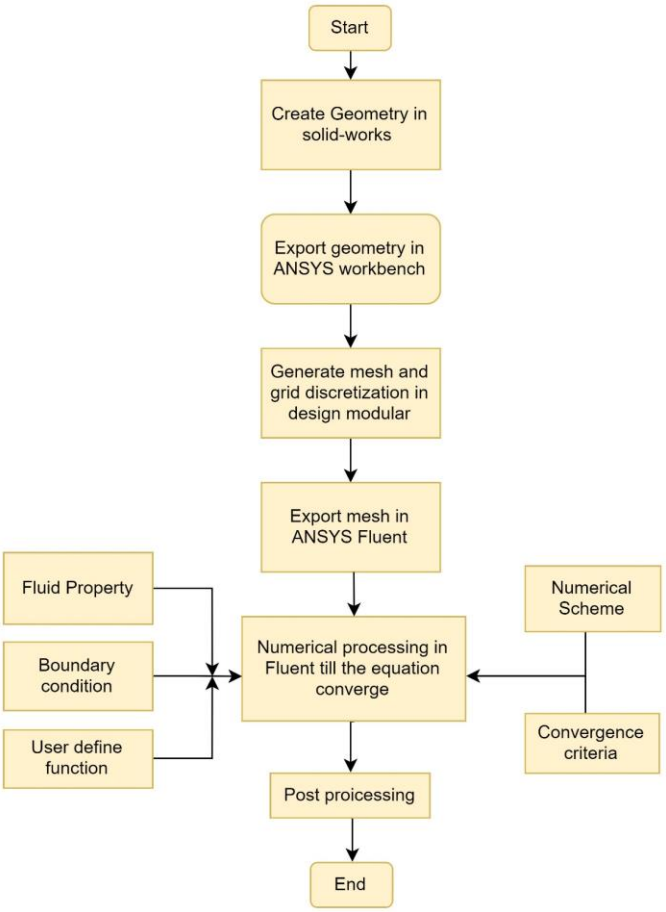

Figure 2-7 Flowchart of process followed for modelling

Rayleigh number can be calculated by equation 2.8.

$$Ra = \frac{g\beta(T_b - T_w)D^3}{\nu\alpha} \qquad (2.8)$$

Where Ra is the Rayleigh number, g is gravitational constant, β is thermal expansion coefficient, D characteristic length (inner diameter of irradiation loop), ν is kinematic viscosity, α is thermal diffusivity and $(T_b - T_w)$ is the temperature difference between bulk fluid and the walls of irradiation loop.

For an assumed temperature difference of 10 ^{0}C the Rayleigh number inside the irradiation loop is 2.82 x 10^7, which is very high compared to the critical Rayleigh number of 1708 (11) from which the Rayleigh-Bernard convection occurs between two horizontal infinite parallel plates.

Forced convection vs Natural convection inside the irradiation loop

Inside the irradiation loop the pump drives the flow to maintain a irradiation time of 3 hrs in the axial direction. As gravity is acting downward the buoyant force would act perpendicular to the axial flow forced by the pump. This transverse flow pattern would enhance the overall heat transfer inside irradiation loop. The degree of impact of each mechanism can be studied by the non-dimensional analysis.

The Richardson number (Ri) is the ratio of Grashof number to the square of Reynolds number in the forced convection. It is used to check the dominance of natural convection over forced convection. If the Richardson number is less than 1, definition of Ri indicates forced convection dominates the heat transfer and natural convection can be neglected whereas if Ri is greater than 10 then natural convection dominates and forced convection can be neglected. (12)

Inside the irradiation loop for uranyl nitrate solution, for assumed 10 ^{0}C temperature difference between the loop wall and core, the Grashof number is 5.17 x10^6. Also for the irradiation time of 3 hours the calculated Reynolds number is 13.99. From this the Richardson number calculated is of the order of 10^4, which is very high and indicates natural or free convection shall dominate the flow field and will be the dominating mechanism for heat transfer from the irradiation loop.

$$Gr = \frac{g\beta(T_b - T_w)D^3}{\nu^2} = Ra.\Pr = 5.17\times10^6 \qquad (2.9)$$

$$\mathrm{Re} = \frac{\rho.u.D}{\mu} = 13.99 \qquad (2.10)$$

Table 2-1 Initial non-dimensional analysis of the system

Non-dimensional number	Criteria	Result
$Ra = \frac{g\beta(T_b - T_w)D^3}{\nu\alpha} = 2.82\times10^7$	If Ra > 1708 Temperature gradient shall affect the flow field.	Transverse flow would be seen in the irradiation loop.
$Ri = \frac{Gr}{\mathrm{Re}^2} = 2.64\times10^4$	Ri < 1 Forced convection 10 > Ri > 1 Mixed convection Ri >> 10 Free convection	Natural convection would be the dominating mechanism for heat transfer inside the irradiation loop.

Chapter 3

Modelling Natural Convection

In chapter 2, we understood internal heat generation would create natural convective transverse flow within the irradiation loop. Moreover, the natural convection would be the dominating mechanism for heat transfer. Hence, the flow inside the irradiation loop should be modelled such that the natural convection can be simulated. However, before actual modelling of the whole system, it was decided to confirm the modelling technique. In this chapter, a simple system is modelled where the simulation results can be verified by an empirical correlation available in the literature.

Natural Convection can be modelled in the ANSYS Fluent using the Boussinesq approximation. In the Boussinesq approximation, the impact of a density change by a temperature gradient is only applied where the density change impacts the gravitational force.

3.1 Theory

In a system where the temperature change impacts the force balance and eventually impacts the flow field, Boussinesq approximation can be used to simulate such phenomenon. For modelling natural convection Boussinesq approximation assumes following (13)

1. *Any variation in physical properties other than density would be ignored. Moreover, the Impact of density change in the continuity or in the energy equation will be ignored*. Hence, equation 2.3 will reduce to equation 3.1

$$\frac{\partial u_x}{\partial x}+\frac{\partial u_y}{\partial y}+\frac{\partial u_z}{\partial z}=0 \qquad (3.1)$$

2. *The effect of pressure variation on the density are negligible and the density change is a linear function of temperature change.* Hence,

$$\rho=\rho_0+\left(\frac{\partial \rho}{\partial T}\right)_{\mathrm{P}}.(T-T_0)$$

$$\frac{\rho_0}{\rho}=1+\beta(T-T_0)$$

here ρ_0 & T_0 corresponds to the density and temperature at t=0 sec or some arbitrary value of density and temperature in the range.

$$\beta=-\frac{1}{V}\left(\frac{\partial V}{\partial T}\right)=-\frac{1}{\rho}\left(\frac{\partial \rho}{\partial T}\right) \qquad (3.2)$$

Here thermal expansion coefficient (β) is a material property which quantifies the change in volume with respect to change in temperature.

3. *The density change will only impact the momentum balance via the gravitational term.* Hence, in a system where gravitational force is acting in the negative Y direction, Y-component of Navier- Stokes equation would be

$$\rho\left[\frac{\partial u_y}{\partial t}+u_x\frac{\partial u_y}{\partial x}+u_y\frac{\partial u_y}{\partial y}+u_z\frac{\partial u_y}{\partial z}\right]=-\frac{\partial \mathrm{P}}{\partial y}+\mu\left(\frac{\partial^2 u_y}{\partial x^2}+\frac{\partial^2 u_y}{\partial y^2}+\frac{\partial^2 u_y}{\partial z^2}\right)+\rho g_y$$

$$\rho_0\left[\frac{\partial u_y}{\partial t}+u_x\frac{\partial u_y}{\partial x}+u_y\frac{\partial u_y}{\partial y}+u_z\frac{\partial u_y}{\partial z}\right]=-\frac{\partial \mathrm{P}}{\partial y}+\mu\left(\frac{\partial^2 u_y}{\partial x^2}+\frac{\partial^2 u_y}{\partial y^2}+\frac{\partial^2 u_y}{\partial z^2}\right)+(\rho-\rho_0)g_y \quad (3.3)$$

$$\text{as } (\rho-\rho_0)g_y=\beta(T-T_0)g_y$$

$$\rho_0\left[\frac{\partial u_y}{\partial t}+u_x\frac{\partial u_y}{\partial x}+u_y\frac{\partial u_y}{\partial y}+u_z\frac{\partial u_y}{\partial z}\right]=-\frac{\partial \mathrm{P}}{\partial y}+\mu\left(\frac{\partial^2 u_y}{\partial x^2}+\frac{\partial^2 u_y}{\partial y^2}+\frac{\partial^2 u_y}{\partial z^2}\right)+\beta(T-T_0)g_y \quad (3.4)$$

Figure 3-1 shows the numerical scheme based on the Boussinesq approximation. The nuclear fission heat would create a temperature gradient in the irradiation loop. As per Eq. 3.4, temperature gradient would impact the movement balance in the Y-direction (direction of gravitational force) instigating some flow in Y-direction. This would impact the continuity equation, and to conserve mass some flow will be created in X, Z direction. Which would again impact the energy balance equation and the temperature gradient will change. This iterative change in temperature and flow will continue till the fission heat generated in the irradiation loop equals the heat flux going out of the domain.

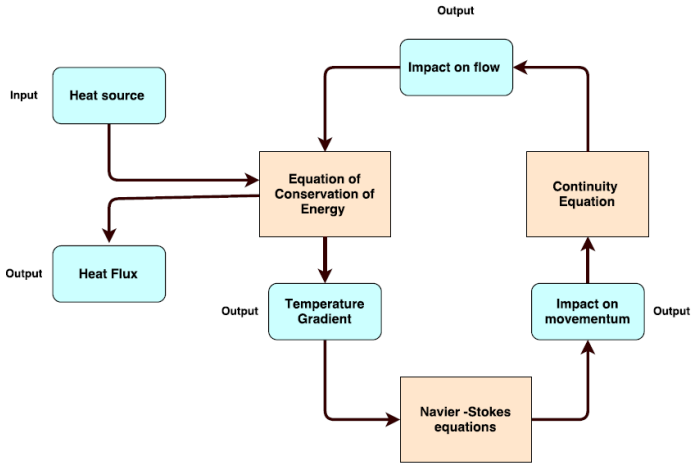

Figure 3-1 Simplified numerical scheme of the Boussinesq approximation

Limiting condition for the Boussinesq approximation

The Boussinesq approximation is only valid when the ratio of density change to the actual density is much less than one. The maximum acceptable temperature gradient within the irradiation loop is 90 ^{0}C, for this the density change to the actual density ratio is 0.0468, which is very less than one.

$$\frac{\rho}{\rho_0}=\beta\Delta T_{\max}=0.0468$$

3.2 Objective

The heat generation inside the irradiation loop makes a bell shaped curve (Figure 2-3) over the X-axis. Any empirical correlation to validate heat transfer modelling inside such non-uniform heat generating fluid is not available. Hence, it was decided to simulate with uniform heat generation such that the Boussinesq approximation for modelling natural convection inside a horizontal cylinder could be validated.

"Validation of CFD simulation for modelling natural convection inside a horizontal cylinder with internal heat generating fluid"

For Uranium concentration of 310 $gU.L^{-1}$, internal heat generation inside the irradiation loop varies from 0 $W.m^{-3}$ to 5.45 MWm^{-3} at the peak. Boussinesq approximation should be valid for the entire range of heat generation.

"Validation of Boussinesq approximation for the operating range of internal heat generation inside the irradiation loop"

Hence, following system was modelled for different heat generation cases whose empirical correlation are available so the modeling method can be validated.

Consider a long horizontal tube (shown in Figure 3-2) of 44 mm diameter. Water is flowing inside the tube with a flowrate of 0.219 gm. s^{-1}. Due to microwaves, whose intensity can be varied, internally heat generates inside the fluid domain. The heat generation is uniformly distributed over the tube. By varying the intensity of microwave, the heat generation rate is varied from case 1 to case 6 (as per Table 3-1). At the outer surface (wall) of cylinder, the external heat transfer coefficient is 10,000 $W.m^{-2}.K^{-1}$ and temperature of surrounding fluid is 300K. Property of the fluid is given in Table 3-2.

Table 3-1 Cases of heat generation to be studied in defined problem

	Heat generation Rate
case 1	16441.73 $W.m^{-3}$
case 2	164417.3 $W.m^{-3}$
case 3	822086.5 $W.m^{-3}$
case 4	1644173 $W.m^{-3}$
case 5	3288346 $W.m^{-3}$
case 6	8220865 $W.m^{-3}$

The problem was solved numerically by using an empirical correlation and then by direct computational modelling in ANSYS Fluent.

Table 3-2 Material properties

Density	990.15 $kg.m^{-3}$
Specific heat	4182 $J.kg^{-1}.K^{-1}$
Thermal conductivity	0.6 $W.m^{-1}.K^{-1}$
Dynamic viscosity	0.000596 $kg.m^{-1}.s^{-1}$
Thermal Expansion Coefficient	0.00042 K^{-1} (14)

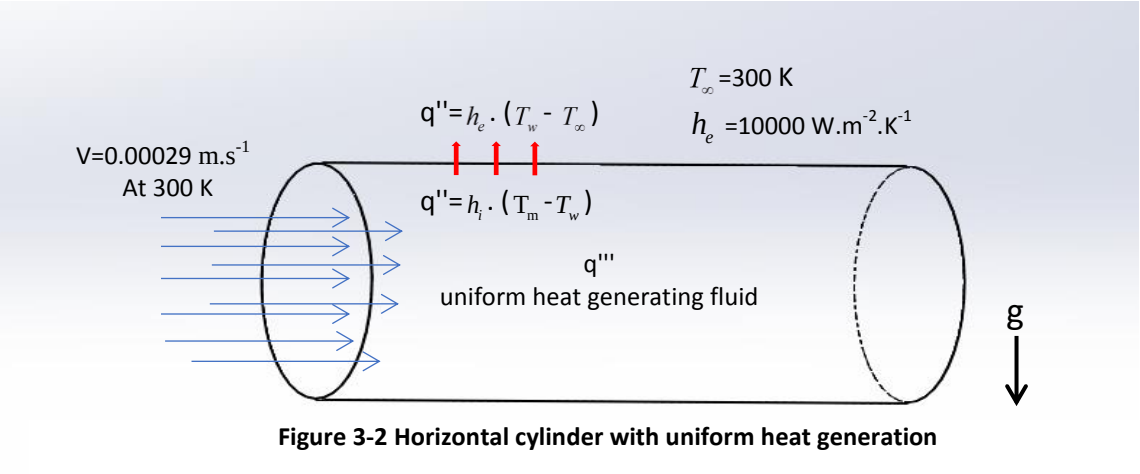

Figure 3-2 Horizontal cylinder with uniform heat generation

3.3 Numerical solution using MATLAB and empirical correlation

Consider a cross section of tube of thickness of dx as shown in Figure 3-3. One dimensional conservation of energy equation over the cross section of cylinder is

$$\pi.r^2.\rho.Cp.\frac{dT_m}{dt}=\pi.r^2.\rho.Cp.\phi_i.\frac{dT_m}{dx}-q".\pi.r+q'''.\pi.r^2$$

At steady state

$$0=\phi_i.\frac{dT_m}{dx}-\frac{q"}{\rho.Cp.r}+\frac{q'''}{\rho.Cp} \qquad (3.5)$$

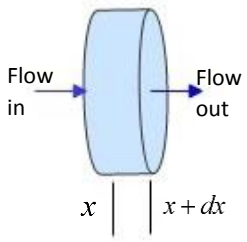

Figure 3-3 Cross Schematic view of tube

Here the q'' in W.m^{-2} is the heat flux from its wall to the surrounding.

$$q"(x)=h_i(x).(T_m(x)-T_w(x))=h_e.(T_w(x)-T_\infty(x)) \qquad (3.6)$$

Inside the pipe the heat transfer takes place initially from the tube core to the boundary wall and then from the boundary wall to the surrounding.

The boundary condition defined for the problem are

$$T_m=300K \text{ at } x=0$$

$$T_\infty=300K \text{ for } 0\le x\le\infty$$

In this problem, there are three unknowns T_m, T_w & h_i and two equations. However, h_i internal heat transfer coefficient is a function of bulk temperature (T_m) and the Wall temperature (T_w) in the tube. By empirical correlations the problem was reduced to just two unknowns and two equations.

The Nusselt number (Nu) for natural convection within the horizontal pipe with isothermal walls is estimated by the Power Law correlation given below (12).

For laminar flow (Ra <10^9)

$$Nu = 0.53(Ra)^{0.25} \qquad (3.7)$$

For turbulent flow (Ra > 10^9)

$$Nu = 0.13(Ra)^{0.33} \qquad (3.8)$$

Nusselt number (Nu) is a non-dimensional number which compares the convective heat transfer to the conductive heat transfer. High Nusselt number implies that the heat transfer mechanism would primarily happen by convection.

$$h_i = Nu.\frac{D}{k} \quad \& \quad Ra = \frac{g\beta(T_m - T_w)D^3}{\nu\alpha}$$

By assuming applicability of either equation 3.7 or 3.8. One dimensional temperature profile inside the pipe was solved using Newton's explicit method of solving differential equations. The MATLAB program of this problem is available in Appendix A.

Results & Discussion

1) As the fluid travels inside the tube, due to internal heat generation the bulk temperature inside the tube increases. However, the region near the wall is subject to a very high external heat transfer coefficient and low external temperature, this results in an internal temperature gradient inside the tube leading to natural convection. The bulk temperature and the wall temperature would increase with the length of the tube. At certain point, the bulk temperature and the wall temperature balances the total heat produced inside the pipe with the total heat leaving from the tube. This forms an equilibrium of temperature gradient, heat production and heat transfer.

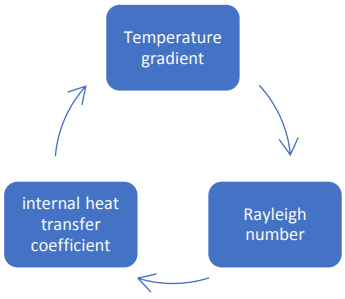

Figure 3-4 Interdependency

2) The applicability of either Eq. 3.7 or Eq. 3.8 depends on the Rayleigh number at that position inside the pipe. However, the Rayleigh number is determined by the temperature gradient in the pipe and the Rayleigh number determines the internal heat transfer coefficient which again determines the temperature gradient. Hence, to solve this interdependency problem a trial and error approach was used. For all the cases, initially it was assumed that the flow inside the pipe is laminar and the equation 3.6 was applied to calculate Nusselt number. Like temperature change the Nusselt number develops over the length of the pipe and stabilizes. For all the cases calculated the Rayleigh number observed was less than 10^9, which confirms the initial assumption of **laminar flow** in the tube (12).

3) Figure 3-5 shows how the bulk and wall temperature develops inside the pipe for all the cases. As anticipated, the temperature difference between the bulk temperature and the wall temperature increases with the internal heat generation rate.

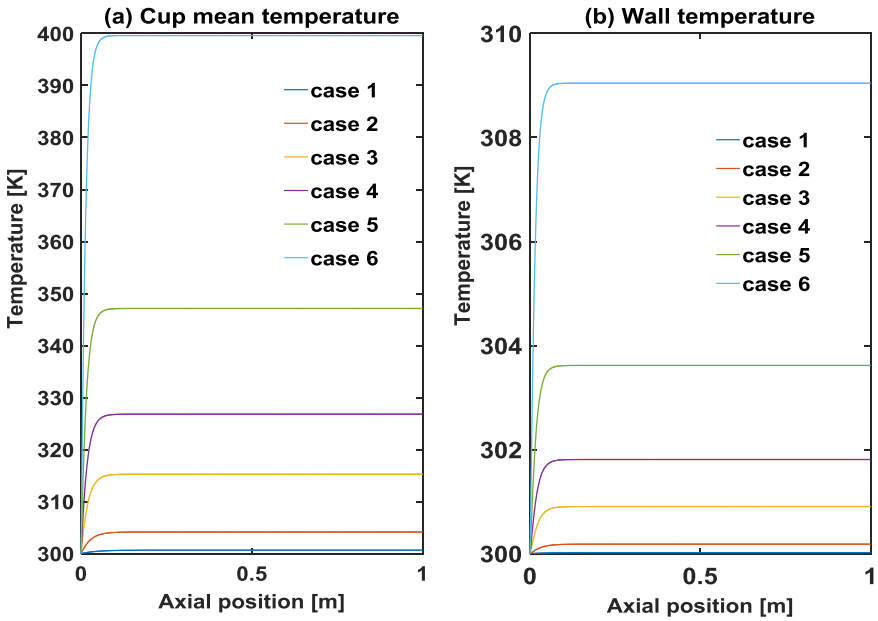

Figure 3-5 (a) Bulk Temperature and (b) Wall Temperature development profile from empirical correlation

4) As the temperature inside the tube reaches a steady state the Nusselt number and the Rayleigh number also attends a steady value. Table 3-3 illustrate these values for all the cases studied.

Table 3-3 Steady state Nusselt number and Rayleigh number in Tube

	Nusselt number	Rayleigh number
Case 1	21.13	2.53×10^6
Case 2	33.49	1.59×10^7
Case 3	46.20	5.78×10^7
Case 4	53.07	1.01×10^8
Case 5	60.96	1.75×10^8
Case 6	73.23	3.65×10^8

3.4 Numerical solution by Computational fluid dynamics

ANSYS Fluent software's academic version 18.1 was selected for modelling this problem. ANSYS Fluent uses finite volume method to analyze and solve various transport phenomena's.

3.4.1 Physical model

Similar steps as explained in Figure 2-7 were followed for modelling this problem. A horizontal tube of 44mm dimeter and 1m length was created in SolidWorks. At the center of the tube across the vertical plane parallel to y -axis symmetry was assumed and only half cylinder was modelled to reduce

the simulation time. The cylinder is placed such that the axis of the cylinder is the x-axis and gravity is acting in the negative y-direction. The physical model can be seen in Figure 3-6.

3.4.2 Boundary conditions

To mimic an infinitely long pipe with internal heat generation, it was assumed that the inlet and the outlet faces of the pipe have periodic flow. i.e. the flow stream leaving at the outlet of the pipe re-enters the pipe from the inlet. At the wall of the pipe no slip and constant external heat transfer coefficient of 10000 $W.m^{-2}.K^{-1}$ with 300 K as the surrounding temperature boundary condition is applied. Also, symmetry boundary condition at the symmetry plane is given. The internal heat generation is defined as an energy source term in the fluid domain.

Table 3-4 **tabulates all the boundary condition defined for the problem**

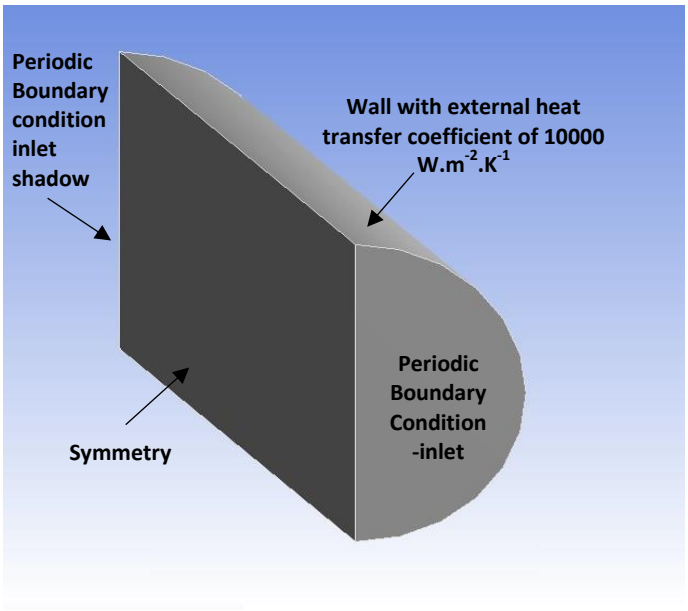

Figure 3-6 Geometry and the Boundary conditions in the model

Table 3-4 boundary conditions defined in Fluent

Boundary conditions	Type	Specification
Inlet	Translation periodic	ϕ_i . ρ = 0.000219 kg. s^{-1}
Outlet	Translation periodic	
Wall	Velocity	$\bar{u} = 0$ (No slip)
	Thermal	h_e = 10000 $Wm^{-1}K^{-1}$, T_∞ =300K
Symmetry plane	Symmetry	
Liquid Fluid domain	Energy source term	* q''' $W.m^{-3}$

*Heat source was defined as per the case specified in Table 3-1

3.4.3 Simulation setup & the Discretization scheme

From earlier empirical calculation it was very clear that for all the six cases the flow inside the tube would be laminar in nature. Hence, laminar model was selected for numerical modelling. The energy equation was turned on and the gravity was set to be acting in negative y -direction with 9.81 $m.s^{-2}$ acceleration. To enable the Boussinesq approximation, in the material property of the fluid density was selected as "Boussinesq". Density, Thermal expansion factor, viscosity, specific heat, and thermal conductivity of all fluid parameters were specified.

Table 3-5 illustrates the numerical scheme adopted for modelling. This numerical scheme is adopted as per the suggestion given in ANSYS theory guide (15). Simple (Semi-Implicit Method for Pressure-Linked Equations) algorithm was selected. Pressure is discretized using the body force weighted scheme to accommodate the buoyancy force's impact over the cell face. Movement and energy equations were discretized by first order upwind scheme (15). Also, the convergence criteria of 10^{-6} was applied.

Table 3-5 Numerical scheme considered for modelling the solution

solution method	
scheme	simple
spatial Discretization	least square cell based
pressure	body force weighted
momentum	first order upwind
energy	first order upwind

3.4.4 Grid discretization and mesh independence study

For a cylindrical flow domain, it was possible to have all the elements in a structured mesh to be hexagonal, hence, the grid was discretized in all hexagonal elements. Also, to capture the activity near wall region thick inflation layer was added in the mesh. Cross sectional view of grid discretization could be seen in Figure 3-7(a).

Preliminary mesh independence study was carried out to check the dependence of solution on meshing. Four different meshes were developed with coarse to fine as shown in Table 3-6. As in simulation inlet and outlet boundaries are periodic, the simulation does not show any variation in x direction hence, extra elements were added on to the y - z plane and in all four cases the meshing was kept similar in x -direction. The size of hexagonal element on the y - z plane was reduced from mesh A to smallest elements in mesh D.

Table 3-6 Mesh independence cases

cases	mesh A	mesh B	mesh C	mesh D
elements	219300	290600	484000	694900

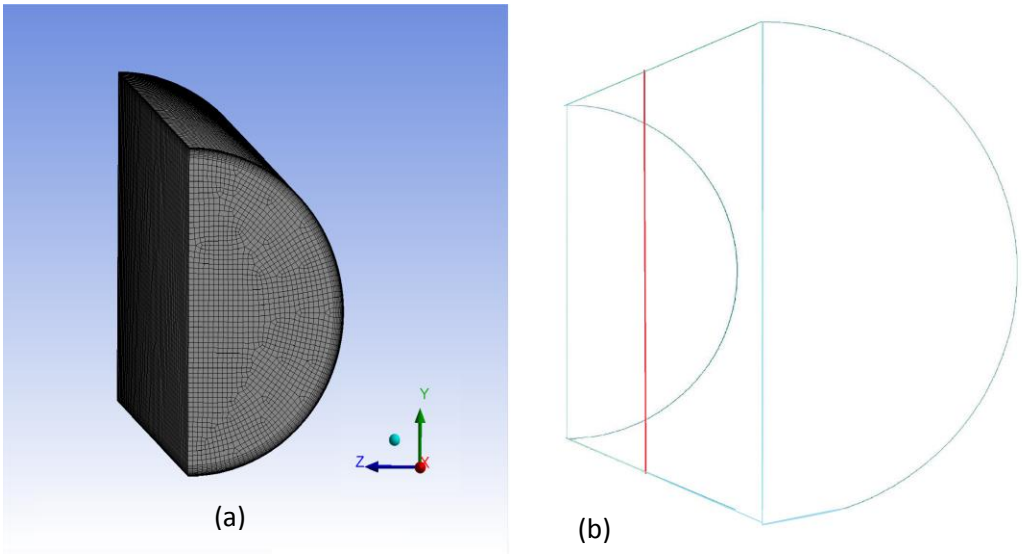

Figure 3-7 (a) Selected mesh for modelling on the left and (b) Position of line (red) used for mesh independence study

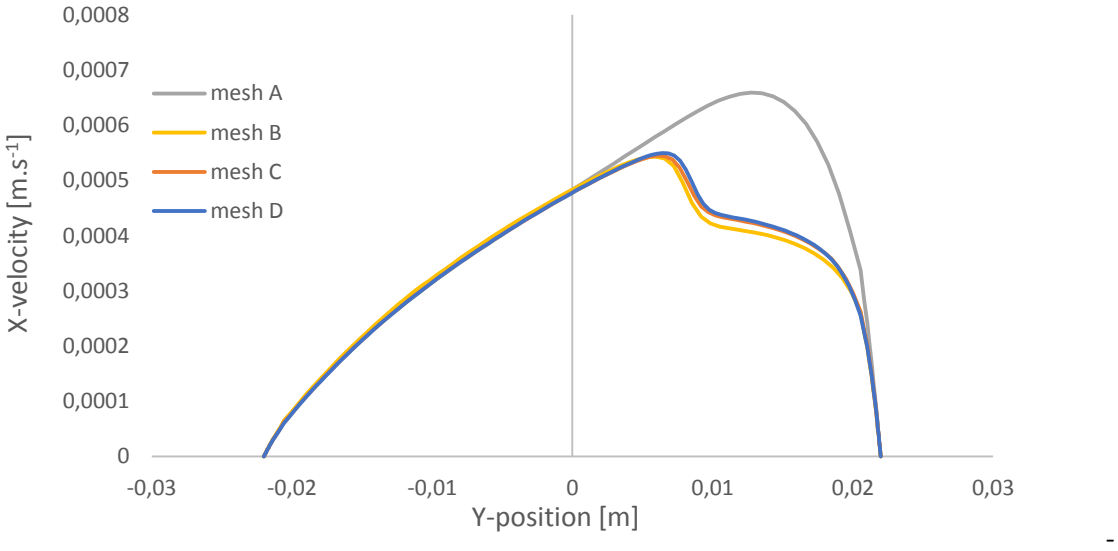

Figure 3-8 x-velocity profile on vertical line for all four mesh

To study the mesh independency of the result x-velocity profile over a vertical line (in Figure 3-7(b)) was plotted for all four meshes. The result of mesh C and mesh D overlaps over one another which means that the simulation has reached independence from the meshing from mesh C. Hence, for all cases mesh C was selected to carry out mesh independence study.

3.4.5 Simulation Result and Discussion

Figure 3-9 shows the steady state temperature, velocity, vector and streamline profile over the cross section of the tube for Case 4. The velocity and the temperature profile inside the horizontal

cylinder matched with the study performed by Kohshi Mitachi and Katsuyuki Aoki (16). Similar temperature and velocity profile were observed for all the cases.

The Internal heat generation inside the tube is uniform. Hence, the temperature of the fluid will start to rise uniformly. However, the surrounding temperature to the pipe remains at lower temperature; consequently, this will result in heat transfer from near wall fluid to the surrounding. Setting the near wall region at low temperature and the tube core at high temperature, the temperature difference between the tube core and near wall region would create density difference between these two regions, causing the core fluid to rise vertically upwards. To conserve mass at the core, rising flow will be balanced by the downward moving flow near wall region. Creating two vortexes near the wall as shown in Figure 3-9 (D). The flow moving down subjects to a cooling effect by the external heat transfer and the rising fluid from the center is gaining heat by internal heating. This creates a stratification of temperature which could be scene in the temperature profile from Figure 3-9 (A).

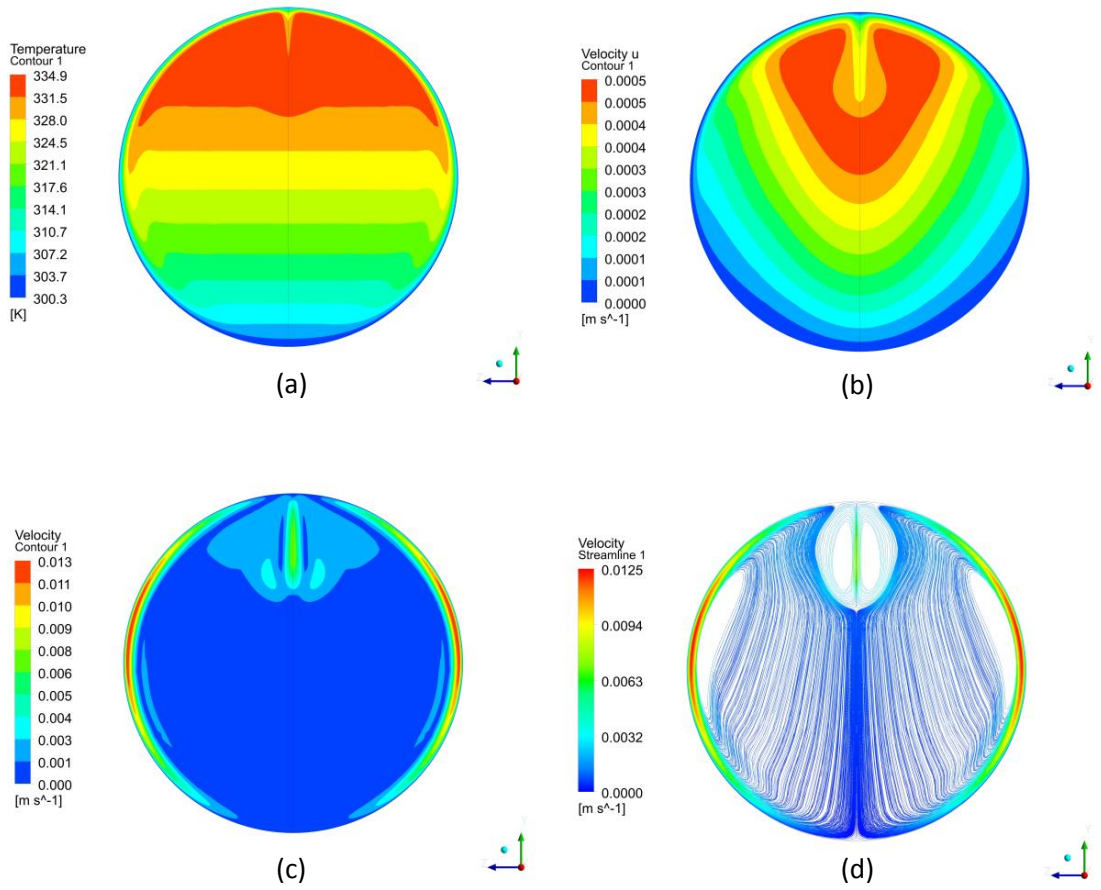

Figure 3-9 Steady state Result of case 4 (a) Temperature profile (b) Axial Velocity profile (c) Velocity magnitude profile (d) Stream line profile over the cross section

Table 3-7 Heat transfer calculation for tube (13)

Equation (3.9)	$T_m = \frac{\int_{A_{cs}} u_x T dA}{\int_{A_{cs}} u_x dA} = \frac{\sum_{A_{cs}} u_x T}{\sum_{A_{cs}} u_x}$	As the pipe has a uniform axial velocity and the velocity and temperature profile over the length of the tube remains constant. T_m was calculated as the cup mixing (adiabatic) temperature.
Equation (3.10)	$T_w = \frac{\int_{A_w} T dA_w}{\int_{A_w} dA_w} = \frac{\sum_{wall} T}{A_w}$	Wall temperature over the cross section of the pipe varies with the angle it makes with the origin. However, to generalize area average temperature of the wall was considered as the wall temperature.
Equation (3.11)	$Nu = \frac{q".D}{K.(T_m - T_w)}$	The Average Nusselt number over the cross section of tube.

3.5 Analysis of Empirical and CFD Result

Figure 3-10 shows that steady state bulk temperature (a) and wall temperature (b) calculated in ANSYS fluent and by the empirical correlation in MATLAB. Both cup mean temperature and the wall temperature estimated for all cases are in good correlation. Even Nusselt number and Rayleigh number for a steady state solution shows similar correlation. The maximum error in the Nusselt number is 2.8% for case 6 which is acceptable. Hence, for the range of heat generation, a good agreement between the empirical results and the simulated result confirms that the modelling technique with Boussinesq approximation is valid.

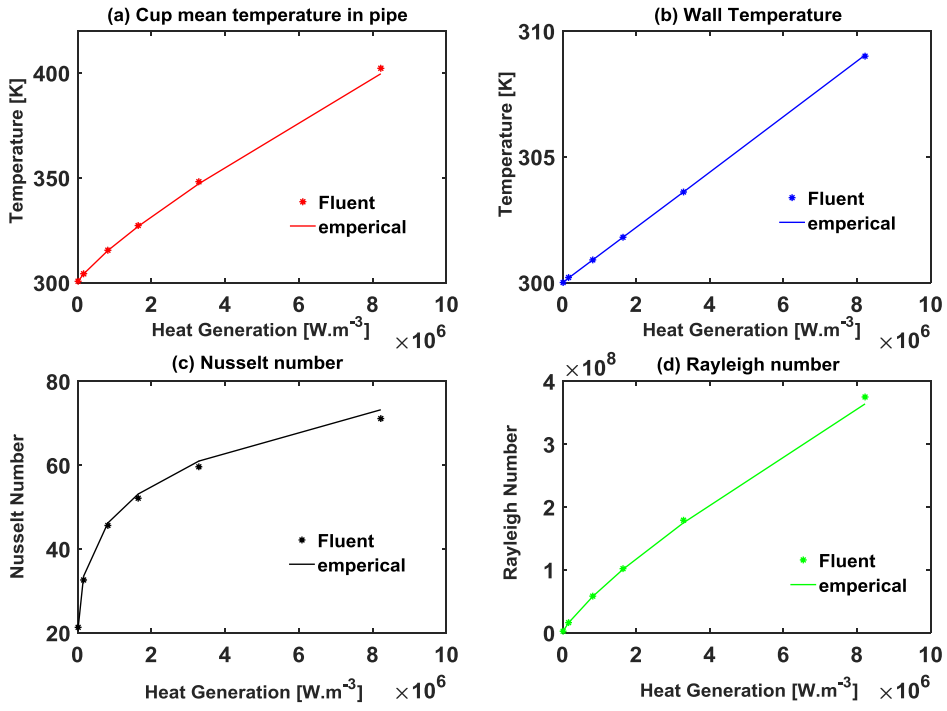

Figure 3-10 Comparison of empirical result and the CFD result a) Steady state cup mean temperature b) avg. wall temperature c) Nusselt number d) Rayleigh number

3.5.1 Maximum Temperature in the domain

Figure 3-11 shows the Maximum Temperature in the Tube for all six cases. As expected the maximum temperature increases with the Internal heat generation in the fluid. Moreover above 4.2 MW.m^{-3} maximum temperature in the domain is above 100 ^{0}C (critical Temperature), which would mean for irradiation loop there exists an internal heat generation limit above which the operating temperature inside the loop will increase above its boiling point.

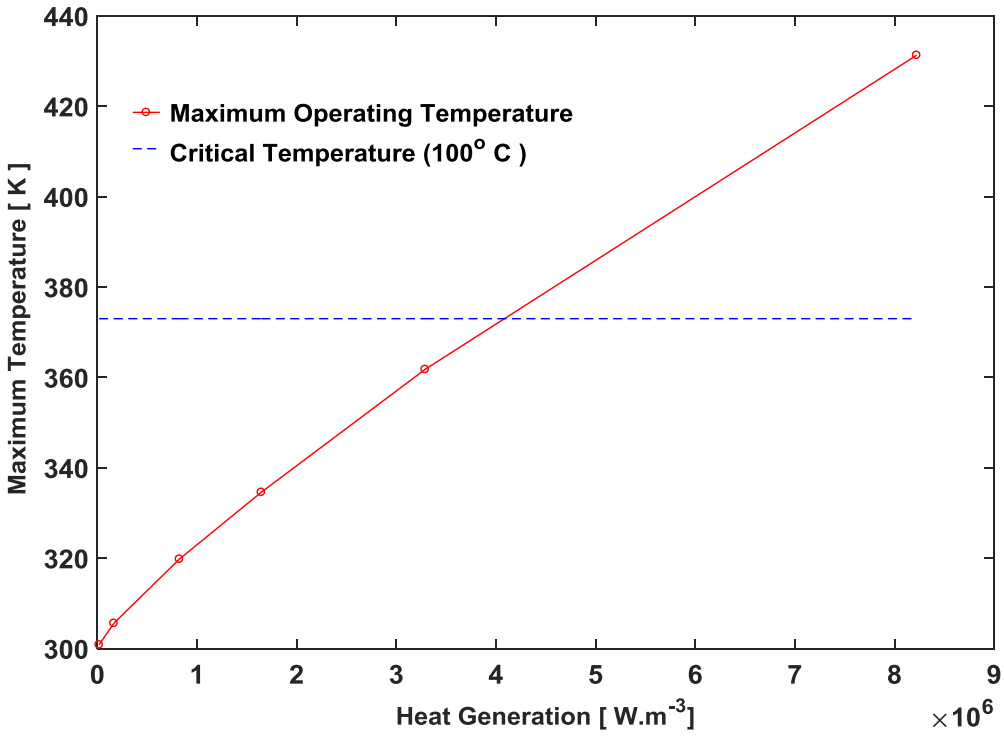

Figure 3-11 Maximum temperature in the tube

3.6 Conclusion

In this study, the heat transfer mechanism inside a horizontal cylinder with an internally heat generating fluid was modelled using the Boussinesq approximation. This model was verified and validated by an empirical correlation found in the literature. From the result, it can be concluded that for given operating range of heat production the Boussinesq approximation & defined simulation setup can be used to model complete irradiation loop setup.

Chapter 4

Internal Heat Transfer Limitation

In chapter 3, the modelling technique of the Boussinesq approximation to simulate natural convection inside the irradiation loop was validated. During the simulations, the wall temperature was kept close to the surrounding temperature by artificially applying a high external heat transfer coefficient. However, as it can be seen in Figure 3-11 when the internal heat generation rate is above 4.2 $MW.m^{-3}$, the maximum temperature in the tube exceeded the boiling point of water. Inside the irradiation loop the segment in front of HOR core has higher heat generation rate then 4.2 $MW.m^{-3}$ (Figure 2-3).

In this chapter, the irradiation loop with the bell-shaped heat generation profile was modelled to ensure the internal heat transfer mechanism is not limiting the heat transfer by creating high temperature gradient in the irradiation loop.

4.1 Theory

At steady state, the total heat produced inside the fluid domain will be given out to the surrounding.

At steady state, $$H_v.V = A.h_i.(T_h - T_w) = A.h_e.(T_w - T_c) \quad (4.1)$$

for a heat generating fluid, the temperature gradient inside the fluid depends on internal and external heat transfer mechanism. There are three possible scenarios in which the temperature of the heat generating fluid can cross the critical temperature (boiling point). As shown in Table 4-1.

1) Case - I: - Limiting external heat transfer coefficient
2) Case -2: - Limiting internal heat transfer coefficient
3) Case -3: - Limiting both internal and external heat transfer coefficient's

Table 4-1 Limiting cases of heat transfer from the irradiation loop

Case 1 Limiting external heat transfer coefficient	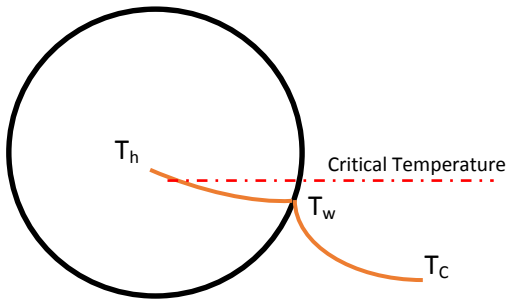	The external heat transfer coefficient limits rate of heat transfer, which would cause an elevated temperature gradient outside the irradiation loop. This would ultimately elevate the temperature inside the irradiation loop.

Case 2 Limiting internal heat transfer coefficient	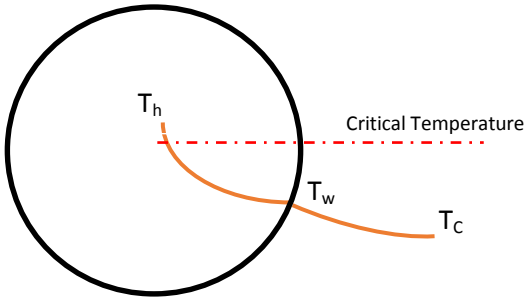	The internal heat transfer coefficient is low which would cause elevated temperature gradient inside the irradiation loop. In such scenario, the operating temperature of the irradiation loop can cross the critical temperature.
Case 3 Limiting internal & external heat transfer coefficient	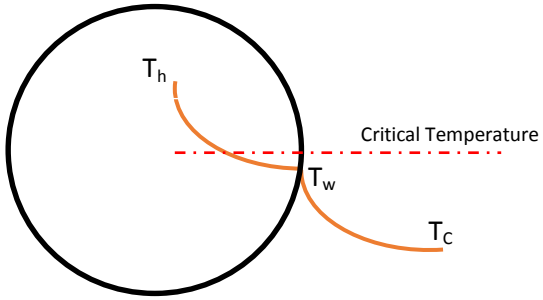	Both internal and external heat transfer coefficient are low which would cause the temperature inside the domain to increase above critical temperature.

In the first case, by varying the cooling mechanism or coolant temperature, the external heat transfer limitation can be eliminated. However, in case 2 the internal heat transfer mechanism limits the heat transfer. In the irradiation loop the internal heat transfer mechanism is governed by the natural convective flow. As natural convection cannot be controlled, It was important to identify such scenario.

4.2 Objective

In a system with limiting internal heat transfer coefficient, the internal mechanism would demand a high temperature gradient to remove heat produced. Hence, even with an efficient cooling mechanism the temperature inside the irradiation loop would remain higher than critical temperature hence before designing a cooling system following objective was set.

"To ensure the internal heat transfer mechanism inside the irradiation loop is not limiting the heat transfer"

Secondary objective

The heat generation inside the irradiation loop depends on the concentration of uranium nuclei, the neutron flux from the core and the neutron fission cross section of uranium nuclei. In the current setup, the neutron flux from the HOR core is constant. So, the only degree of freedom which would vary heat generation is the concentration of uranium inside the irradiation loop.

"To calculate the limiting internal heat transfer coefficient inside the irradiation loop for varying concentrations of uranium."

4.3 CFD Modelling

The Uranyl nitrates aqueous solution inside the irradiation loop will be modelled with the bell shaped internal heat generations profile corresponding to 310 $gU.L^{-1}$ concentration for this system. The

external heat transfer coefficient will be incrementally varied and the impact of external heat transfer over the internal temperature field will be analyzed to check the internal heat transfer limitation.

4.3.1 Physical model

Figure 4-1 shows the geometry of the irradiation loop. It is a cylindrical tube in a U-shaped structure with an inner diameter of 44mm. The loop was positioned horizontally such that the gravity is acting in the negative Y-direction and both the axis of the cylinder are parallel to the x-axis. Around 80mm of the tube length was extended from the DLDR left flange. The dimensions of the model have been defined in Figure 4-1.

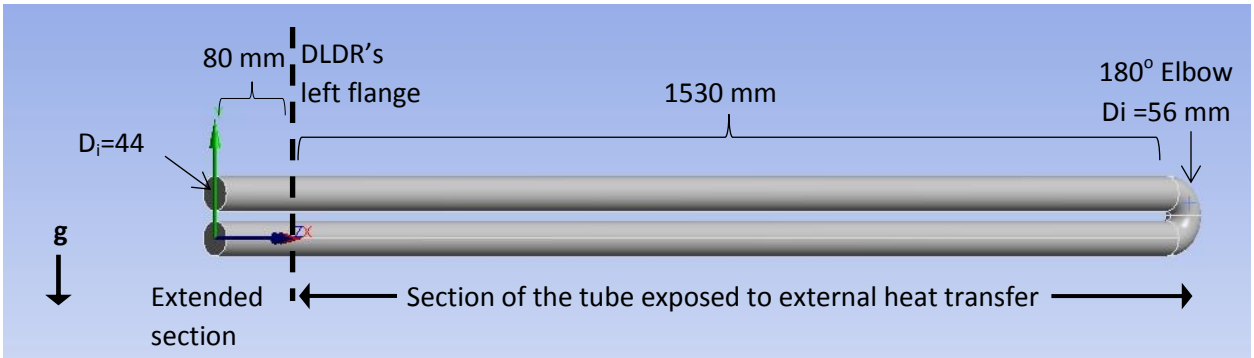

Figure 4-1 Physical model of the irradiation loop

4.3.2 Simulation setup

The flowchart explained in figure 2.2 was followed to export the geometry from SolidWorks to run simulations on Fluent. For the envisaged operating range, the natural convective flow inside the irradiation loop is expected to be laminar. Hence, laminar model was selected. The numerical scheme and the simulation setup validated in the chapter 3 was followed. All simulations were carried in a transient model till it reached a steady state result. Convergence criteria of 10^{-5} was selected for velocity and continuity equation and 10^{-6} for the energy equation.

4.3.3 Material properties of uranium nitrate solution

In literature, most of the properties such as density and viscosity of uranyl nitrate solutions are available. The thermal expansion coefficient and the thermal conductivity data were unavailable. Hence, water's thermal expansion coefficient and thermal conductivity data was used for modelling. The variation in specific heat and density of the solution with respect to the concentration of uranyl nitrate can be calculated using appendix B and C.

Table 4-2 Uranyl nitrate solution material properties

Uranyl nitrates' aqueous solution (310 $gU.L^{-1}$)		Water property used
Density (5)	1330.6 $kg.m^{-3}$	No
Specific heat (5)	2905.5 $J.kg^{-1}.K^{-1}$	No
Thermal conductivity	0.65 $W.m^{-1}K^{-1}$	Yes
Viscosity (5)	0.00122 $kgm^{-1}.s^{-1}$	No
Thermal expansion coefficient	0.00052 K^{-1}	Yes

4.3.4 Boundary condition

Following boundary conditions were defined for modelling irradiation loop.

Table 4-3 Boundary conditions defined in Fluent

Name	Type	Specification
Flow Inlet	Velocity inlet	u_x =0.0002916 m.s^{-1}
	Thermal	T =300K
Flow outlet	Outflow	$\frac{\partial u_x}{\partial x}=0, \frac{\partial T}{\partial x}=0$
Wall	Velocity	$\bar{u}=0$ (No slip)
	Thermal convection	h_e *, T_∞ =300K

*The external heat transfer coefficient was varied as per the simulation cases

4.3.5 Heat generation

From MCNP's neutron flux study, August Winkelman confirmed that for a Uranium concentration of 310 gU.L^{-1}, 7.87 kW of heat will be produced by nuclear fission reaction. However, the heat generation inside the irradiation loop creates a bell-shaped curve (Figure 2-3) in which the heat production varies from 0 W.m^{-3} to 5.4 MW.m^{-3} at the peak. This heat due to fission reaction inside the loop was modelled using a user defined function (UDF). UDF was created to duplicate the heat generation curve (Figure 2-3) inside the uranyl nitrate solution. Appendix D can be referred to understand how heat source was defined in Fluent.

4.4 Grid discretization and mesh independence study

As the uranyl nitrate solution is flowing in the cylindrical loop, it was possible to discretize the entire domain into a structured mesh of hexagonal elements. Hence, the entire mesh was discretized in hexagonal elements. A thick inflation layer of 15 cells was formed near the mesh wall such that the activity in the near wall region would be captured effectively. Figure 4.2 Shows the grid discretization of the selected mesh.

The preliminary mesh independence study was carried out to check the dependence of solution on meshing. Four different meshes were developed with coarse to fine, the number of elements were increased consequently in both axial direction and over the face of the mesh. Number of elements in each mesh is shown in Table 4-4.

Table 4-4 Mesh independence cases

mesh 1	mesh 2	mesh 3	mesh 4
464,200	583,440	1,531,200	1,920,009

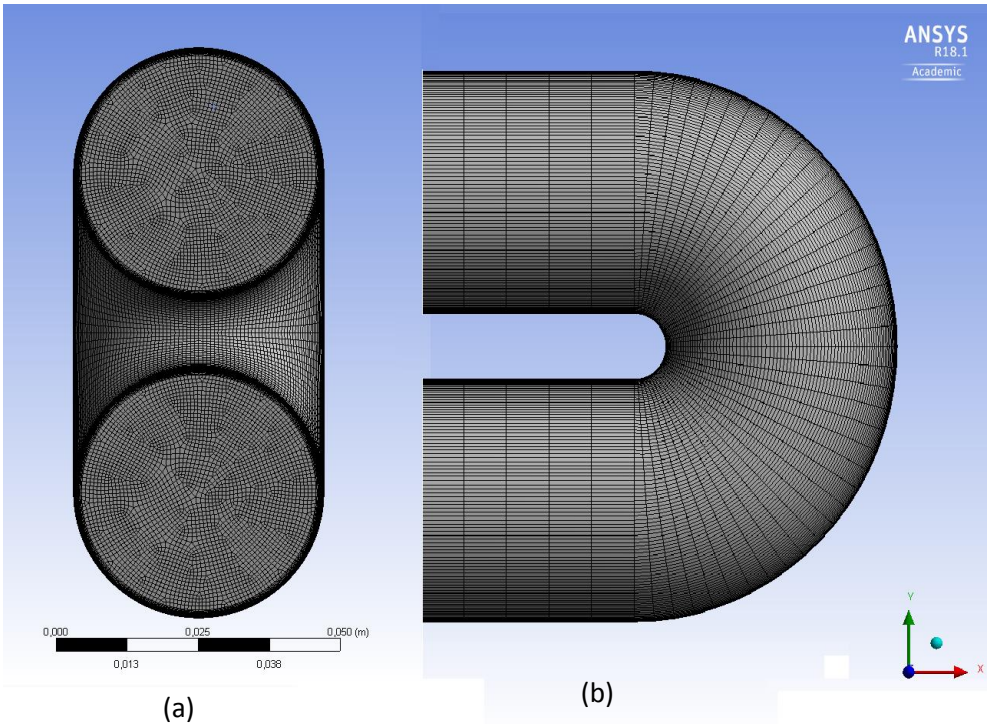

Figure 4-2 Grid discretization for selected mesh (a) Front view from the Left flange of DLDR (b) Side view of 180° bend

A mesh independency study was carried out by plotting the velocity and temperature profile over a vertical line as shown in Figure 4-3 connecting point 1 (0.78, -0.022,0) [m] and point 2 (0.78, 0.022,0) [m] were plotted. Figure 4-4 and Figure 4-5 show that the velocity and temperature plots for all four cases. For mesh 3 & 4, the velocity and temperature profile overlaps. This indicates that after increasing the number of elements from mesh 3 to mesh 4 the simulation result would remain the same. Hence, mesh 3 with 1,531,200 elements was selected for further analysis.

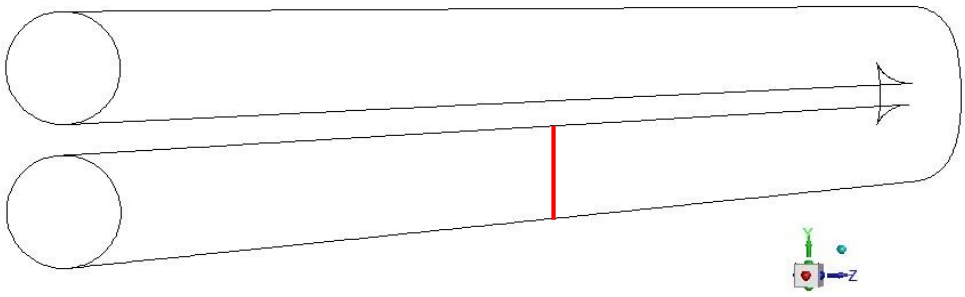

Figure 4-3 Mesh independence study was carried out on red line

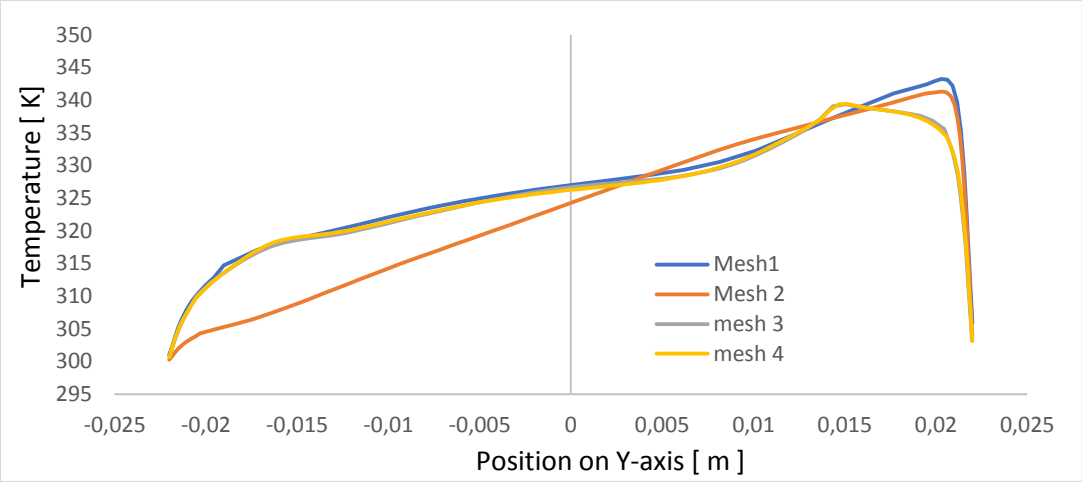

Figure 4-4 Temperature profile over Vertical line

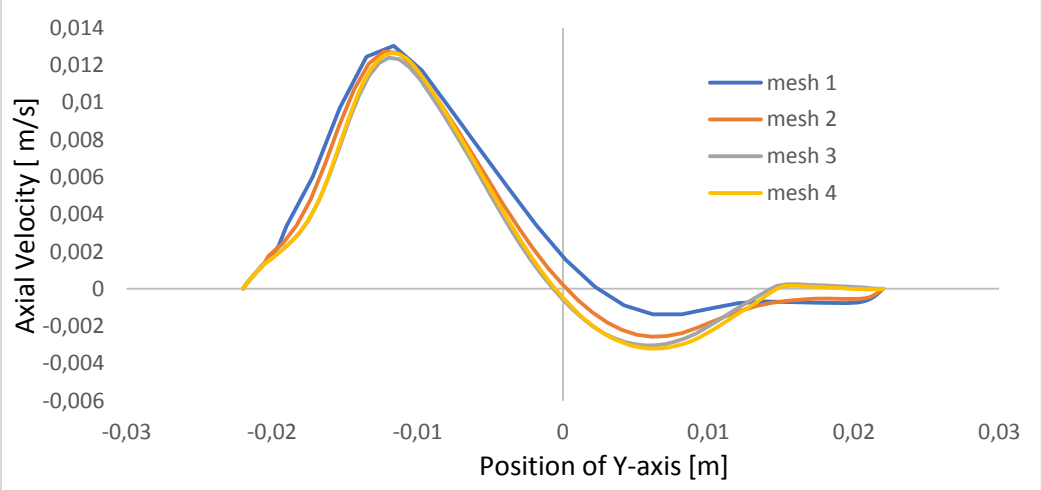

Figure 4-5 Temperature profile over the vertical line

4.5 Result and Discussion

All the cases were simulated with varying external heat transfer coefficient. Similar temperature and flow profile were observed for all external heat transfer coefficients. Figure 4-6 shows a typical velocity, streamline and temperature profile which were observed on plane parallel to x-axis (at z=0) for the case with external heat transfer coefficient of 10,000 $W.m^{-2}.K^{-1}$.

Figure 4-6 (a) shows a typical temperature profile inside the irradiation loop. As expected the temperature profile is analogous to the heat generation profile. i.e. the temperature in irradiation loop is highest in front of the reactor core and reduces near the right and left flanges. However, in Figure 4-6(b) the velocity contour in axial direction showed four different circulation zones corresponding to two legs of the heat generating curve with either increasing or decreasing heat generation rate.

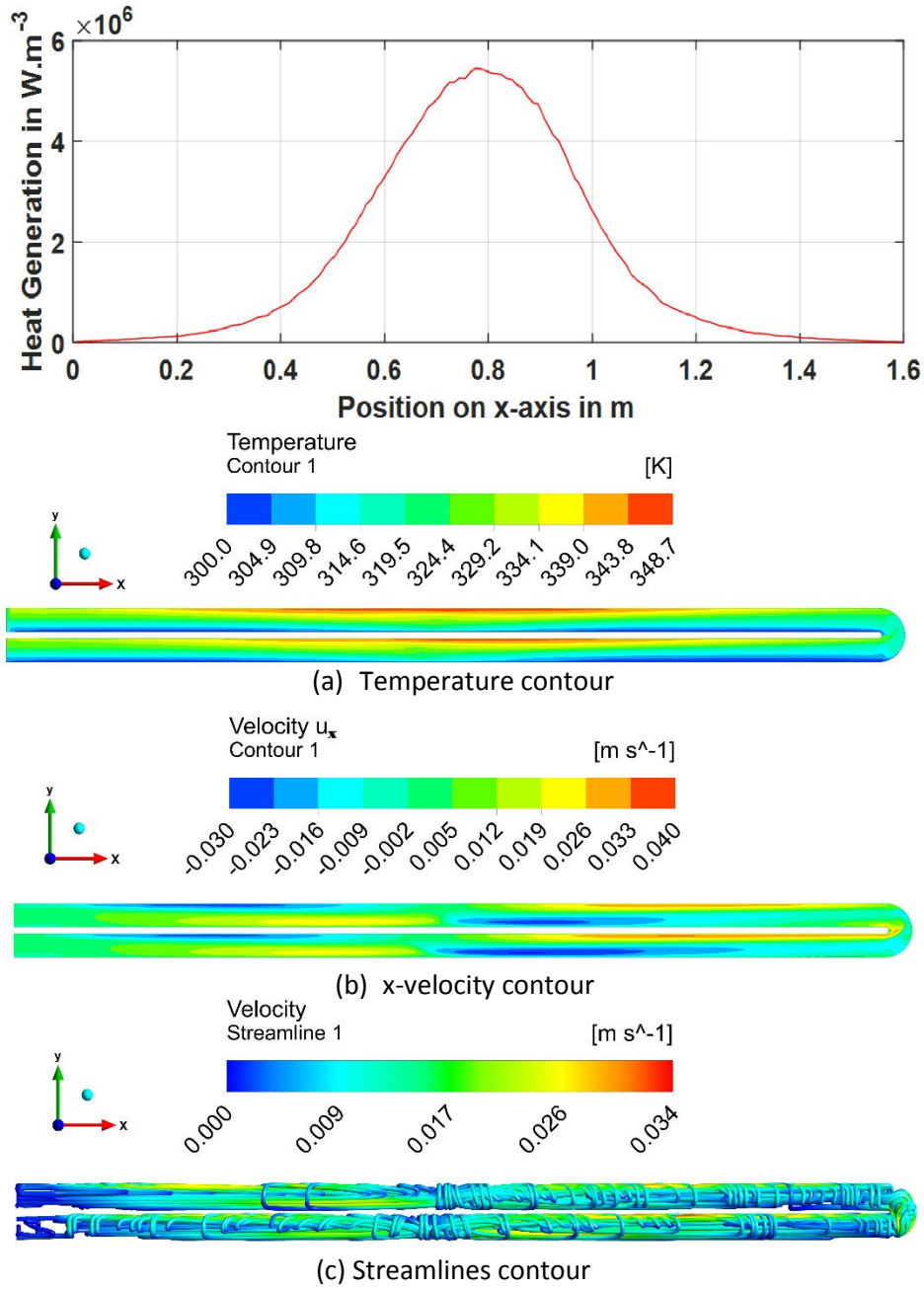

Figure 4-6 For case with external heat transfer coefficient of 10000 W.m^{-2}. K (a) Temperature contour (b) X-velocity Contour (c) streamline contour

In Figure 4-8 the temperature profile is plotted over three different positions on the x-axis. Plane-I and plane-II are normal to the x axis and are at x =0.2 m and x =0.83 m. Over both planes the temperature profiles shows similarities however, due to different energy generation rate the fluid on plane II would be hotter than the fluid on plane I. In chapter 3, temperature gradient was seen only in the y - z plane. There wasn't any temperature gradient in axial x-direction. However, over the irradiation loop the bell-shaped heat generation creates a bell-shaped temperature distribution. Hence,

a temperature gradient is seen in the x-direction. This creates a force imbalance in axial direction creating different flow pattern then the previous study.

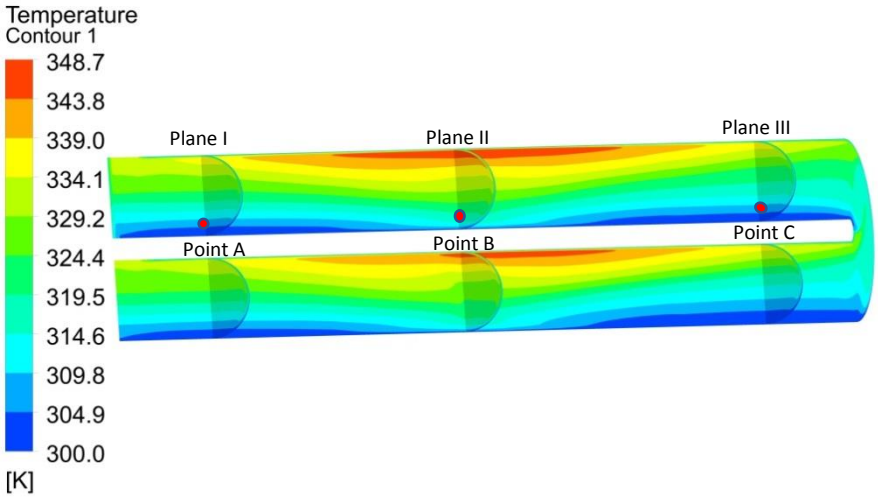

Figure 4-7 Temperature profile over plane I, II & III

Consider three points A, B & C from Figure 4-7 over plane I, plane II & Plane III. The volumetric heat generation rate over plane I & plane III is less than the volumetric heat generation at plane II. When the surrounding temperature and the external heat transfer coefficient acting over the surface of loop would be the same everywhere, the vertical temperature gradient at point B would be more than the temperature gradient at point A & C. Hence, the buoyant force acting at point B would be more than point A & C. Due to continuity two circulation zones are created, one on the left side and one on the right side of point B. This analogy can explain the four circulating zones observed on the streamline and velocity profile in Figure 4-6 (b) & (c).

4.5.1 Heat transfer study

As the temperature and velocity profile inside the irradiation loop varies, the internal heat transfer coefficient acting locally on wall would vary. A simplistic approach was taken to calculate the average internal heat transfer coefficient. The internal heat transfer coefficient inside the irradiation loop is defined as following

$$h_i = \frac{q''_{wh}}{A_{wh}.(T_h - T_{wh})} \qquad (4.2)$$

Where h_i is the internal heat transfer coefficient, q''_{wh} is total heat flux from the wall, A_{wh} is inner surface area of tube wall, T_h is volume average temperature inside the irradiation loop and T_{wh} is area average temperature of irradiation loop. Following equation were used to calculate the values of T_h and T_{wh} values for various cases of simulation.

$$T_h = \frac{\iiint_V T.dV}{\iiint_V V.dV} = \frac{\sum_V T}{\sum_V V} \tag{4.3}$$

$$T_{wh} = \frac{\int_{A_{wh}} T dA_{wh}}{\int_{A_{wh}} dA_w} = \frac{\sum_{wall} T}{A_{wh}} \tag{4.4}$$

Table 4-5 Impact of varying external heat transfer coefficient

h_e W.m^{-2}.K^{-1}	$T_{\max}$ in K	T_h in K	T_w in K	h_i W.m^{-2}.K^{-1}
500	391.8	355.5	335.9	892.0
1000	370.9	337.8	318.5	916.9
2000	359.06	328.8	309.7	928.0
5000	351.5	323.4	304.4	932.7
10000	348.1	321.6	302.6	933.2
20000	347.6	320.8	301.7	933.1
50000	346.7	320.2	301.2	933.3

Figure 4-8 illustrates internal heat transfer coefficient & the maximum operating temperature inside the tube for varying external heat transfer coefficients. Initially the internal heat transfer coefficient seems to be increasing with the external heat transfer coefficient. However, roughly from 1000 W.m^{-2}.K^{-1} onwards the internal heat transfer coefficient increases marginally and settles around 933 W.m^{-2}.K^{-1}. This behavior can be explained by specific Biot number Bi_S . (Refer appendix E).

Specific Biot Number

For an internal heat generating system with natural convection, the specific Biot number is the ratio of external heat transfer coefficient to the limiting internal heat transfer coefficient.

$$Bi_S = \frac{h_e}{h_{i\_\text{limiting}}}$$

At low specific Biot number (<1) the h_i seems to be increasing more rapidly with h_e. However, as the specific Biot number is increasing ($Bi_S > 1$), the rate of increase of h_i with respect to h_e seems to reduce and at certain point h_i reaches a maximum value and then remains constant. This h_i is the limiting heat transfer coefficient for the irradiation loop. As h_{i_limiting} is the maximum internal heat transfer coefficient, at h_{i_limiting} the temperature gradient in the loop is optimum (minimum).

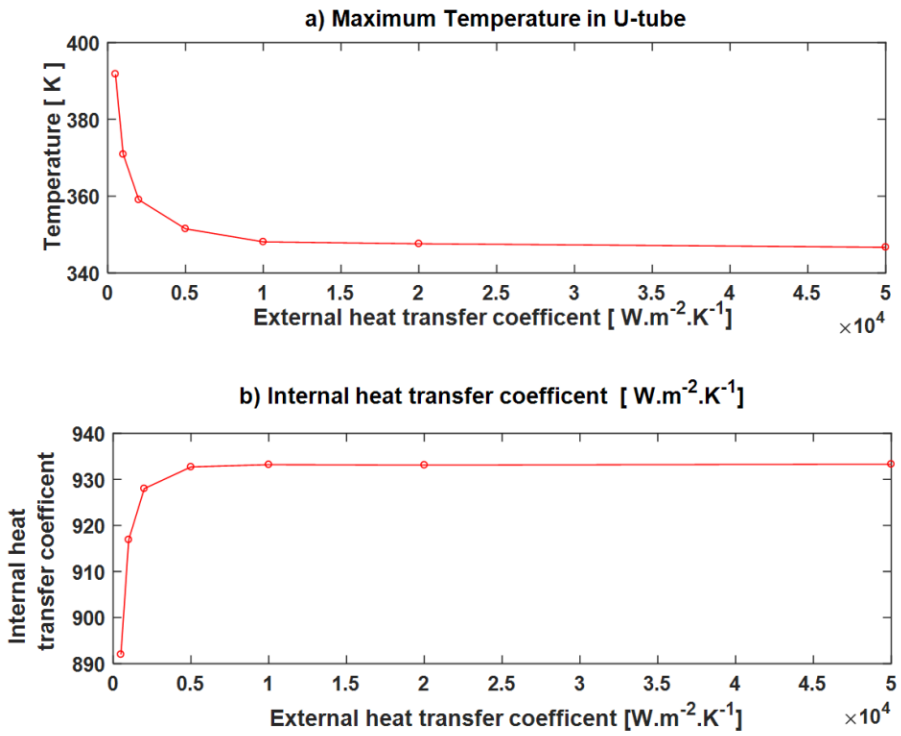

Figure 4-8 Impact of varying external heat transfer coefficient on a) Maximum operating temperature (b) Internal Heat Transfer Coefficient

The maximum operating temperature in the loop showed a similar profile as the h_i. Up to the point when the specific Biot number was less than one the internal heat transfer coefficient was low hence to dissipate generated heat the temperature gradient was higher and correspondingly the maximum operating temperature was higher. However, for later case when the internal heat transfer coefficient stabilized to limiting value and the maximum operating temperature inside the irradiation loop seemed to decrease only as the function of wall temperature. The maximum operating temperature for limiting case is 346.7 K with corresponding wall temperature of 301.2 K.

The maximum operating temperature inside the irradiation loop dropped below the boiling point of water for external heat transfer coefficient of 1000 $W.m^{-2}.K^{-1}$ for this case the avg. wall temperature is 337.8 K.

4.6 Impact of Uranium concentration on limiting internal heat transfer coefficient

As explained in chapter 2.2.1 the heat generation inside the irradiation loop depends on the concentration of uranium nuclei, the neutron flux from the core and the neutron fission cross section of uranium nuclei. In the current setup, the neutron flux from the HOR core is constant. So, the only degree of freedom which would vary heat generation inside the irradiation loop is the concentration of uranium inside the irradiation loop. Hence, it was decided to calculate limiting internal heat transfer coefficient for varying concentrations of uranium.

By combining equation 2.1 and the typical fission heat, the volumetric heat generation rate inside the irradiation loop can be approximately calculated as following

$$q''' = 200.\varepsilon.\sigma.\phi_n.N \qquad \text{in MeV.s}^{-1}\text{.m}^{-3}$$

Figure 4-9 shows different cases of concentration of uranium and corresponding total heat production rate inside the irradiation loop.

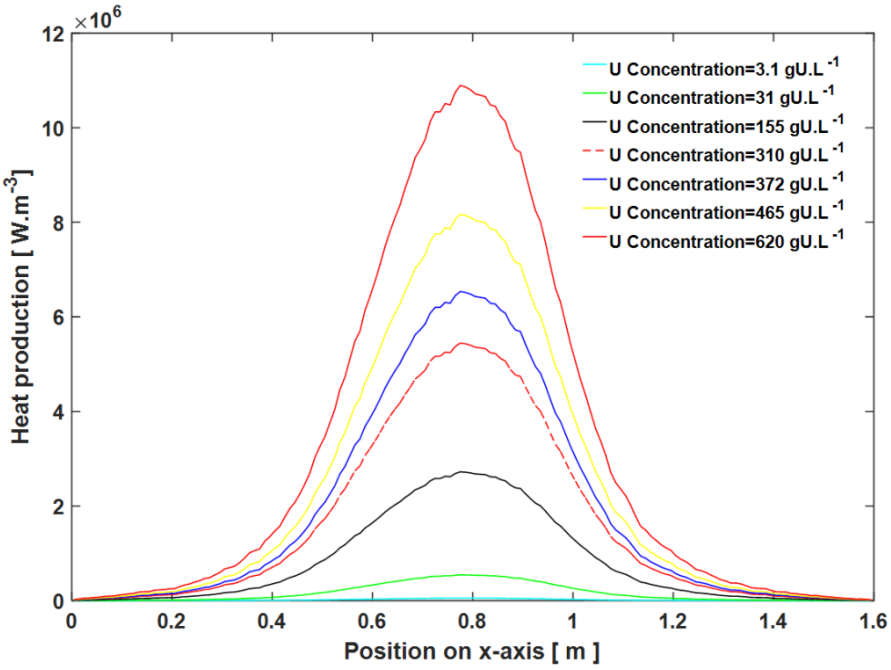

Figure 4-9 Heat generation curve inside the irradiation loop for varying concentration of uranium

Modified Rayleigh number (17) (16)

In a heat generating fluid the final temperature gradient inside the domain is indefinite. Hence, it's not possible to calculate its Rayleigh number and then subsequently other properties. Hence, another form of Rayleigh number is used to estimate heat transfer properties in a heat generating fluid. The modified Rayleigh number (Ra_{M}) can be derived as follows

$$\text{In general, } Ra = \frac{g\beta\Delta T D^3}{\nu\alpha}$$

For a heat generating system

$$H_v D^3 \sim D^2 q'' \sim D^2 k \frac{\Delta T}{D} Nu$$

$$\text{Hence, } \Delta T \sim \frac{H_v D^2}{k}$$

$$Ra_M = \frac{g\beta H_v D^5}{\kappa\nu\alpha} \qquad (4.5)$$

Table 4-6 shows the various cases of uranium concentrations and corresponding volumetric heat generation rate by nuclear fission (H_v) reaction inside the irradiation loop. Here K is the proportionality constant which is used to correlate the concertation of uranium with the heat generation.

$$\mathrm{K} = \frac{\text{uranium concentration in gU.L}^{-1}}{310\ \text{gUL}^{-1}}$$

$$\mathrm{H}_v = \mathrm{K} \times \text{Volume averag heat production during concentration of } 310\ \text{gU.L}^{-1}$$

Table 4-6 Cases modeled to calculate limiting heat transfer coefficient for varying concentration

case	K	Concentration in gU.L^{-1}	H_v W.m^{-3}
1	0.01	3.1	16,441.73
2	0.1	31	164,417.3
3	0.5	155	822,086.5
4	1	310	1,644,173
5	1.2	372	1,973,007.6
6	1.5	465	2,466,259.5
7	2	620	3,288,346

All seven cases listed above were simulated by varying K in UDF. Refer to appendix-D for more detail. For all the cases, the material property such as density, viscosity and heat capacity were assumed same as in Table 4-2. For all other cases listed in Table 4-6 the simulation was carried out by considering h_e =10,000 W.m^{-2}K^{-1} and T_c = 300K.

Table 4-7 shows the result obtained for all the cases. The velocity and temperature profile inside the irradiation loop for all the cases remain identical to Figure 4-6. However maximum temperature, and the average temperature inside the domain varied with the modified Rayleigh number.

Table 4-7 Impact of modified Rayleigh Number

K	Ra_M	$T_{\max}$ K	T_h K	h_i W.m^{-2}.K^{-1}	Nu
0.01	1.38 x 10^{8}	301.5	300.4	437.4	29.6
0.1	1.38 x 10^{9}	308.2	303.0	641.9	43.5
0.5	6.90 x 10^{9}	328.2	312.0	832.8	56.4
1	1.38 x 10^{10}	348.1	321.6	933.2	63.2
1.2	1.66 x 10^{10}	356.6	325.3	962.3	65.1
1.5	2.07 x 10^{10}	367.6	330.5	999.4	67.7
2	2.76 x 10^{10}	385.2	339.04	1049.8	71.1

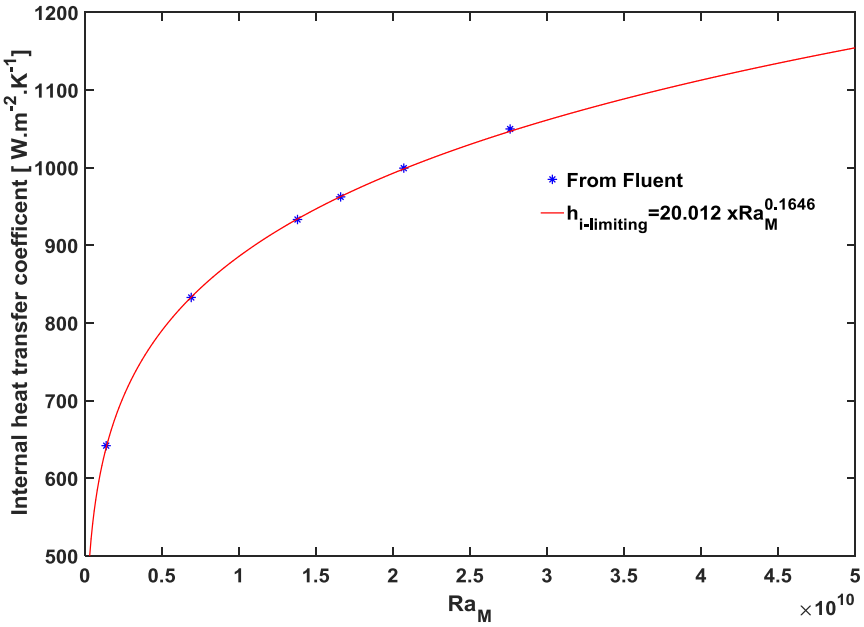

Figure 4-10 Limiting heat transfer coefficient with varying modified Rayleigh number

Using curve fitting regression calculation, a Power Law correlation (R^2 =0.9996) was developed for all the data points. Following equation gives the limiting internal heat transfer coefficient for varying modified Rayleigh number.

$$h_{i\_\text{limiting}} = 20.012 \times Ra_M{}^{0.1646} \qquad (4\text{-}6)$$

The maximum operating temperature inside the irradiation loop increased with the modified Rayleigh number. As the temperatures inside the domain is also a function of surrounding temperature, a more convenient parameter to identify the maximum operating temperature would be the difference between the $T_{\max}$ to the T_c. Figure 4-11 correlates the maximum operating temperature difference to the modified Rayleigh number. Like limiting heat generation rate a Power Law correlation for maximum temperature inside the irradiation loop was calculated. (R^2 =0.996)

$$\Delta T_{\max} = 1.01\times10^{-6} \times Ra_M^{0.7579}$$

$$T_{\max} = 1.01\times10^{-6} \times Ra_M^{0.7579} + T_c \qquad (4.7)$$

The above equation is only valid when the thermal expansion factor is equal to or is more than the defined $5.2 \times 10^{-4}\ K^{-1}$.

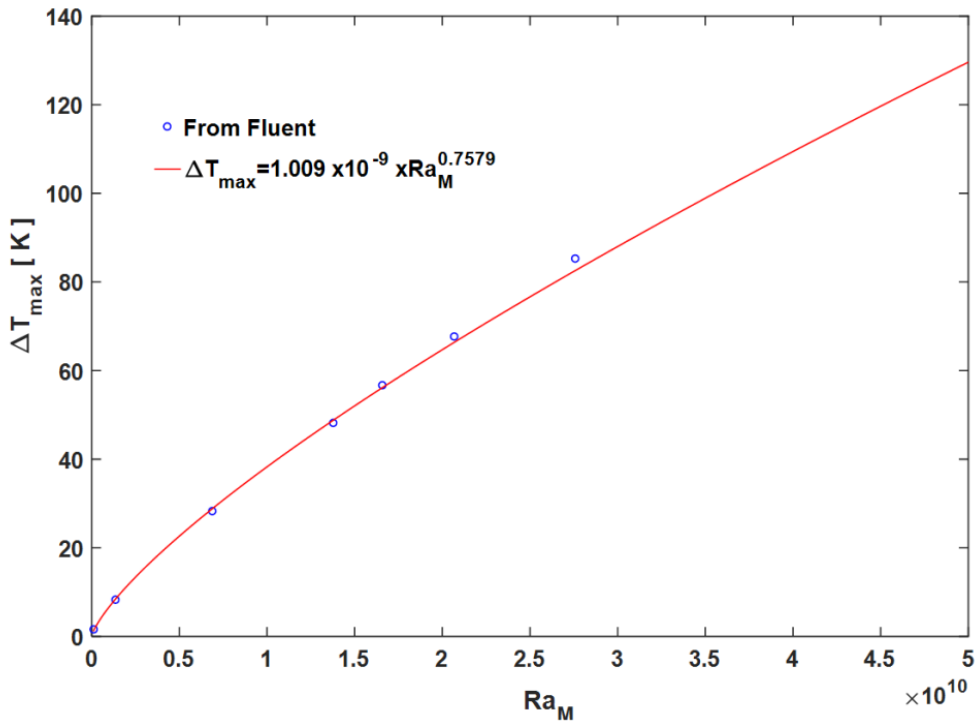

Figure 4-11 Maximum temperature difference in domain varying with modified Rayleigh number

4.7 Conclusion

Unlike chapter 3, where the transverse flow was seen over a plane normal to the axis, in irradiation loop, the non-homogenous heat generation creates recirculating three dimensional flows. These three-dimensional flows seemed to enhance the heat transfer to the surroundings.

The maximum operating temperature inside the irradiation loop dropped below 373 K (100 ^{o}C), when a external heat transfer coefficient of 1000 W.m^{-2}.K^{-1} and higher with surrounding temperature of 300K was applied. Therefore, it can be concluded that the internal heat transfer mechanism is not limiting heat transfer from the irradiation loop and with an effective external cooling mechanism the irradiation loop can be operated at safe temperatures.

Chapter 5

Cooling system for Irradiation Loop

In the last chapter, the internal heat transfer inside the irradiation loop was studied. It was confirmed that for the uranium concentration of 310 gU.L^{-1}, natural convection will not limit heat transfer from the irradiation loop. A correlation between concentration of uranium and limiting heat transfer coefficient was established using the modified Rayleigh number.

The next objective was to design a cooling system around the irradiation loop such that the required external heat transfer mechanism is provided.

5.1 Removal of safety (flood) barrier

Currently the irradiation loop is placed inside a cylindrical flood barrier as shown in Figure 5-1 for protection from spillage in case of a leak. However, the flood barrier adds one more level of resistance for heat transfer. As the flow inside the flood barrier is not enforced by e.g. a pump, heat transfer from the irradiation loop wall to the flood barrier will happen by natural convection. Natural convection inside the flood barrier will depend on the temperature gradient created by the temperature at the wall of the loop and the outer surface of the flood barrier. In following study, we tried to estimate the irradiation loop's wall temperature with respect to the heat transfer coefficient generated in the flood barrier.

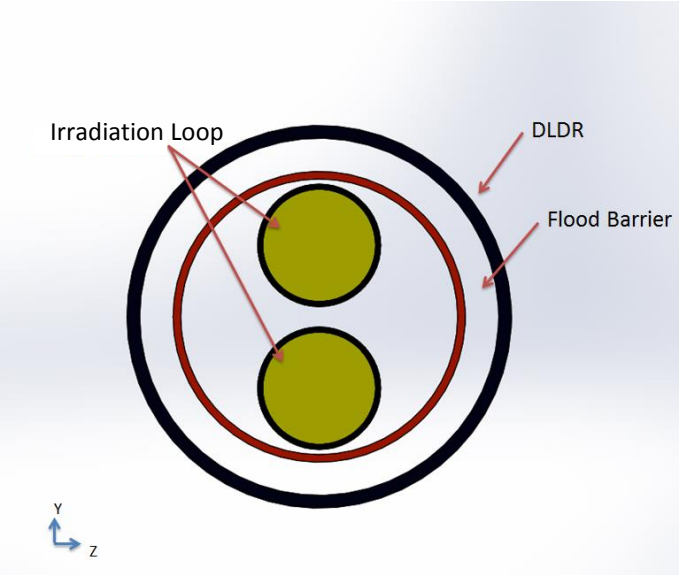

Figure 5-1 Cross sectional view of setup with flood barrier

It was assumed that the Landers empirical correlation of natural convective heat transfer over a horizontal pipe is valid to calculate heat transfer coefficient and wall temperatures in the flood barrier. (18)

$$Nu = 0.12 \times (Ra)^{0.25} \qquad (2.3)$$

$$h = Nu \frac{K}{L}$$

Figure 5-2 shows the development of irradiation loops wall temperature with respect to the heat transfer coefficient developed in flood barrier. During this study, it was assumed that flood barrier's wall temperature is maintained at 283K. The heat transfer coefficient of 1000 W.m^{-2}K^{-1} is achieved only when the temperature at the irradiation loops wall is 373 K. Even if an effective cooling mechanism is

developed over the wall of flood barrier the maximum operating temperature inside the irradiation loop would rise above boiling point of water.

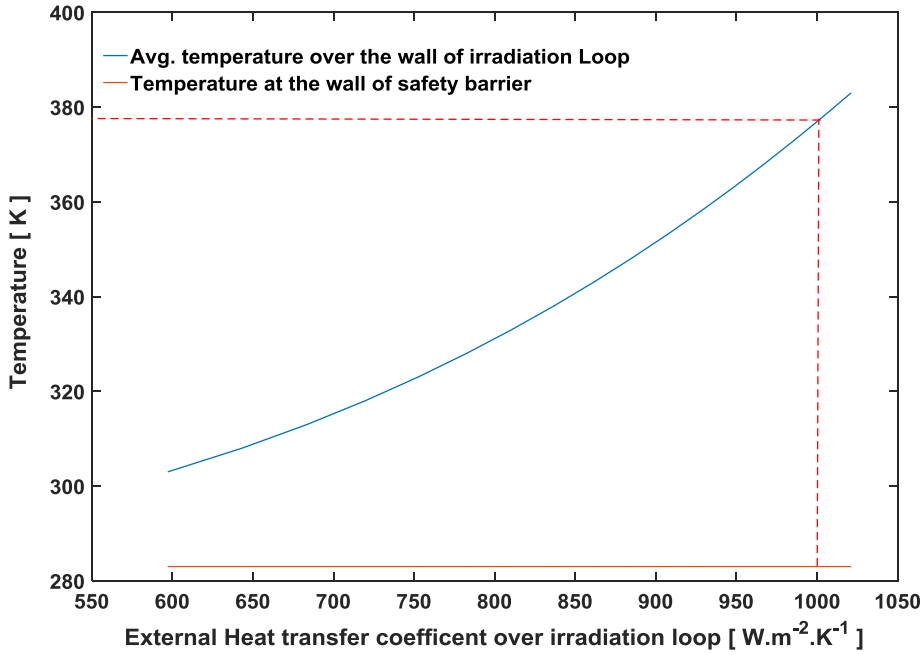

Figure 5-2 Required Temperature distribution over the safety barrier for natural convection vs the external heat transfer coefficient over irradiation loop

Clearly the flood barrier is significantly limiting the heat transfer, and it was decided to remove the flood barrier from the setup. Additionally, removal of flood barrier allows implementation of forced convection over the external surface of the irradiation loop.

5.2 Cooling system setup

The tubular shape of irradiation loop facilitates the possibility of studying the most common heat transfer equipment design of shell and tube heat exchanger. In the setup, the DLDR acts as a shell and the loop as the tube. Figure 5-3 illustrates the representation of the setup where uranyl nitrate solution is flowing in the loop (tube side) and the coolant is flowing in DLDR over the loop wall (shell side). In DLDR, flow of cooling fluid is bounded from both sides by the left direction and right direction flange. Cooling fluid enters at the top nozzle and leaves from the bottom near the right direction flange.

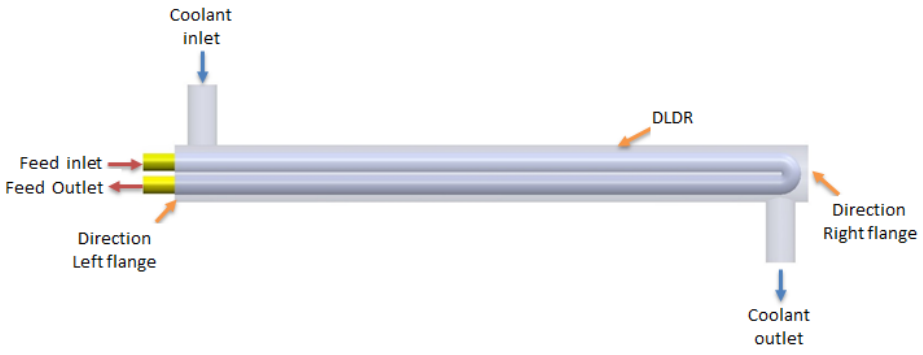

Figure 5-3 Irradiation loop setup with cooling system

Figure 5-4 gives the process scheme envisioned for the cooling system. It is expected that the coolant used would be flowing in a closed loop such that any leakage in the irradiation loop would be detected by a radiation detector and any loss of feed solution can be avoided. As the DLDR is located inside the water pool, the temperature of cooling fluid should be above freezing point of water to avoid any freezing of water over the surface of DLDR. Considering this, chilled water at 10 ^{0}C (283K) was considered as the cooling utility in this study (19). In a shell and tube heat exchanger, baffle usually creates additional turbulence and helps in improving heat transfer. However, as baffles will add another interference for neutron flux, it was decided to avoid installation of baffles inside the DLDR.

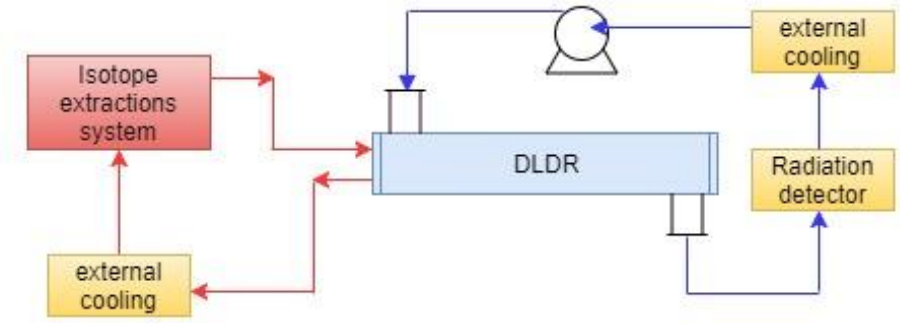

Figure 5-4 Cooling System Design

5.3 Objective

The heat transfer from the irradiation loop mainly depends on three factor's the heat produced in the irradiation loop, the resistance to heat transfer within the loop and the resistance to heat transfer in the cooling media. Moreover, the resistance to heat transfer within the loop cannot be monitored. Hence, the only degree of freedom to change the resistance to heat transfer is in the cooling media. As the resistance to heat transfer will depend directly on the flowrate of chilled water. The following objective was set

''To study the impact of chilled waters flowrate on the heat transfer from the irradiation loop.''

5.4 CFD study

5.4.1 Physical geometry of setup

The DLDR tube has an inner diameter of 140 mm and a length of 1600 mm from direction right flange to direction left flange. Inside the DLDR, the irradiation loop is placed vertically with its open end coming out from the direction left flange and U-bend near direction right flange. The irradiation loop has an inner diameter of 44mm and wall thickness of 2 mm. The length of the irradiation loop at both inlet and at outlet is extended by 80 mm from the direction left flange. The irradiation loop and DLDR are placed such that the gravity is acting in the negative y-direction and the axis of DLDR is the x-axis.

5.4.2 Physical model

The physical geometry of the model was created in SolidWorks software and later exported into the ANSYS workbench. Meshing or grid discretization was carried out using the default ANSYS design modular program. Later the model was imported into ANSYS Fluent and the simulations were carried

out. Due to a possibility of asymmetric flow in the domain, it was decided to model the whole setup instead of assuming a symmetry across the vertical plane. The setup consists of three domains as shown in Figure 5-5. The aluminum pipe of DLDR surrounding the cooling fluid was not modelled instead of that no slip condition with heat flux calculated analytically was incorporated over the interface of cooling fluid.

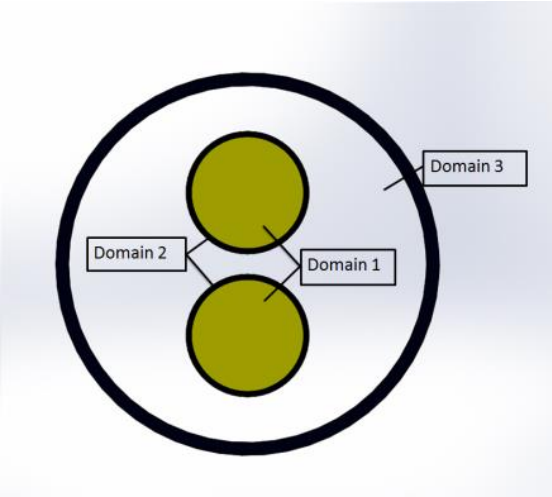

	Type	Material
Domain 1	Fluid	uranyl nitrate aq. solution
Domain 2	Solid	Zircaloy
Domain 3	Fluid	Chilled water

Figure 5-5 Description of domains in setup

Table 5-1 Properties of fluid in each domain

Material	Property	Specification	Unit
Uranyl nitrate solution (Domain 1)	Density	1330.6 (5)	$kg.m^{-3}$
	Specific heat	2905.5 (5)	$J.kg^{-1}K^{-1}$
	Viscosity	0.00122 (5)	$kg.m^{-1}s^{-1}$
	Thermal expansion factor	0.00052	K^{-1}
	Thermal conductivity	0.65	$W.m^{-1}.K^{-1}$
Zircaloy (Domain 2)	Density	6500 (20)	$kg.m^{-3}$
	Specific heat	2850 (20)	$W.m^{-1}.K^{-1}$
	Thermal conductivity	21.5 (20)	$W.m^{-1}.K^{-1}$
Water (Domain 3)	Density	998.5	$kg.m^{-3}$
	Specific heat	4180	$J.kg^{-1}K^{-1}$
	Viscosity	0.001	$kg.m^{-1}s^{-1}$
	Thermal conductivity	0.6	$W.m^{-1}.K^{-1}$

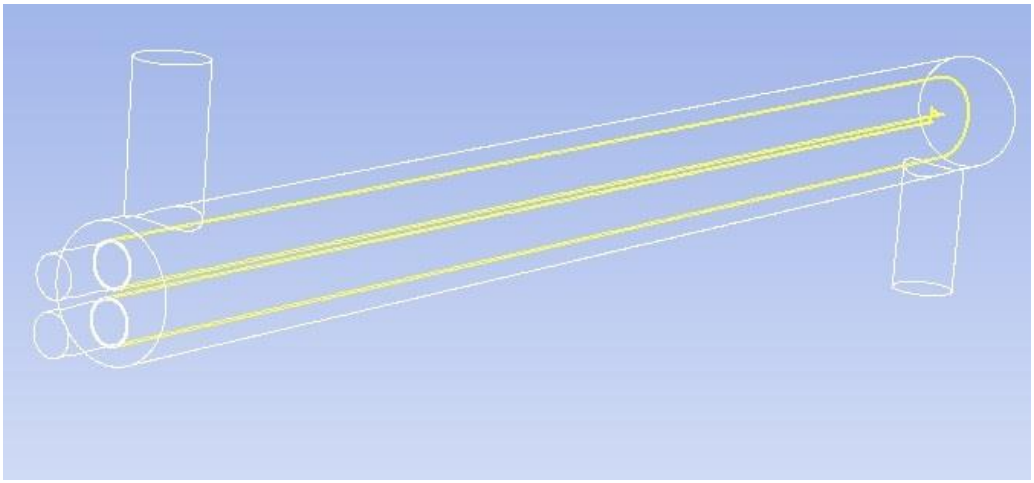

Figure 5-6 Physical model simulated in Fluent

5.4.3 Boundary condition

Table 5-2 Boundary conditions given in Fluent

Name	Type	specification
Feed inlet	Velocity	u_x =0.0002916 m.s^{-1}
	Thermal	T =300K
Feed outlet	Pressure outlet	P = 0 Pa, (refer chapter 5.4.7)
Cold inlet	Velocity inlet	u_y =-0.25 ms^{-1} to -2.25 m.s^{-1}
Cold outlet	Pressure outlet	P = 0 Pa
Fluid-solid interface 1	Mapped walls	$\bar{u} = 0$ (No slip) and $q^{"} = k\nabla T$
Fluid-solid interface 2	Mapped walls	$\bar{u} = 0$ (No slip) and $q^{"} = k\nabla T$
DLDR Tube wall	Wall	$\bar{u} = 0$ (No slip)and note 2

1. The roughness factor considered at the wall is 0.5 with no roughness height (default setting).
2. Heat flux defined using UDF. Refer Appendix D.

5.4.4 Heat sources

1. Due to fission

The heat production due to nuclear fission reaction inside the irradiation loop was modelled using a user defined function. The UDF was created such that the bell-shaped heat generation curve (Figure 2-3) inside the uranyl nitrate solution can be achieved. Appendix-D can be referred to understand how heat source was defined in Fluent.

2. Due to Gamma Heating

The heat deposited over the Zircaloy wall of irradiation loop was also modelled using a UDF. Gamma deposition heat was added as the energy source in domain-2 (tube wall) to model the heat adsorbed from gamma radiation. The user defined function of gamma heating can be found in appendix D.

3. Flux from the DLDR wall

The DLDR pipe is inside a liquid pool. The temperature of the liquid pool is around 40 ^{o}C and the temperature of coolant flowing inside the DLDR is around 10 ^{o}C. This temperature difference will

generate a flux from the water pool. Along with this flux, flux by gamma deposition over the DLDR's aluminum wall was, incorporated as a boundary condition to the walls of domain-3 (chilled water). For details about how user defined function is incorporated refer appendix D.

5.4.5 Simulation Setup

The flowchart explained in Figure 2-7 was followed to export geometry from SolidWorks to run simulations on Fluent. For modelling natural convective laminar flow of uranyl nitrate solution and the turbulent flow of chilled water simultaneously, RNG k-ε model with standard wall function was selected. Refer appendix-F for details. The numerical scheme and the simulation setup validated in chapter 3 was followed. Convergence criteria of 10^{-4} for continuity, velocity and k-ε equation and 10^{-6} for energy equation was followed for the transient analysis till a steady result was achieved.

5.4.6 Mesh independence study

Domain-1 (uranyl nitrate solution) and domain-2 (tubewall) were discretized in structured hexagonal elements. To capture the impact of solid-fluid interface, very thick inflation layer of 15 cells in fluid and 3 inflation layers in solid were added. To reduce number of elements for similar accuracy Domain-3 was discretized in all polyhedral elements with thick inflation layer at the wall of DLDR. (21). Figure 5-7 shows cross sectional view of discretized mesh.

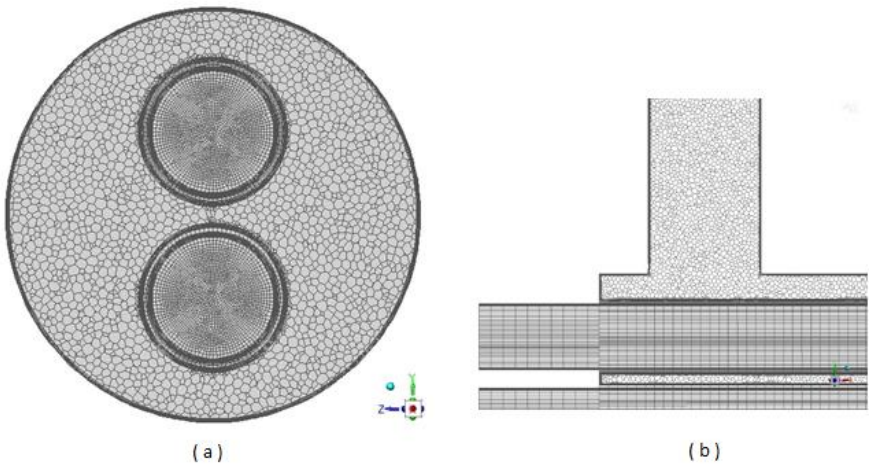

Figure 5-7 Grid discretization of selected mesh for modeling a) front view b) side view

Table 5-3 Mesh independence study

	Number of elements			
	Domain-1	Domain-2	Domain-3	Total
Mesh 1	465840	115200	1348361	1929401
Mesh 2	593320	134400	1649348	2377068
Mesh 3	1794960	259200	4684596	6738756
Mesh 4	1794960	259200	6552820	8606980

Preliminary mesh independence study was carried out to check the dependency of solution on meshing. Four different meshes were developed from coarse to fine as shown in Table 5-3 with 1929401, 2377068, 6738756 and 8606980 elements.

For mesh independence study simulations were carried out at a chilled waters inlet velocity of 2 $m.s^{-1}$. In all meshes, a common trend was observed, the maximum temperature, cup mixing temperature at the outlet of the coolant and the volume average temperature seemed to decrease with an increase in number of elements. The results of meshes 3 & 4 are very close to each other. Also, the current computational hardware available for grid discretization was limiting the creation of finer meshes. Hence, it was decided to use mesh 3 for analysis.

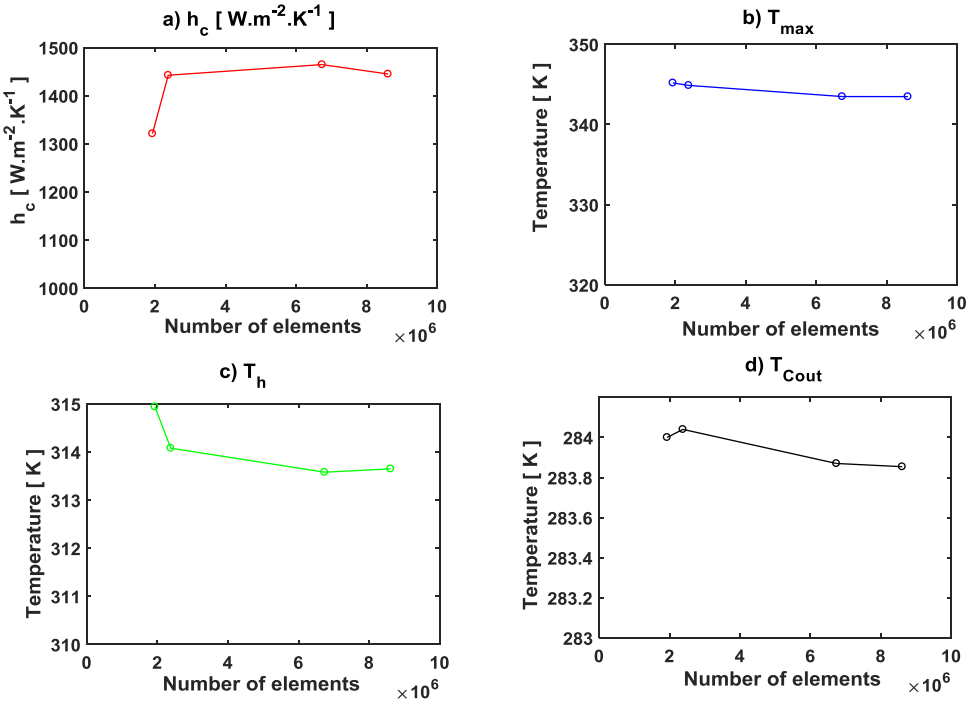

Figure 5-8 Mesh independence analysis

5.4.7 Pressure outlet limitation (10)

One of the major limitations of fluent is that Fluent does not allow to keep any boundary condition other than the pressure outlet for simulating heat transfer across two-fluid domains separated by a solid domain. The pressure outlet boundary condition assumes constant pressure over the entire face of outlet. The pressure outlet boundary condition applies perfectly to the coolant leaving from the domain-3. However, for the uranyl nitrate solution, due to internally recirculating flows and the buoyancy effect, the pressure at the loop outlet face is not constant. A back flow from outside enters the domain-1 from the outlet face. However, the back-flow temperature at the beginning of modelling is not known. The following steps were followed to model and determine the back-flows temperatures for varying flowrate of cooling water.

1) The current set up was modelled for all the cases with the assumption that backflow temperature is 300 K.

2) From the simulation results, the external heat transfer coefficient acting on the irradiation loops outer surface was estimated using equation 5.3.
3) The calculated external heat transfer coefficient and the surrounding temperature of 283 K was applied over the irradiation loop's modelling setup of chapter 4. (only domain-1 of uranyl nitrate solution).
4) From the irradiation loop modeling, the cup mixing (adiabatic) temperature of the fluid leaving from outlet face of loop was calculated using equation 3.9.
5) This temperature at the outlet of irradiation loop from the modeling setup of chapter 4 was defined as the back-flow temperature of the current modeling setup.
6) With this new back flow temperature, the simulations were carried out for all the cases.

Table 5-4 compares the defined back flow temperature with the volume average temperature calculated over the extended portion of loop outside the DLDR left flange. As it can be seen both temperatures are very close and the volume average temperature is 0.2 to 0.3 ^{o}C lower than the back-flow temperature, which means the approach considered is more conservative and it is in a good approximation with the actual result.

Table 5-4 Comparison of Volume average temperature (in K) in the extended portion of loop with the defined backflow temperature (in K)

Case	1	2	3	4	5	6	7	8	9
Volume average temperature	324.1	314.0	311.2	309.4	308.1	307.32	306.3	305.6	305.3
Back flow temperature	324.3	314.2	311.4	309.7	308.4	307.7	306.5	305.8	305.5

5.5 Result & observations

For all cases, transient simulations were carried out till steady state solution is achieved. The inlet velocity at the chilled water inlet nozzle was varied from 0.25 m.s^{-1} to 2.25 m.s^{-1}. For 0.25 m.s^{-1}, maximum operating temperature in the domain was 95 ^{o}C. Since for lower flowrate, the maximum temperature will cross boiling temperature of water, any lower flowrate was not modelled. Since Reynolds number at both the inlet nozzle and outlet nozzle was more than 2000 for all cases, the flow was modelled using a turbulence model (5.4.5).

5.5.1 Flow profile in DLDR

Figure 5-9 illustrates the velocity and streamline profile of cooling fluid flowing in the DLDR over a plane normal to Z axis at z=0. The flow enters the DLDR from the top nozzle and leaves from the bottom. As the cross-sectional area in the vertical portion of the nozzle is smaller than the cross-sectional area of the shell, the flow enters the nozzle with higher velocity and slows down in DLDR. As expected, the pressure drops in the domain increases with the flowrate. Figure 5-10 shows the pressure drop in the cooling fluid. The pressure drop and the Reynolds number curve shows two different regimes. In the first regime for three data points the pressure drop and the Reynolds number appears to follow a linear equation 5.1 (R^2=0.9982). However, from Reynolds number of 13000 onwards (for 11.9 m^3.h^{-1}) the pressure drop follow's a Power Law correlation of equation 5.2 (R^2=0.9924). The Reynolds number is defined based on the outer diameter of loop and chilled water's properties.

$$\Delta P = 0.0782\,\mathrm{Re} - 0.7876 \qquad \text{for Re < 13403 (5.1)}$$

$$\Delta P = 7.63\times10^{-5}\,\mathrm{Re}^{1.73} \qquad \text{13403 <Re > 40208 (5.2)}$$

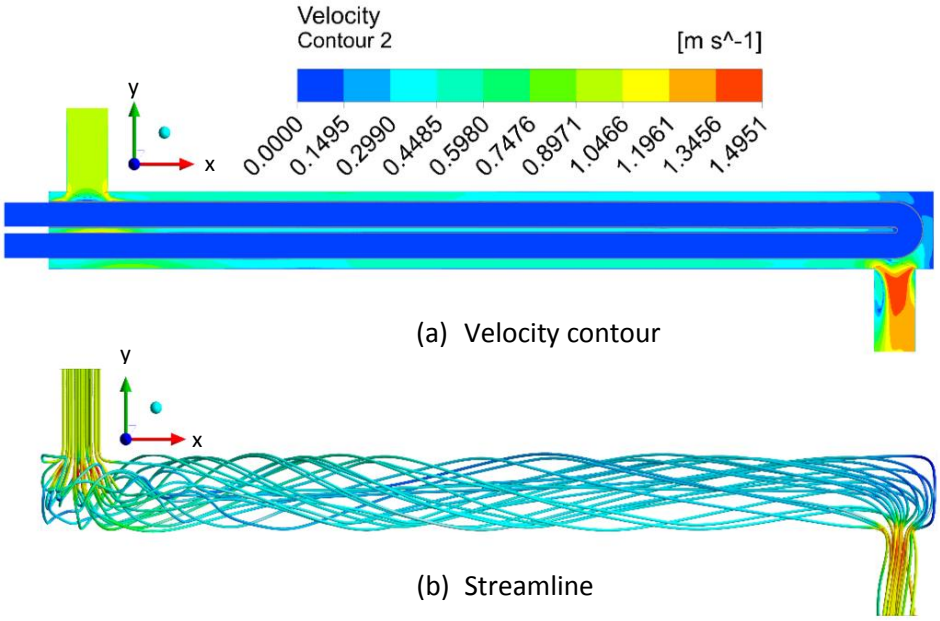

Figure 5-9 Velocity & Streamline profile of chilled water inside the DLDR for flowrate of 11.9 $m^3.h^{-1}$

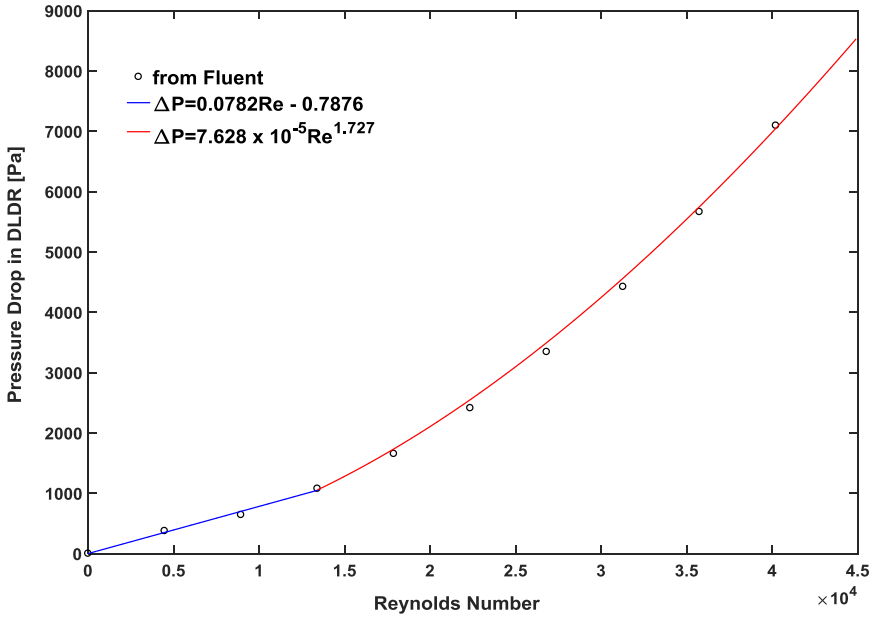

Figure 5-10 Pressure drop across the shell for varying Flowrate of chilled water

5.5.2 Temperature and velocity profile in the irradiation loop

Figure 5-11 shows the temperature, velocity and streamline profile inside the irradiation loop for the flowrate of 15.8 m^3h^{-1} (for the Reynolds number of 17870). The temperature and velocity profile inside the irradiation loop is identical to the temperature and velocity profile found in chapter 4. At the outlet in the extended tube outside the DLDR left flange some back flow could be observed as described earlier. This back flow entering the domain changes the velocity profile locally from the observed velocity profile in Figure 4-6 (b).

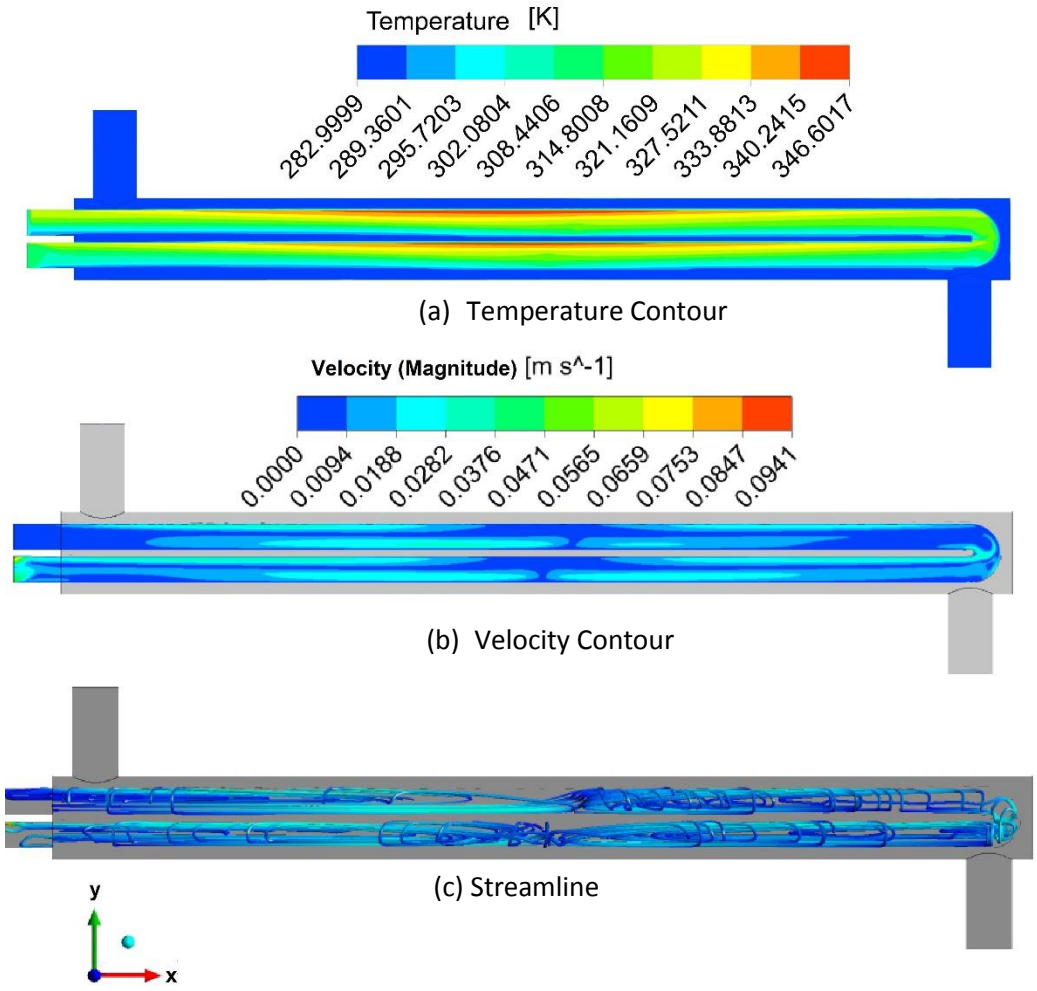

Figure 5-11 Flow profile inside irradiation loop for flowrate of 15.8 $m^3.h^{-1}$ (a) Temperature profile (b) Velocity Profile (c) Streamline profile

5.5.3 Heat Transfer analysis

5.5.3.1 Internal Heat transfer coefficient

To calculate internal heat transfer coefficient a similar approach to chapter 4 was taken. The internal heat transfer coefficient and all other related parameters were calculated using equation 4.2, 4.3 & 4.4.

Table 5-5 Impact of varying chilled water flowrate

Case	u_{cin} m.s^{-1}	Flowrate m^3.h^{-1}	Re	ΔP Pa	T_{max} in K	v_{max} in m.s^{-1}
1	0.25	4.0	4468	375	368.8	0.4
2	0.5	7.9	8935	642	354.2	0.9
3	0.75	11.9	13403	1076	349.6	1.4
4	1.0	15.8	17870	1654	346.7	1.8
5	1.25	19.8	22338	2412	344.7	2.4
6	1.5	23.7	26805	3343	343.35	3.02
7	1.75	27.7	31273	4422	342.3	3.6
8	2.0	31.6	35740	5663	341.3	4.2
9	2.25	35.6	40208	7093.5	340.8	4.8

5.5.3.2 External Heat transfer coefficient

The heat flux from the irradiation loop faces resistances in both solid domain of Zircaloy and the fluid domain of chilled water. Hence the total external heat transfer coefficient (h_e) acting over uranyl nitrate fluid domain was defined by adding the resistances in domain-1 and domain -2.

$$\frac{1}{h_e} = \frac{1}{h_c} + \frac{t_z}{k} \qquad (5.3)$$

Here h_c is the heat transfer coefficient of cooling fluid, t_z is thickness of Zircaloy wall and k is the thermal conductivity of Zircaloy. Equation 5.4 defines the heat transfer coefficient of chilled water to estimate the resistance to flow in the cooling system. External heat transfer coefficient was calculated by the average temperature in the cold domain (T_c) and by the average temperature over the outer wall of the tube (T_{wc}).

$$h_c = \frac{q_{wc}''}{A_{wc}.(T_{wc} - T_c)} \qquad (5.4)$$

The average temperature of the cold domain was calculated as the mean temperature of the flow entering and leaving the domain.

$$T_c = \frac{1}{2}.\left(\frac{\int_{A_{Cout}} v_y T dA_{Cout}}{\int_{A_{Cout}} v_y dA_{Cout}} + T_{Cin} \right) \qquad (5.5)$$

Where $Cout$ and Cin suffix corresponds to the cooling fluid outlet and cooling fluid inlet nozzle surface. Figure 5-12 shows the variation in internal and external heat transfer coefficient inside the irradiation loop with respect to the flowrate of chilled water. As expected, the external heat transfer coefficient

increases with an increase in Reynolds number. For all nine data points, a Power Law correlation was established between external heat transfer coefficient and the Reynolds number (R^2=0.9991).

$$h_c = 4.216\,\mathrm{Re}^{0.603} \qquad (5.6)$$

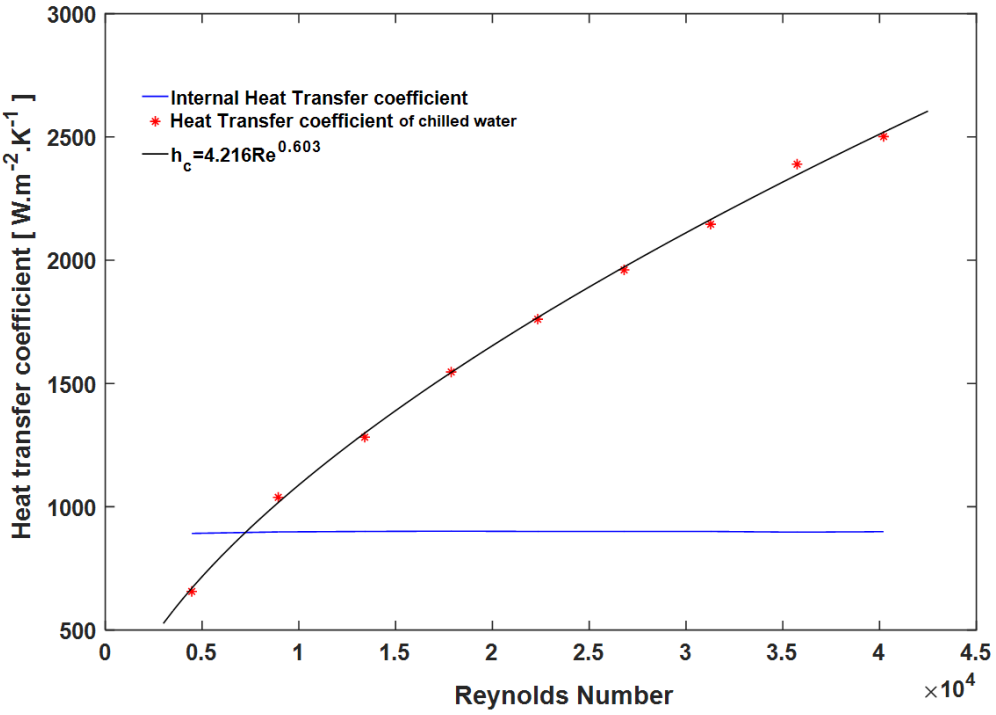

Figure 5-12 impact of Reynolds number on heat transfer coefficient of chilled water

Up to 11.9 $m^3.h^{-1}$ the internal heat transfer coefficient increases from 891 $W.m^2.K^{-1}$ to 900 $W.m^2.K^{-1}$. At lower velocities, the change in internal heat transfer coefficient is due to increase in external heat transfer coefficient, the temperature distribution over the walls of irradiation loop is governed by external mechanism. From 11.9 $m^3.h^{-1}$ ($Bi_s > 1$) onwards, as h_e increases natural convection starts governing the temperature distribution over the wall's. Hence, change in h_i with respect to h_e is less.

5.5.4 Overall heat transfer coefficient

Heat generation occurs inside the irradiation loop by nuclear fission and over the irradiation loop wall by gamma radiation. Hence, the heat flux across the composite domains is different. Hence, equation 5.7 is used to calculate the overall heat transfer coefficient

$$U = \frac{q''_{wc}}{A_{wc}.(T_h - T_c)} \qquad (5.7)$$

Figure 5-13 illustrate the impact of the flowrate variation on the overall heat transfer coefficient. Using curve fitting, a Power Law correlation was established for all the data points.

$$U = 51.489\,\mathrm{Re}^{0.2382} \qquad (5.8)$$

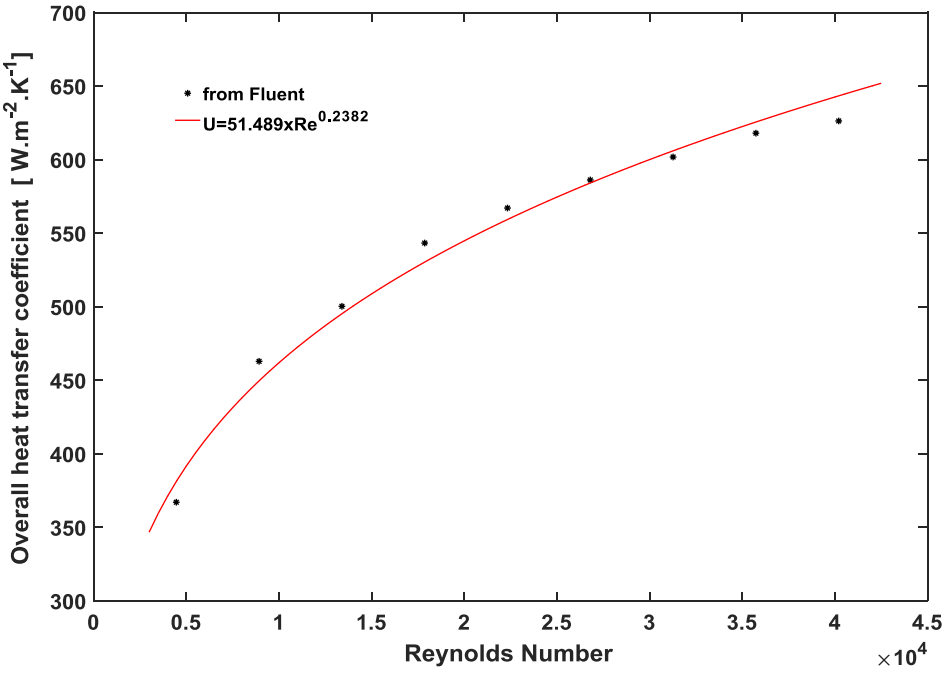

Figure 5-13 Impact flowrate on overall heat transfer coefficient

Table 5-6 Impact of cooling fluid variation on overall heat transfer

Case	u_{cin} m.s^{-1}	ϕ_i m^3.h^{-1}	Re	T_h K	T_{wh} K	T_{wc} K	T_c K	h_i W.m^{-2}.K^{-1}	h_c W.m^{-2}.K^{-1}	h_e W.m^{-2}.K^{-1}	U W.m^{-2}.K^{-1}
1	0.25	4.0	4468	333.6	313.9	312.3	285.3	891.6	656.5	618.7	367.1
2	0.5	7.9	8935	322.6	302.9	301.3	284.1	898.3	1038.2	946.8	462.9
3	0.75	11.9	13403	319.3	299.7	297.6	283.8	899.8	1282.1	1145.5	500.3
4	1	15.8	17870	316.6	296.8	295.2	283.6	900.8	1546.7	1352.2	543.3
5	1.25	19.8	22338	315.1	295.3	293.6	283.4	900.2	1760.7	1512.9	567.1
6	1.5	23.7	26805	314.0	294.2	292.5	283.4	900.1	1960.7	1658.3	586.2
7	1.75	27.7	31273	313.1	293.3	291.7	283.3	900.2	2146.0	1788.9	601.8
8	2	31.6	35740	312.3	292.5	290.8	283.3	897.0	2389.5	1954.9	618.0
9	2.25	35.6	40208	311.9	292.1	290.4	283.2	899.2	2501.7	2029.4	626,3

5.6 Impact of chilled waters flowrate on maximum operating temperature

Figure 5-14 illustrates the variation in maximum temperature inside the irradiation loop with varying Reynolds number (flowrate). The maximum operating temperature curve shows two different

regimes. At flowrate lower than 11.9 $m^3.h^{-1}$, T_{max} seems to be more sensitive to the cooling water velocities. This is due to low specific Biot number and non-optimized wall temperature distribution at $Bi_s \leq 1$. Since only three data points were available a second order polynomial correlation was established to estimate the temperature of the hot spot in the irradiation loop. From 11.9 $m^3.h^{-1}$ (Re 13403) up to 35.6 $m^3.h^{-1}$, the hot spot temperature reduces but the temperature variation is less sensitive to the velocity change. The improved wall temperature distribution at $Bi_s > 1$ makes the maximum temperature less sensitive to change in velocity.

$$T_{max} = 2.5\times10^{-7}\,\mathrm{Re}^2 - 0.0066\,\mathrm{Re} + 393.41 \qquad \text{Re} < 13407 \quad (5.9)$$

$$T_{max} = 435.93\,\mathrm{Re}^{-0.02334} \qquad 13403 < \text{Re} > 40208 \quad (5.10)$$

The irradiation loop must be operated in the second regime (equation 5.10) as in this regime the maximum operating temperature is less sensitive to fluctuations in the flowrate. For chilled water, the flowrate of 15.8 $m^3.h^{-1}$ (Re 17870) provides a maximum temperature of 73.7 ^{o}C, which is a safe temperature for operating the irradiation loop.

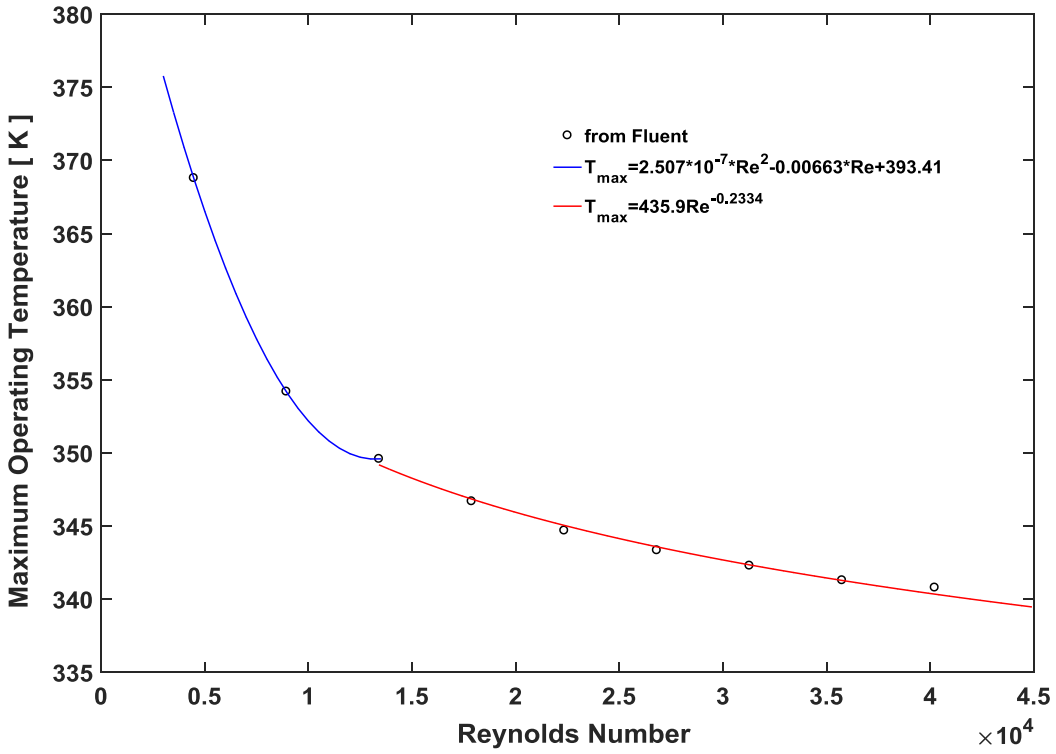

Figure 5-14 Maximum temperature vs Reynolds number

5.7 Conclusion

The safety (flood) barrier added inside the DLDR for protection from any leakage adds additional resistance for heat removal from irradiation loop. Moreover, it facilitates heat transfer only by natural convection. For heat removal, natural convection requires high temperature gradient in between the

irradiation loop wall and the inner wall of safety barrier. This would rise the temperature inside the irradiation loop above critical temperature. Hence, it was decided to remove the safety barrier.

The cooling mechanism around the irradiation loop was adopted from the most common heat transfer equipment being a shell and tube heat exchanger where the irradiation loop acts like a tube while the DLDR acts as a shell with cooling fluid. Chilled water at $10^{o}C$ (283 K) is considered as the cooling fluid in DLDR.

CFD analysis of envisaged setup was carried out to identify the operating point for cooling system. chilled water's flowrate was varied from 4 $m^3.h^{-1}$ to 35.6 $m^3.h^{-1}$. At 15.8 $m^3.h^{-1}$ of chilled water flowrate the maximum operating temperature is 73.8 ^{o}C and the maximum operating temperature in this range is less sensitive to fluctuations in flowrate. Hence the cooling system can be operated at 15.8 $m^3.h^{-1}$ of chilled water flowrate.

Chapter 6

Redesigned irradiation loop

During initial study Elgin optimized the uranyl nitrate solutions flowrate based on the minimum time required to extract ^{99}Mo from the extraction column. Hence, an irradiation time of 3 hours was confirmed. However, now a different technique of isotope extraction is under investigation which does not follow this limitation.

In earlier setup, the irradiation time of 3 hrs. was maintained using a pump. However, the pump used for monitoring the flow inside irradiation loop creates complications like possibility of leakage or difficulty in removal of gas bubbles formed inside the uranyl nitrate solution. The pump creates a hindrance for natural convection by controlling the axial flow. Hence, to avert these constraints it was decided to remove the pump and connect both the extended legs of loop as shown in Figure 6-1. In this chapter, the prospect of using this new design was explored.

6.1 Redesigned irradiation loop geometry and setup

In this setup, the extended length of the irradiation loop coming out from the DLDR left flange, is connected back to the inlet of the loop. In such assembly, the flow of uranyl nitrate solution inside the loop will not be monitored by a pump. The flow field inside the irradiation loop will entirely depend on the natural convection created by the temperature gradient. Moreover, the flow will vary depending on the heat generation and the resistance to heat transfer in the cooling media.

In such setup, isotopes produced would be extracted by taking out tapping from the extended pipe coming out from left flange of DLDR. The Design of cooling system around the loop is the same as the previous setup from chapter 5. In a closed domain, the fluctuations in temperature will fluctuate system volume and such fluctuations would cause over-pressure inside the irradiation loop. This limitation can be prevented by a pressure balancing line, which will equalize the fluctuation in the total volume of the system by exerting a constant pressure using inert gas like N_2.

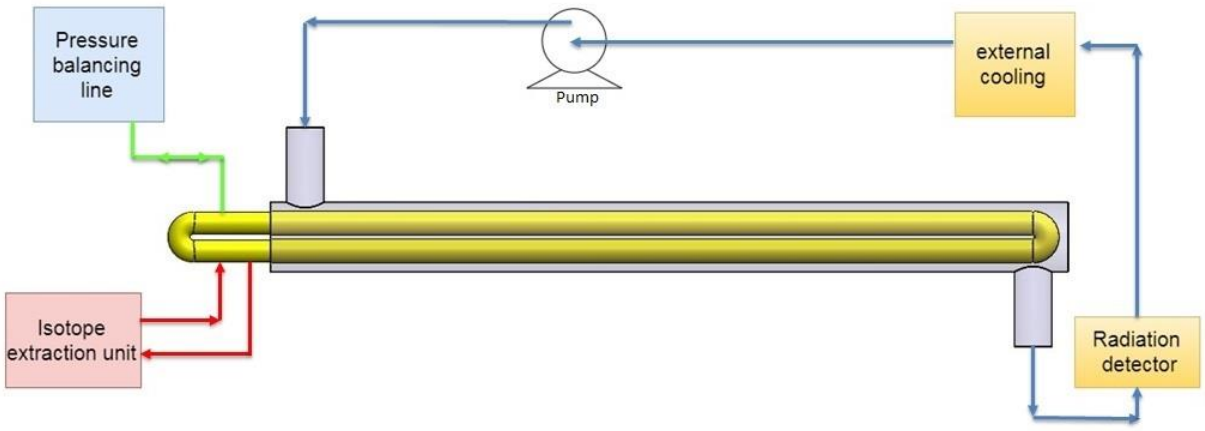

Figure 6-1 Process Flow Scheme for redesigned irradiation loop

Table 6-1 Comparison of both designs

Redesigned setup	Earlier setup
Flow inside the loop is formed by natural convection.	Pump monitors a constant axial flowrate.
All the heat generated by nuclear fission reaction and gamma deposition would be extracted by the cooling system.	Requires an additional heat exchanger to cool down the solution leaving from loop.
The pressure balancing line facilitates removal of gas bubbles formed due to the low irradiation stability of uranyl nitrate.	Gasses formed in the uranium nitrate solution are difficult to remove.
Any Fluctuation in the solution volume can be accommodated by the pressure balancing line.	Fluctuation in solution volume will create over pressure scenario.

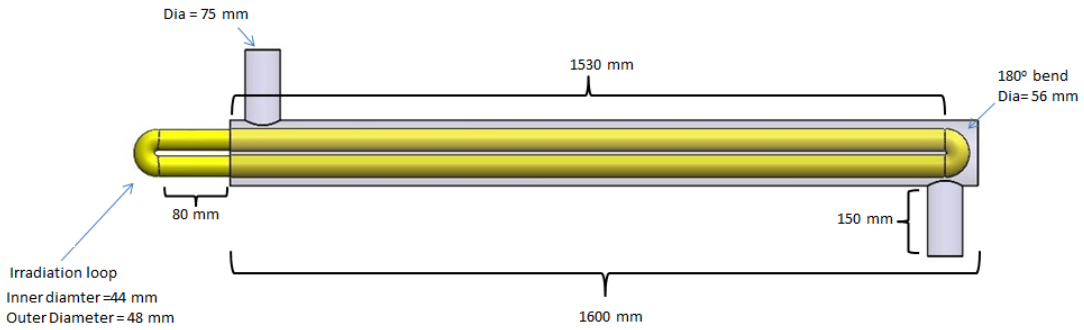

Figure 6-2 Geometry of the redesigned irradiation loop setup

6.2 Objective

After removal of pump, the only driving force for any flow in the irradiation loop is natural convection. Since temperature and the flow distribution inside the loop depends upon the heat generation inside the loop and the resistance to heat transfer in the cooling media. The heat transfer in chilled water is by forced convection and it varies with the chilled waters flowrate. Hence, CFD analysis of the new setup with varying chilled water flowrate was carried out to investigate the operating range of cooling system.

"To study the impact of chilled waters flowrate on the heat transfer from the redesigned irradiation loop based on natural convection"

6.3 CFD setup

6.3.1 Physical geometry of setup

The geometry of the setup was created in SolidWorks and later exported to ANSYS workbench. The DLDR tube has an inner diameter of 140 mm and its length is 1600 mm from direction right flange to direction left flange. Inside the DLDR the irradiation loop is placed vertically with its one end coming out from the direction left flange. In the physical geometry modelled, the extended U-shaped loop coming out from the DLDR is extended by 80mm. Rest of the dimension of the geometry are like the setup studied in the previous chapter 5.

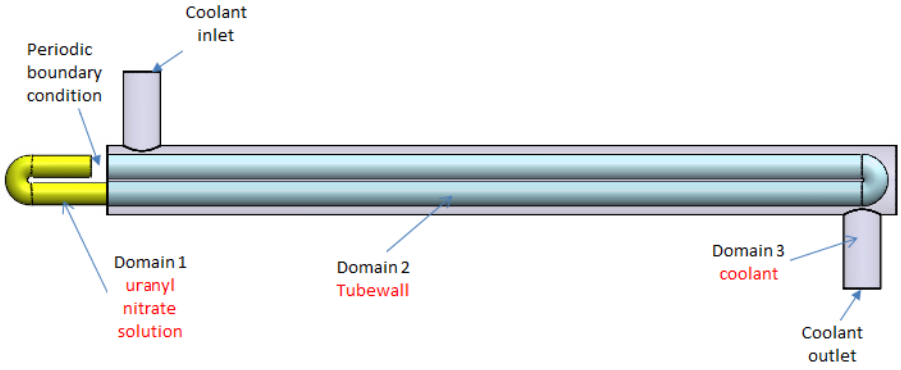

Figure 6-3 Physical model of the redesigned setup modelled

6.3.2 Physical model

The physical geometry of the model was created in SolidWorks software and later it was exported in to the ANSYS workbench. Grid discretization was carried out using the default ANSYS designer modular program. Later the model was imported into ANSYS Fluent and the simulations were carried out. The physical model consists of three domains as shown in Figure 6-4. Fluid Domain-1 of uranyl nitrate solution, solid domain-2 of Zircaloy loop and the chilled waters fluid domain-3. The aluminum pipe of DLDR surrounding the cooling fluid was not modelled instead of that no slip condition with heat flux calculated analytically was assumed over the interface of cooling fluid.

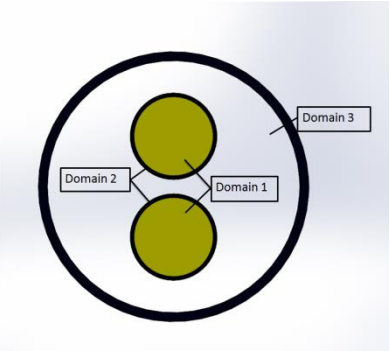

Figure 6-4 Description of domains

Table 6-2 Properties of fluid in each domain

Material	Property	Specification	unit
Uranyl nitrate Solution (Domain 1)	Density	1330.6 [2]	$kg.m^{-3}$
	Specific heat	2905.5 [2]	$J.kg^{-1}K^{-1}$
	Viscosity	0.00122 [2]	$kg.m^{-1}s^{-1}$
	Thermal expansion coefficient	0.00052	K^{-1}
	Conductivity	0.65	$W.m^{-1}.K^{-1}$
Zircaloy (Domain 2)	Density	6500 [3]	$kg.m^{-3}$
	Specific heat	2850 [3]	$W.m^{-1}.K^{-1}$
	Conductivity	21.5 [3]	$W.m^{-1}.K^{-1}$
Water (Domain 3)	Density	998.5	$kg.m^{-3}$
	Specific heat	4180	$J.kg^{-1}K^{-1}$
	Viscosity	0.001	$kg.m^{-1}s^{-1}$
	Conductivity	0.6	$W.m^{-1}.K^{-1}$

Table 6-3 Boundary conditions defined in Fluent

Name	Type	Specification
Feed inlet	Translational periodic	ΔP =0 Pa
Feed outlet		
Cold inlet	Velocity inlet	u_y = -0.25 to -2.25 m.s^{-1}
Cold outlet	Pressure outlet	P =0 Pa
Fluid solid interface 1	Mapped walls	$\bar{u} = 0$ (No slip) and $q'' = k\nabla T$
Fluid solid interface 2	Mapped walls	$\bar{u} = 0$ (No slip) and $q'' = k\nabla T$
DLDR tube wall	Wall	$\bar{u} = 0$ (No slip) and note 2

1. The roughness factor considered at the all the wall is 0.5 (default) with no roughness height.
2. Heat flux is defined using an UDF. Refer Appendix D.

6.3.3 Heat source

All three heat sources were defined same as chapter 5.4.4.

6.3.4 Numerical scheme

The flowchart explained in Figure 2-7 was followed to export geometry from SolidWorks to run simulations on Fluent. For modelling, natural convective laminar flow of uranyl nitrate solution and the turbulent flow of chilled water simultaneously, RNG k-ε model with standard wall function was selected. Refer appendix-F for more details. The numerical scheme and the simulation setup validated in chapter 3 was followed. Convergence criteria of 10^{-4} for continuity, velocity and k-ε equation and 10^{-6} for energy equation was followed for a transient analysis till a steady result was achieved.

6.3.5 Mesh independence study

Domain-1 (uranyl nitrate solution) and domain-2 (tube wall) were discretized in structured Hexagonal elements. To capture the impact of solid-fluid interface very thick inflation layer of 15 cell in fluid domain-1 and 3 cells in solid domain-2 was formed. Domain -3 was discretized in unstructured polyhedral elements with thick inflation layer of 10 cells at the walls of DLDR and at the wall of the tube. (22) Figure 7 shows cross sectional view of discretized mesh.

Preliminary mesh independence study was carried out to check the dependence of solution on meshing. Five different meshes were developed with coarse to fine as shown in Table 6-4 with 2588125, 2934854, 5523894, 6375138, 7692008 elements.

Table 6-4 Mesh independence study

	Number of elements			
	Domain-1	Domain-2	Domain-3	Total
Mesh 1	1141200	88592	1358333	2588125
Mesh 2	1323201	158400	1453253	2934854
Mesh 3	1749825	203520	3570549	5523894
Mesh 4	1749825	203520	4421793	6375138
Mesh 5	2276615	274428	5140965	7692008

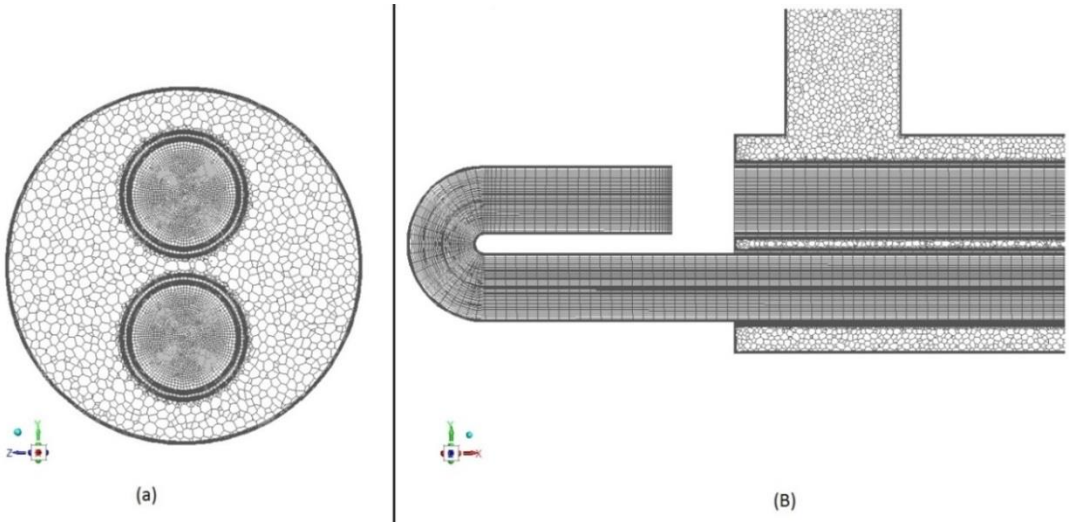

Figure 6-5 Grid Discretization in the selected mesh (a) Cross sectional view on the y-z plane (b) Side view form the x-y plane

A common trend was observed for all the meshes the maximum temperature, the bulk temperature at the outlet of the coolant and the volume average temperature seemed to decrease with increase in number of elements. The results of mesh 3, 4 & 5 shows minor difference. Also, the current computational hardware available for grid discretization was limiting creation of finer mesh. Hence, it was decided to use mesh 3 for analysis.

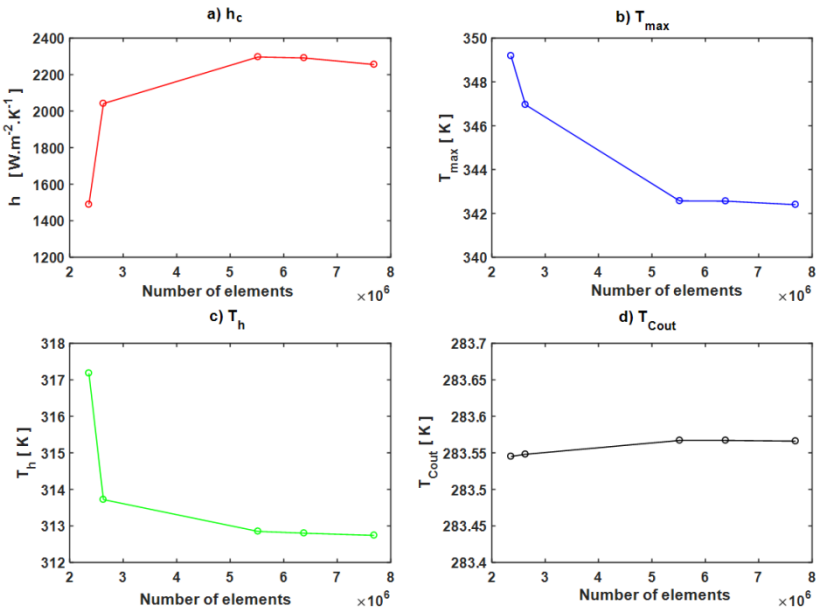

Figure 6-6 Mesh independence study results

6.4 Result and observations

The flow and temperature field inside the irradiation loop was investigated by varying the chilled waters flowrate from 0.25 $m.s^{-1}$ to 2.25 $m.s^{-1}$. Figure 6-7 illustrates the temperature and heat generation profile inside the irradiation loop for chilled water flowrate of 19.8 $m^3.h^{-1}$. Temperature profiles inside the current setup design are identical to the earlier design. As expected, part of the loop in front of the reactor core corresponds to the maximum temperature. In current setup, as all the heat generated by nuclear fission and gamma deposition is taken out by the cooling system, the overall temperature's inside the loop are slightly higher (by roughly 1^oK) than earlier setup.

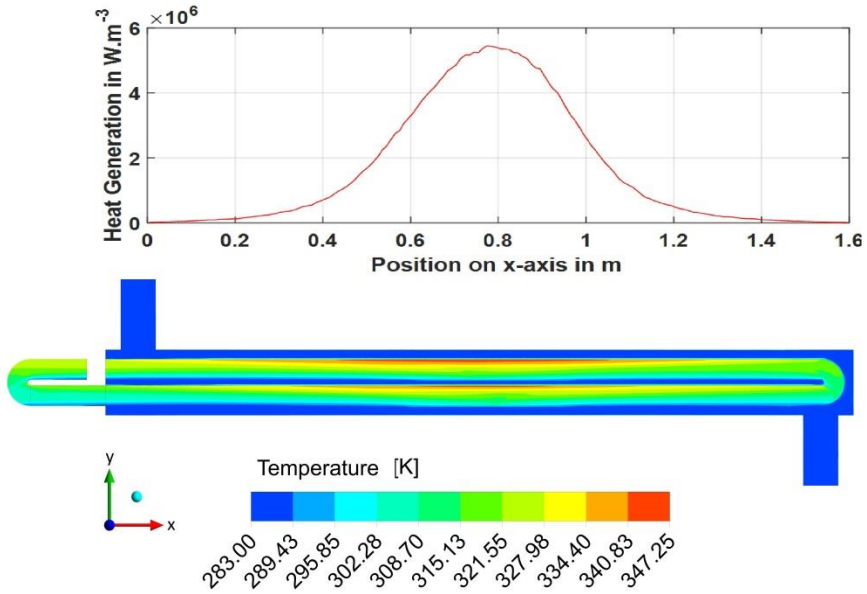

Figure 6-7 Temperature profile inside the new setup of irradiation loop for chilled water flowrate of 19.8 $m^3.h^{-1}$

In Figure 6-8 (b) of earlier setup shows that the bell-shaped heat generation creates four different zones of internal circulation. In earlier setup, as the external pump monitors the axial flow to maintain 3 h's of irradiation time, overall axial velocity is low and the four circulation zones are more distinct.

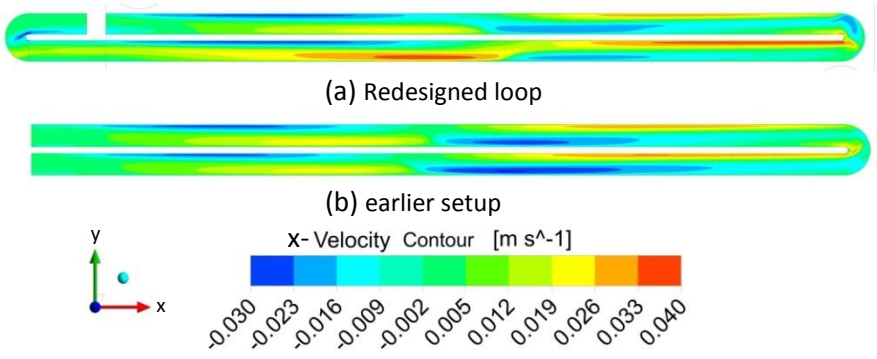

Figure 6-8 Comparison of x- Velocity contour

In the redesigned loop Figure 6-8 (a), the fluid in the irradiation loop follows two circulation patterns. One circulation like the one observed in earlier setup, where the flow is circulating in zones along the upward or downward slopping heat generation curve. The other circular motion is over the entire loop in an anti-clockwise direction. Similar observations could be made from streamline profile (Figure 6-9), fluid in the redesigned setup is rotating internally in circulation zones and along the entire loop.

The anticlockwise rotation is due to the imbalance of heat generation between the extended portion of the loop with the irradiated portion. The fluid in right is internally heating so it would tend to move up however the fluid outside DLDR (left side) is not being internally heated and will not experience buoyant force. This imbalance will create a flow such that the fluid in the right will tend to move up and due to continuity, the fluid in the left will move in right direction, creating an anti-clockwise motion.

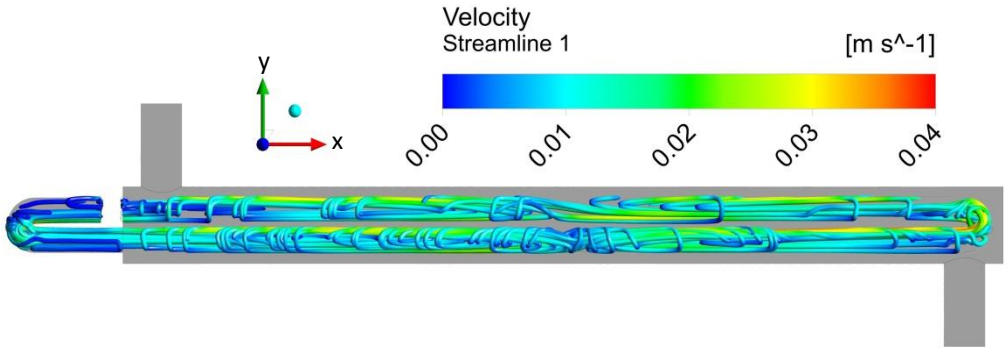

Figure 6-9 Streamline profile inside irradiation loop for chilled water flowrate of 19.8 $m^3.h^{-1}$

6.4.1 Impact of varying the chilled water flowrate

The impact of the chilled water flowrate on the irradiation loop temperature was investigated in nine cases by varying the chilled waters velocity at the inlet nozzle from 0.25 $m.s^{-1}$ to 2.25 $m.s^{-1}$ as shown in Table 6-5

Table 6-5 Impact of varying chilled water flowrate

case	u_{cin} $m.s^{-1}$	ϕ_i $m^3.h^{-1}$	Re	T_{max} K	T_h K	T_{wh} K	T_{wc} K	T_c K	h_i $W.m^{-2}.K^{-1}$	h_c $W.m^{-2}.K^{-1}$	h_e $W.m^{-2}.K^{-1}$	U $W.m^{-2}.K^{-1}$	ϕ_m * $kg.s^{-1}$ $x10^{-4}$
1	0.25	4.0	4468	368.6	332.4	312.7	310.6	287.5	921.8	719.6	674.5	387.1	8.102
2	0.5	7.9	8935	358.1	323.9	304.3	302.2	283.3	927.3	956.7	878.5	447.7	8.137
3	0.75	11.9	13403	352.5	319.6	300.2	298.0	284.5	933.0	1280.5	1144.2	508.5	7.716
4	1	15.8	17870	349.3	317.1	297.7	295.6	284.1	934.0	1513.0	1326.3	543.3	7.467
5	1.25	19.8	22338	347.4	315.5	296.1	293.9	283.9	934.6	1751.7	1506.2	569.4	7.299
6	1.5	23.7	26805	345.8	314.3	294.9	292.7	283.8	935.2	1964.4	1660.9	590.3	7.144
7	1.75	27.7	31273	344.4	313.2	293.9	291.7	283.6	937.9	2189.5	1819.0	610.3	7.114
8	2	31.6	35740	343.5	312.5	293.2	290.9	283.6	938.2	2387.2	1953.4	624.7	7.047
9	2.25	35.6	40208	342.7	311.9	292.5	290.3	283.5	938.5	2591.5	2088.1	637.9	6.931

* ϕ_m is the mass flowrate of uranyl nitrate solution at the feed inlet boundary

6.4.2 Heat transfer calculation

External and Internal heat transfer coefficients inside the setup were calculated with the similar approach of chapter 5. As the design, operating fluid and the flowrate of cooling system considered in current study and the previous study is the same, the resistance to heat transfer offered by the cooling media remains the same. Hence, the same Power Law correlation in Eq. 5.6 applies for current setup.

$$h_c = 4.216\,\mathrm{Re}^{0.603}$$

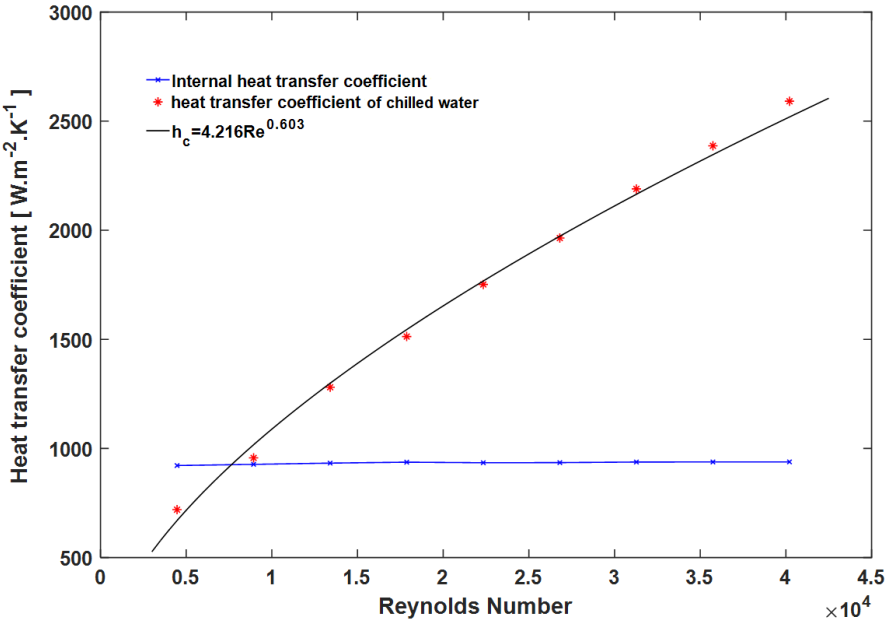

Figure 6-10 Impact of Reynolds number on heat transfer coefficient of chilled water

Similar to chapter 4, even in this study, the internal heat transfer coefficient changes from 921 $W.m^{-2}K^{-1}$ to 937 $W.m^{-2}.K^{-1}$ and then changes marginally for any change in external heat transfer coefficient. At lower velocities, up to 11.9 $m^3.h^{-1}$, the change in internal heat transfer coefficient is due to increase in external heat transfer coefficient, the temperature distribution over the walls of irradiation loop is governed by external mechanism. From 11.9 $m^3.h^{-1}$ ($Bi_s > 1$) onwards, as h_e increases natural convection starts governing the temperature distribution over the wall's. Hence, change in h_i with respect to h_e is less.

6.4.3 Overall heat transfer coefficient

An approach Similar to chapter 5 was taken to calculate overall heat transfer coefficient. Figure 6-11 shows the impact of varying chilled water flowrate on overall heat transfer coefficient. A Power Law correlation was established between the overall heat transfer coefficient and the Reynolds number of chilled water.

$$U = 51.489\,\mathrm{Re}^{0.2382} \qquad (6.3)$$

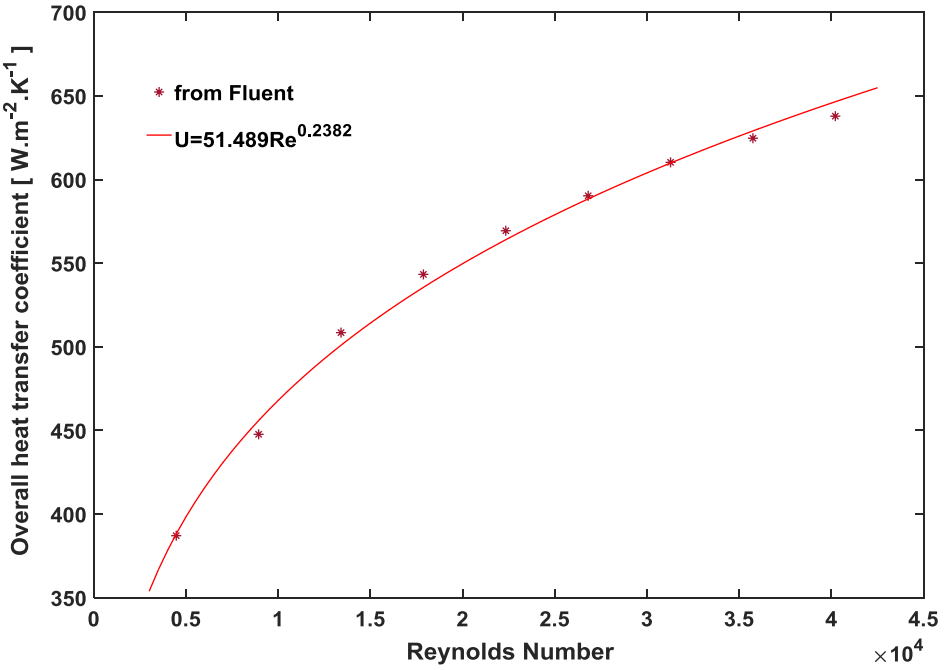

Figure 6-11 Impact on chilled water flowrate on overall Heat Transfer Coefficient

6.4.4 Maximum operating temperature

Figure 6-12 shows the maximum operating temperature inside the irradiation loop varying with the Reynolds number of chilled water. $T_{\max}$ and the Reynolds number curve shows two regimes. In first regime, up to 11.9 $m^3.h^{-1}$ the $T_{\max}$ is more sensitive to change in flowrate. Using three data point a Power Law correlation equation 6.1 was developed to estimate $T_{\max}$ in first regime. From 11.9 $m^3.h^{-1}$ (Re 13403) when the flowrate was increased up to 35.6 $m^3.h^{-1}$, the $T_{\max}$ reduces but the temperature variation is less sensitive to velocity change.

In first regime, at lower flowrates the maximum operating temperature is sensitive to the chilled water flowrate. This is due to low Bi_s and non-optimized wall temperature distribution. However, in second regime as higher flowrates applies high h_e (Bi_s >1), the temperature distribution over the surface of the wall starts optimizing as per natural convection, hence $T_{\max}$ is less sensitive to velocity change.

$$T_{max} = 519.35 \times Re^{-0.041} \qquad \text{for Re < 13403 (6.1)}$$

$$T_{max} = 448.53 Re^{-0.025} \qquad \text{for 13403 < Re < 40208 (6.2)}$$

The irradiation loop must be operated in the second regime (equation 5.4) as in this regime the maximum operating temperature is less sensitive to fluctuation in flowrate. For chilled water flowrate of 19.8 $m^3.h^{-1}$ (Re 22338) the maximum temperature is 74.4 ^{o}C which is a safe temperature for operating

the irradiation loop. Thus, it can be recommended to operate cooling system at the flowrate of 19.8 $m^3.h^{-1}$ (Re 22338) with an inlet temperature of 283 K.

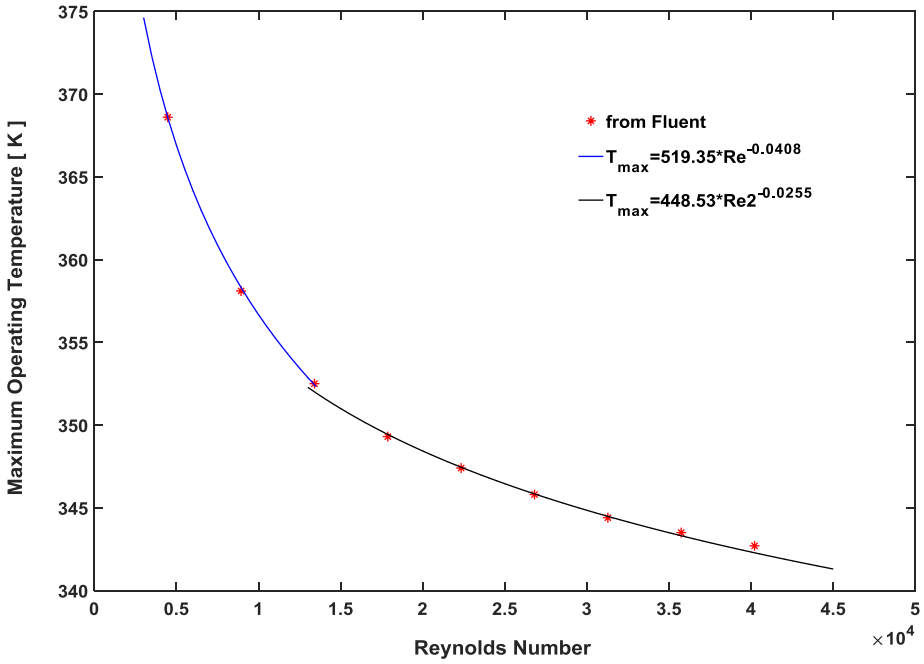

Figure 6-12 Impact of Reynolds number on Maximum operating temperature

6.5 Impact of change in thermal expansion coefficient

In current calculation as the actual thermal expansion coefficient data was not available, water's thermal expansion coefficient at an arbitrary temperature was considered as the thermal expansion coefficient. However, if the thermal expansion factor of uranyl nitrate solutions differs from the assumed value the temperature distribution in the domain will differ from the one estimated.

In the Boussinesq approximation, gravitational force acting on a finite volume in the direction of gravity is proportional to $\beta.\Delta T$. A lower thermal expansion coefficient would mean a lesser driving force for natural convection. The reduced natural convective flow will increase the temperature gradient inside the domain to remove the generated heat. Hence, a study was performed by taking more conservative values of thermal expansion coefficient to check its impact on the maximum operating temperature in the irradiation loop.

For the envisaged operating point of cooling system (chilled water at 283 K and the flowrate 19.8 $m^3.h^{-1}$) setup was modelled by varying the thermal expansion coefficient. During these simulation, all other process condition and the material properties were kept constant. The simulation result has been tabulated in Table 6-6.

As the lower expansion coefficient would reduce the buoyancy effect, maximum operating temperature in the irradiation loop increases with the reduction in thermal expansion coefficient. A correlation between the maximum operating temperature and thermal expansion coefficient was developed (equation 6.4) from the five data points as shown in Figure 6-13 (a).

$$T_{\max} = 265.135 \times \beta^{-0.0357} \qquad (6.4)$$

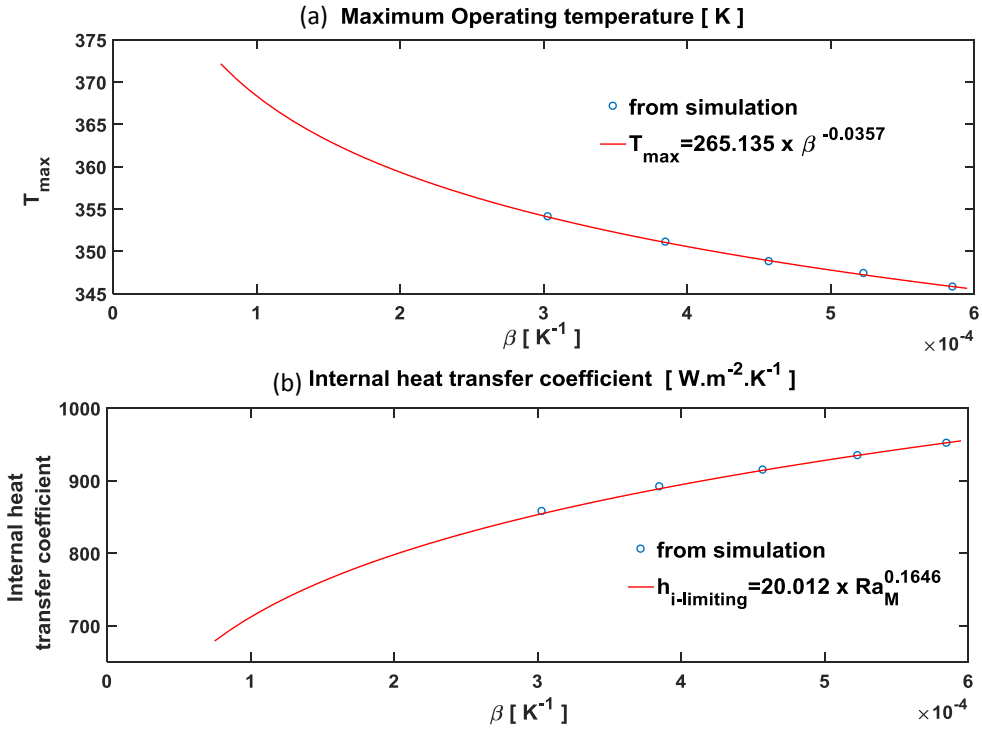

Figure 6-13 Impact of variation in thermal expansion coefficient (a) Maximum temperature in domain (b) Internal heat transfer coefficient

for thermal expansion coefficient of 1.51 x 10^{-4} K^{-1} the maximum operating temperature would rise to more than 90°C. However, such small thermal expansion coefficient factor of uranyl nitrate solution seems unlikely as it is less than the thermal expansion coefficient of pure water at 20 °C (14). In literature, it is generally observed that the thermal expansion coefficient of a liquid increases by addition of polar solutes (23) (24). That means the thermal expansion coefficient of uranyl nitrate solution must be higher than that of water. Hence, even for a conservative β, it could be concluded that the maximum operating temperature will remain below critical temperature for envisaged operating condition of cooling system.

Table 6-6 Simulation result for varying thermal expansion coefficient

β * K^{-1}x 10^{-4}	$T_{\max}$ K	T_h K	T_{wh} K	T_{wc} K	h_{ex} $W.m^2.K^{-1}$	h_i $W.m^2.K^{-1}$
3.03	354.1	317.5	296.2	294.0	1742.5	857.7
3.85	351.1	316.6	296.2	294.0	1738.3	891.7
4.57	348.8	316.0	296.2	294.0	1742.4	914.7
5.2	347.4	315.5	296.1	293.9	1751.7	934.6
5.85	345.8	315.2	296.1	293.9	1751.2	951.7

*Thermal expansion coefficient of water at different temperatures (14)

6.6 Conclusion

As the limitation of 3 hours irradiation time was irrelevant, the irradiation loop setup was redesigned by removing the pump and by connecting the extended lengths of the tube coming out from the left flange of DLDR in a 180^{o} bend. In such assembly, the flow inside the loop will not be controlled by a pump. This new setup was analyzed by computational fluid dynamics and by varying flowrate of chilled water.

In redesigned setup, all the heat generated by nuclear fission reaction and by gamma deposition would be extracted by the cooling system. The fluid in irradiation loop seemed to be following two circulation patterns. One circulation (like in chapter 4's results) where the flow is circulating in zones along the upward or downward sloping heat generation curves and the second circulation along the entire loop in anticlockwise direction.

As the flow was not monitored or restricted by a pump, it was anticipated that the internal heat transfer coefficient for the loop would be higher than the previous setup. However, the Internal heat transfer inside the loop did not change significantly. As the design of cooling system remained the same the overall external heat transfer coefficient also remained the same.

For the studied range of chilled water flowrate (4 to 35.6 $m^3.h^{-1}$), the maximum temperature in the domain reduces with the increasing chilled waters flowrate. For the flowrate of 19.8 $m^3.h^{-1}$ maximum temperature inside the domain is 74.4^{0}C. around this flowrate the maximum temperature appears less sensitive to fluctuations flowrate. Hence an operating flowrate of 19.8 $m^3.h^{-1}$ was envisaged for the system.

Chapter 7

Conclusions and Recommendations

The research carried out in this thesis focused on heat transfer from the Molybdenum-99 production loop placed adjacent to HOR core. The goal of the research was to design a cooling system around the irradiation loop such that the heat produced by nuclear fission would be removed efficiently and the maximum operating temperature inside the irradiation loop would be less than 100 ^{0}C. The research was carried out by computational modelling of the irradiation loop and the cooling system in ANSYS Fluent.

Before computational modelling of the actual system, the system was analyzed using non-dimensional numbers to study the dominating mechanism for heat transfer. The Rayleigh number and Richardson number showed that natural convection would be the dominating mechanism for heat transfer inside the irradiation loop.

Natural convection inside the irradiation loop could be modelled using the Boussinesq approximation. However, any empirical correlation to confirm the modelling result for non-uniform heat generating fluid was not available. Hence, it was decided to model the system with a simple geometry with uniform heat generating fluid such that the natural convection's modelling technique of the Boussinesq approximation could be validated. The result proved that for the operational range of the entire heat generation, natural convection inside the loop can be modelled using the Boussinesq approximation.

Limiting internal heat transfer

The internal heat transfer inside the irradiation loop occurs through natural convection. As natural convection is a responsive process to temperature gradient. Before designing the cooling system, it was decided to design just the irradiation loop with the bell-shaped heat generating curve and varying external heat transfer coefficient, such that the limitation of internal heat transfer could be studied. It was seen that the internal heat transfer does not limit the heat transfer from the irradiation loop. The limiting heat transfer coefficient inside the irradiation loop is 933 W.m^{-2}.K^{-1}.

Heat generation inside the irradiation loop varies with the concentration of uranium. Hence a correlation was developed between the concentration of uranium with the limiting internal heat transfer coefficient with the help of modified Rayleigh Number.

$$h_{i\_\text{limiting}} = 20.012 \times Ra_M^{\,0.1646}$$

Removal of safety barrier

The safety barrier added in the DLDR for protection from any leakage adds additional resistance for removal of heat from the irradiation loop. Moreover, it facilitates heat transfer only by natural convection. As natural convection requires a high temperature gradient between the loop wall and the inner wall of safety barrier, it would increase the temperature at the walls of irradiation loop and eventually will raise the temperature inside loop above boiling point of water. Hence, to facilitate better heat transfer, the safety barrier was removed from the setup.

Cooling system for irradiation loop

The cooling mechanism around irradiation loop was adopted from a shell and tube heat exchanger, such that irradiation loop acts as Tube and the DLDR acts as a shell. Chilled water at 10^{o}C (283 K) is considered as the cooling fluid in DLDR. Chilled water enters the DLDR from a 3'' nozzle near the left flange at the top, and leaves the DLDR from another nozzle near the right flange from the bottom.

From CFD analysis, the effectiveness of the cooling system was studied. As expected, with the increasing flowrate of chilled water, the external heat transfer coefficient increases and temperature of the hot spot inside the irradiation loop decreases. Above 15.8 $m^3.h^{-1}$ of chilled water flowrate, the maximum operating temperature (73.8^{o}C) inside the irradiation loop is less sensitive to flowrate change; hence the operational flowrate of chilled water was envisaged to be 15.8 $m^3.h^{-1}$ or higher.

Redesigned irradiation loop setup

As the initial understanding of 3 hours irradiation time for Molybdenum-99 was irrelevant, the irradiation loop's setup was redesigned by removing the pump and by connecting the extended lengths of the tube coming out from the left flange of DLDR in a 180^{o} bend. In such assembly, the flow inside the irradiation loop will not be controlled by a pump. This new setup was analyzed by computational fluid dynamics and impact of varying flowrate of chilled water was studied.

In new setup, all the heat generated by nuclear fission reaction and by gamma deposition would be extracted by the cooling system. Hence, the overall temperatures inside the new setup is slightly higher than the previous setup. The fluid in the irradiation loop seemed to follow two circulation patterns: one circulation (like earlier setup) where the flow is circulating in zones along the upward or downward slopping heat generation curves, and the second circulation along the entire irradiation loop in anticlockwise direction.

Unlike the earlier setup, the flow in the new setup was not monitored or restricted; hence, it was anticipated that internal heat transfer coefficient in the loop would be higher than the previous setup. However, the internal heat transfer inside the irradiation loop did not improve significantly. For the studied range of chilled water flowrate (4 $m^3.h^{-1}$ to 35.6 $m^3.h^{-1}$), the maximum temperature in the irradiation loop reduces with the increasing chilled waters flowrate. A correlation between the maximum temperature in domain and the external heat transfer coefficient with the Reynolds number of chilled water was established. For the flowrate of 19.8 $m^3.h^{-1}$, the maximum operating temperature inside is 74.4 ^{0}C. Around this flowrate, the maximum temperature appears less sensitive to fluctuations in chilled waters flow. Hence, an operating flowrate of 19.8 $m^3.h^{-1}$ can be envisaged to be an operating flowrate of irradiation loop.

Even though the overall temperature and the maximum operating temperature inside the irradiation loop increased slightly, the overall advantages like removal of the pump and the provision for the removal of gas bubbles lends more advantages to the new design.

7.1 Shortcomings

1) The impact of radiation heat transfer was not studied in this work. The radiation heat transfer from the walls to the cooling fluid would enhance the heat transfer from the irradiation loop.
2) In the current calculation, the neutron flux considered is from the Huisman's work. The neutron flux considered in his study does not consider any interaction of neutrons with the water in

between the DLDR and irradiation loop. Also, the impact of four circulating zones on the rate of reaction and on the ^{99}Mo distribution must be studied.

3) Due to self-shielding effect of uranyl nitrate solution in the irradiation loop, the neutron flux in the z-direction of the setup would reduce. However, for simplicity, in the current calculation it was assumed that the neutron flux over the cross section is uniform.
4) The low irradiation stability of uranyl nitrate produces gas bubbles of H_2, N_2 and NO_x. This will have an impact on the flow and temperature field. However, in current calculation the bubble formation inside the irradiation loop was ignored.

7.2 Recommendations

1) As any empirical correlation for bell shaped heat generation curve was not available. The observed internal circulating flows generated by the bell-shaped heat generation profile and the equation of limiting heat transfer coefficient can be verified by experimental study. The study can be performed on a scaled down replica of irradiation loop and microwaves can be used for internal heat generation.
2) The flowrate of 19.8 $m^3.h^{-1}$ is high, a study can be performed to improve the effectiveness of the cooling system. For example, the impact of surface roughness on external heat transfer coefficient can be studied to reduce chilled waters flowrate. also, smaller baffles at strategic locations can be used to provide higher external heat transfer coefficient at lower flowrates.
3) A study should be carried out for the extraction of ^{99}Mo from the research loop such that the optimum concentration and the rate of solution extract could be studied. The concentration distribution of ^{99}Mo in the entire loop should be studied.
4) Low irradiation stability of uranyl nitrate solution would possibly create gasses like NO_x and NO along with H_2 and O_2. Removal of these gasses from the pressure balancing line must be studied.
5) The irradiation loop system can be operated at elevated pressure to increase the boiling point of aqueous solution for additional margin.
6) A database could be created by experimental study for properties of uranyl nitrate solution for varying pressures and temperature.

Bibliography

1. **National Academies of Sciences, Engineering, and Medicine.** *molybdenum-99-for-medical-imaging.* Washington, DC: : The National Academies, 2016. https://doi.org/10.17226/23563..

2. **OECD.** *An Economic Study of the Molybdenum-99 Supply Chain.* s.l. : NUCLEAR ENERGY AGENCY ORGANISATION FOR ECONOMIC CO-OPERATION AND DEVELOPMENT, 2010.

3. Production and Supply of Molybdenum-99. [Online] 2010. https://www.iaea.org/About/Policy/GC/GC54/GC54InfDocuments/English/gc54inf-3-att7_en.pdf.

4. **Elgin, Kenneth.** *A study of the feasibility of 99Mo production inside the TU Delft Hoger Onderwijs Reactor.* 2014.

5. **J.A.R.Huisman.** *Heat transfer of the mo-99 researsch loop.* 2016.

6. **Chris van Egmond.** *Calculating the interdependency of the temperature and power production inside the Mo-99 research loop.* 2016.

7. **C.C.Pothoven.** *Recirculation of the Mo-99 research loop Predicting the long-term behaviour of the the loop content.* 2016.

8. **J.J. Duderstadt, L.J. Hamilton.** *Nuclear reactor analysis - 1st ed.* . s.l. : John Wiley & Sons, 1976. 978-0471223634.

9. **Hanjalic K., Kenjeres S.,Tummers M.J.,Jonker H.J.J.** *Analysis and Modelling of Physical Transport Phenomena.* s.l. : VSSD Book, 2007. ISBN-13 978-90-6526-165-8,.

10. **Ansys Fluent theory guide.** [Online] https://www.sharcnet.ca/Software/Ansys/16.2.3/en-us/help/flu_th/flu_th.html.

11. **Jiro Mizushima, Sachiko Hayashi, Takahiro Adach.** *Transitions of natural convection in a horizontal annulus.* Japan : Department of Mechanical Engineering, Doshisha University, 2001.

12. **Donald R Pitts, LeightonE,Sissom.** *Theorty and problems of Heat Transfer, second edition, chapter 8.* s.l. : mcgraw hill, 1998.

13. **Deen, William M.** *Analysis of Transport Phenomena.* October 2011. 9780199740253.

14. **L.P.B.M. Janssen, M.M.C.G. Warmoeskerken.** *Transport Phenomena Data Companion.* s.l. : VSSD, 2006. ISBN 90-71301-59-1.

15. **ANSYS Fluent.** Bousinesqs approximation in ansys. [Online] https://www.sharcnet.ca/Software/Fluent6/html/ug/node572.htm.

16. **Kohshi MITACHI, Katsuyuki AOKI, Kenzo KITAMURA, Noritoshi KOMATSU,** *Natural Convection of Heat Generating Fluid within Horizontal Cylinder.***.** s.l. : JSME, 1986.

17. **L. A. Bol'shov, P. S. Kondratenko, V. F. Strizhev.** *Natural convection in heat-generating fluids.* Moscow : Nuclear Safety Institute, Russian Academy of Sciences, 2001.

18. **Boetcher, Sandra K. S.** *Natural Convection Heat Transfer From Horizontal Cylinders -1st ed. Chapter 2.* 2014. 9783319081328.

19. **Warren D. Seider, Daniel R. Lewin, J. D. Seader, Soemantri Widagdo, Rafiqul Gani, Ka Ming Ng.** *Product and Process Design Principles: Synthesis, Analysis and Evaluation, 3rd Edition.* 2009.

20. **zircaloy properties.** [Online] 2014. https://www.atimetals.com/Products/Documents/datasheets/zirconium/alloy/Zr_nuke_waste_disposal_v2.pdf.

21. **meshes, The advantage of Polyhedral.** [Online] https://pdfs.semanticscholar.org/51ae/90047ab44f53849196878bfec4232b291d1c.pdf.

22. converting domian to polyhedral mesh. *Ansys Fluent.* [Online] https://www.sharcnet.ca/Software/Fluent6/html/ug/node187.htm.

23. **Green, Don W. and Perry:, Robert H.** *Perry's Chemical Engineers' Handbook, Eighth Edition. THERMAL EXPANSION.* s.l. : McGraw-Hill Professional, 2008 1997 1984 1973 1963 1950 1941 1934.

24. Engineering ToolBox, (2009). Volumetric or Cubical Expansion Coefficients of Liquids. [Online] : https://www.engineeringtoolbox.com/cubical-expansion-coefficients-d_1262.html.

25. **Bhutta, Muhammad Mahmood Aslam.** *CFD applications in various heat exchangers design: A review.* s.l. : Department of Mechanical Engineering, University of Engineering & Technology, Lahore, Pakistan.

26. **Nicholas D. Francis, Jr., Michael T. Itamura, Stephen W. Webb, and Darryl L. James.** *CFD Calculation of Internal Natural Convection in the Annulus between Horizontal Concentric Cylinders.* s.l. : Sandia National Laboratories, 2002.

27. **Daniel Milian Pérez, 1 Daniel E. Milian Lorenzo.** *Thermal-Hydraulics Study of a 75 kWth Aqueous Homogeneous Reactor for 99Mo Production.* 2015.

28. **Bolshov, L.A., Arutyunyan, R.V., Popkov, A.G., Chudanov, V.V., Vabishchevich, P.N., & Churbanov, A.G.** *Numerical study of natural convection of a heat-generating fluid in nuclear reactor safety problems* . s.l. : International Atomic Energy Agency (IAEA), 2004.

Appendix

A. MATLAB Code of Numerical solution using the empirical correlation

```
clc;
clear;
K=[0.01 0.1 0.5 1 2 5];
Cp=4182;
% vary the matrix index of K to change the heat generation
Hv=1644173.0*K(1);
k=0.6;
rho=990.15;
Mu=0.000596;
nu=Mu/rho;
g=9.81;
B=0.00042; % thermal expansion coefficient
Di=0.044; % in m
a=k/rho/Cp;
fi=4.43203703703704E-07;
c=0.53;
n=(1/4);
Twater=300; % surrounding temperature
alfa=Hv*3.14*Di^2/rho/Cp/fi/4; % constant found by simplifying equation
beta=3.14*k*c/rho/Cp/fi*(g*B*Di^3/nu/a)^n; % constant found by simplifying
equation
X=k*c/Di*(g*B*Di^3/nu/a)^n;
Tzero=300;  % mean temperature at x=0 m
Zspan= [0 1.0];
h0=10000; % extrenal heat transfer coefficent

f1=@(z,Tm,Twall) (alfa-(3.14*Di/rho/Cp/fi*(Tm-Twater)*(1/h0+(X*(Tm-
Twall)^n)^-1)^-1));    %first derivative of f(x)
a1=0;               %initial value
b1=1;                %final value

% solving using Explicit function
he=0.001;                   % step size for explicit
Ne= abs(a1-b1)/he;          % number of cycles as per step s
ze=(a1:he:b1);              % number of cycles as per step s
[r1,k1]=size(ze);
Tm=zeros(r1,k1);
Twall=zeros(r1,k1);
Tm(1,1)=300;              % initial value of function
Twall(1,1)=300;           % temperature of the wall at x=0m
 for j=1:Ne
     Tm(j+1)= Tm(j)+f1(ze(j),Tm(j),Twall(j))*he;
     for i=1:1000
    Twa(j+1)= (Tm(j+1)-Twater)*((1/h0+(X.*(Tm(j+1)-Twall(j+1))^n)^-1)^-
1)/h0+Twater;
    error=Twa(j+1)-Twall(j+1);
    Twall(j+1)=Twa(j+1);
    if abs(error)<0.000001
```

```
        break
    end
    i=i+1;
     end
 end
 dt=Tm-Twall;

plot(ze,Tm,ze,Twall);
title ('Temperature profile in tube');
legend('Cup mean temperature', 'Wall Temperature');
xlabel('axial length of pipe in m');
ylabel( 'Temperature in K');

for j=1:Ne
Ra(j)=(g*B*(Tm(j)-Twall(j))*Di^3/nu/a);
NU(j)=c*Ra(j).^n;
hi(j)=NU(j).*k/Di;
end
```

Appendix

B. MATLAB Code of density Calculation

Following MATLAB code was taken from J.A.R. Huisman thesis research work

```
clc;
clear all;
ConU=310*1.1;
mp235=19.95;
mp234=8.44e-3*mp235-7.0084e-4;
mp238=100-mp235-mp234;
w234=mp234/100;
w235=mp235/100;
w238=mp238/100;

Na=6.0221e23;
A234=234.0409522088;
A235=235.0439299;
A238=238.05078825;
rhoFuel=2.807;

B234=234+8*15.994+2*14.0067;
B235=235+8*15.994+2*14.0067;
B238=238+8*15.994+2*14.0067;

N234=(Na*(w234*ConU)/A234)/1000;
N235=(Na*(w235*ConU)/A235)/1000;
N238=(Na*(w238*ConU)/A238)/1000;

mFuel=(((N234*B234)/Na)+((N235*B235)/Na)+((N238*B238)/Na))*1000;

vFuel=mFuel/rhoFuel;
vWater=1000-vFuel;

rhoavg=(rhoFuel*vFuel+vWater)/(vFuel+vWater)
rhowater=0.998;
Massfuel=mFuel/(mFuel+vFuel*rhowater)*100;
```

Appendix

C. MATLAB Code of specific heat

Following MATLAB code was taken from J.A.R. Huisman thesis research work

```
clear all;
close all;
clc;
y=[0.894 .759 .757 .646 .573 .574 .583 .530 .542 .493 .521 .513]*4.184;
x=[11.8 25.9 26.2 39.3 46.75 47.2 47.4 52.4 52.7 55.5 55.6 56.0];
ConU=310*1.1;
m=ConU/(238/(238+8*15.994+2*14.0067));
mp=(m/(m+1000))*100;
P=polyfit(x,y,1);
Heatcapacity=(P(1)*mp+P(2))
x2=[0:0.1:60];
y2=(P(1)*x2+P(2));
hFig = figure(1);
set(hFig, 'Position', [300 200 800 550])
plot(x,y,'+',x2,y2,'r')
a(1)=xlabel('Masspercentage uranium');
a(2)=ylabel('Cp [J/gK]');
a(3)=title('Heat capacity Cp v. UO3(NO3)2 salt concentration');
a(4)=legend('Data from Literature,Linear Fit');
set(a,'Interpreter','latex','fontsize',12);
set(a(3),'Fontsize',12)
```

Appendix

D. User defined function for heat source

User defined function (UDF) is a function used to enhance standard capability of the Fluent solver. UDF's are written in C programming language. UDF's are created using defined macros supplied by Fluent Inc. depending upon function different macros are used. In current simulation for nuclear fission heat and gamma deposition heat, "source" macro and for flux from water pool "boundary condition" macro is used. Depending upon the macro defined, UDFs are called at different position in the solver's algorithm. For example, the energy source term UDF would be called before solving the energy equation such that changes in energy generation over time or over space could be accommodated in the solution. Following three UDFS were used in Fluent.

Heat source term in the irradiation loop

The heat generation by nuclear fission is incorporated as an energy source term, in the uranyl nitrate solution's fluid domain. While defining the heat generation over the irradiation loop it was assumed that the heat generation over the cross section of the irradiation loop normal to x-axis is uniform. and the volumetric heat generation inside the irradiation loop is varying only in the x-direction. Figure D-1 shows the bell-shaped heat generation curve defined in irradiation loop. In the UDF depending upon concentration of uranium the proportionality constant K was varied. For 310 $gU.L^{-1}$ uranium concentration K=1.

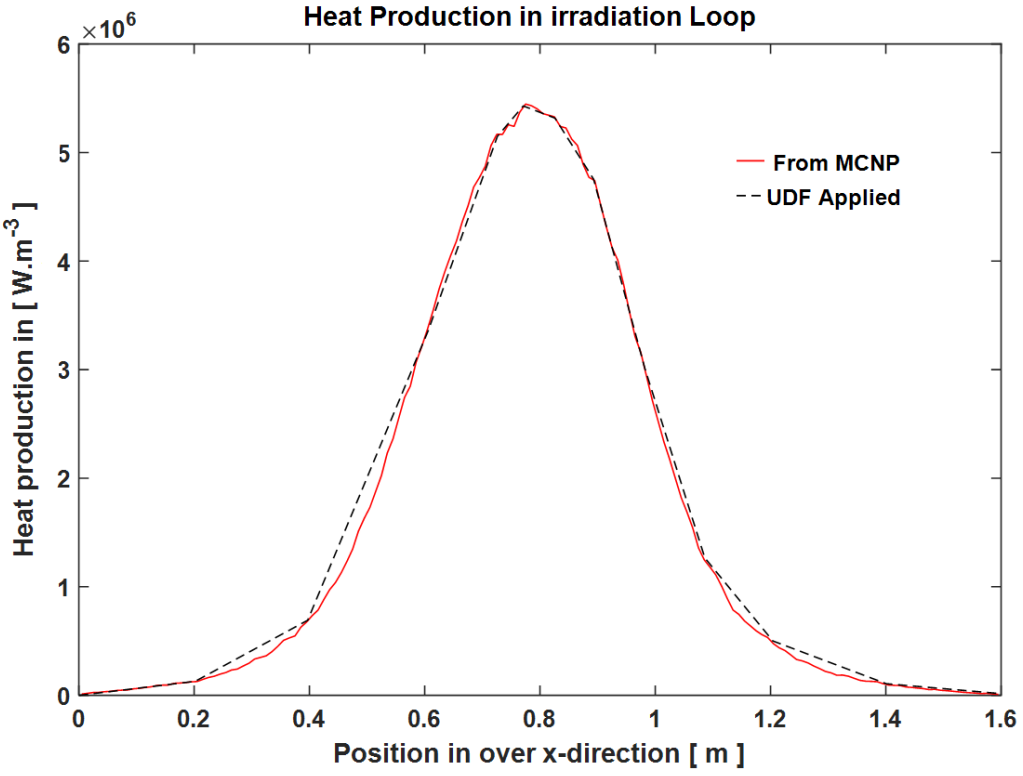

Figure D-1 heat production profile in irradiation loop incorporated in Fluent

UDF incorporated in Fluent

```
DEFINE_SOURCE(heat_source, c, t,a1,a2)
{
real x[ND_ND];
real source,pos_x,K;
C_CENTROID(x, c, t);
pos_x = x[0];
K=1.0;
if (pos_x <0.0)
source =0;
else if (pos_x <(0.2819))
source =(628408*pos_x+0)*1.02*K;
else if (pos_x < (0.557343453510436))
source =(2822396*pos_x-442961)*1.02*K;
else if (pos_x < (0.686072106261859))
source =(12526820*pos_x-4298950)*1.02*K;
else if (pos_x < (0.80561669829222))
source =(14673771*pos_x-5600157)*1.02*K;
else if (pos_x < (0.851157495256167))
source =(6056391*pos_x+652757)*1.02*K;
else if (pos_x < (0.906185958254269))
source =(-2004874*pos_x+6869263)*1.02*K;
else if (pos_x < (0.972599620493358))
source =(-8305908*pos_x+12075088)*1.02*K;
else if (pos_x < (1.06178368121442))
source =(-19174277*pos_x+21776190)*1.02*K;
else if (pos_x < (1.16614800759013))
source =(-16385291*pos_x+19038010)*1.02*K;
else if (pos_x < (1.28379506641366))
source =(-6376794*pos_x+8167300)*1.02*K;
else if (pos_x < (1.48113851992409))
source =(-1956680*pos_x+2846389)*1.02*K;
else
source =(-451583*pos_x+737540)*1.02*K;
return source;
}
```

Heat source term in the Tube wall:

The heat deposited by gamma radiation over the tube wall is incorporated as an energy source term in domain-2 (tube wall). Like fission heat gamma heating is assumed uniform in y and z direction and is considered to vary only in x-direction. Figure D-2 gives the profile of heat deposited by gamma radiation on to the Zircaloy wall of irradiation loop. zircol

UDF incorporated in Fluent

```
DEFINE_SOURCE(gamma_heat, c, t,a1,a2)
{
real x[ND_ND];
```

```
real source,pos_x;
C_CENTROID(x, c, t);
pos_x = x[0];
rho=6500000;
if (pos_x <0.0)
source =0;
else if (pos_x <(0.132682927))
source =(0.073553599*pos_x+0.005)*rho;
else if (pos_x < (0.407804878))
source =(0.223958333*pos_x-0.015)*rho;
else if (pos_x < (0.655609756))
source =(0.769095783*pos_x-0.237)*rho;
else if (pos_x < (0.735609756))
source =(0.599506579*pos_x-0.126)*rho;
else if (pos_x < (0.784390244))
source =(0.214967105*pos_x+0.157)*rho;
else if (pos_x < (0.84097561))
source =(-0.163594601*pos_x+0.454)*rho;
else if (pos_x < (0.889756098))
source =(-0.526809211*pos_x+0.759)*rho;
else if (pos_x < (1.00488))
source =(-0.880895963*pos_x+1.074)*rho;
else if (pos_x < (1.18829))
source =(-0.632121361*pos_x+0.825)*rho;
else if (pos_x < (1.36585))
source =(-0.252774364*pos_x+0.374)*rho;
else
source =(-0.09797335*pos_x+0.162)*rho;
return source;
}
```

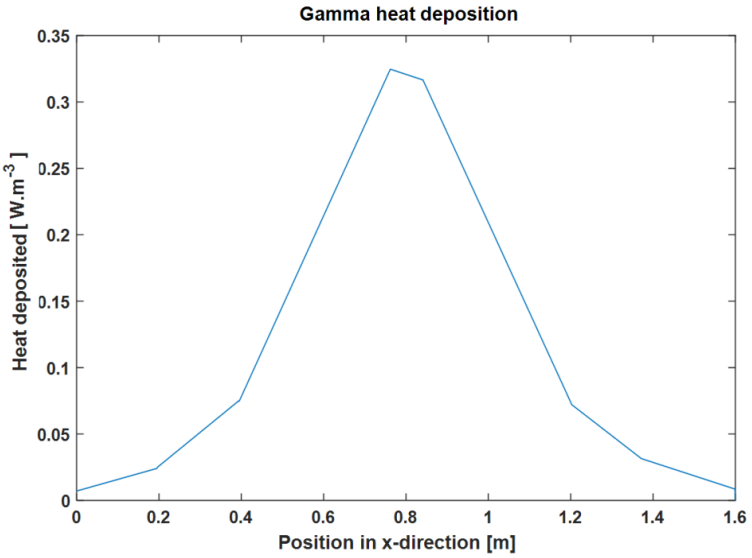

Figure D-2 Gamma heat deposition incorporated over tubewall

Flux from the DLDR wall:

The gamma heat deposition and the temperature difference from the surrounding these two factors contributes into influx of heat to the cooling fluid from DLDR wall. Instead of modelling the DLDR wall as different domain. The heat flux from the wall is simulated as boundary conditions to the domain-3 of coolant.

Temperature at DLDR and water pool interface = 290 K (Assumed)
Temperature of liquid water pool = 313 K
It was assumed that the Landers empirical correlation for calculating heat a transfer coefficient over a horizontal pipe is valid to calculate heat transfer rate. (18)

$$Nu = 0.12 \times (Ra_w)^{0.25}$$

$$Nu = hl / k = 0.12 \times (Ra_w)^{0.25}$$

$$Ra = \frac{g\beta(T_b - T_w)D^3}{\nu\alpha} = 2.35 \times 10^9$$

Based on which the flux from the neighboring water pool is approximately 15 kW.m^{-2}.

UDF incorporated in Fluent

```
DEFINE_PROFILE(flux_profile,t,i)
{
real x[ND_ND]; /* this will hold the position vector */
real pos_x;
face_t f;
begin_f_loop(f,t)
{
F_CENTROID(x,f,t);
pos_x = x[0];
if (pos_x <0.0)
F_PROFILE(f, t, i) =0;
else if (pos_x <(0.132682927))
F_PROFILE(f, t, i) =((0.073553599*pos_x+0.005)*2986.73)+15000;
else if (pos_x < (0.407804878))
F_PROFILE(f, t, i) =((0.223958333*pos_x-0.015)*2986.73)+15000;
else if (pos_x < (0.655609756))
F_PROFILE(f, t, i) =((0.769095783*pos_x-0.237)*2986.73)+15000;
else if (pos_x < (0.735609756))
F_PROFILE(f, t, i)=((0.599506579*pos_x-0.126)*2986.73)+15000;
else if (pos_x < (0.784390244))
F_PROFILE(f, t, i) =((0.214967105*pos_x+0.157)*2986.73)+15000;
else if (pos_x < (0.84097561))
F_PROFILE(f, t, i)=((-0.163594601*pos_x+0.454)*2986.73)+15000;
else if (pos_x < (0.889756098))
F_PROFILE(f, t, i) =((-0.526809211*pos_x+0.759)*2986.73)+15000;
else if (pos_x < (1.00488))
F_PROFILE(f, t, i)=((-0.880895963*pos_x+1.074)*2986.73)+15000;
```

```
else if (pos_x < (1.18829))
F_PROFILE(f, t, i) =((-0.632121361*pos_x+0.825)*2986.73)+15000;
else if (pos_x < (1.36585))
F_PROFILE(f, t, i) =((-0.252774364*pos_x+0.374)*2986.73)+15000;
else
F_PROFILE(f, t, i) =((-0.09797335*pos_x+0.162)*2986.73)+15000;
}
end_f_loop(f, t)
   }
```

Appendix

E. Specific Biot Number

For an internal heat generating system with natural convection, Specific Biot number can be defined as the ratio of external heat transfer coefficient to the limiting internal heat transfer coefficient.

$$Bi_S = \frac{h_e}{h_{i\_\text{limiting}}}$$

Natural convection is a function of temperature gradient; however, the temperature gradient depends upon the heat generation rate and the resistance to heat transfer. There seems to be a correlation of specific Biot number with the development of natural convection inside the liquid domain.

Equation E.1 is valid for any heat generating closed system in a steady state.

$$H_v.V = h_i(T_h - T_w) = h_e(T_w - T_c) \qquad \text{(E.1)}$$

For heat generating system the optimization of natural convection would follow following regimes: -

1) $Bi_S >> 1$

   In this case, the limiting heat transfer coefficient is low compared to the external heat transfer coefficient. Which would mean the external heat transfer coefficient would not demand high wall temperature. However, inside the fluid domain, natural convection would demand certain temperature gradient to dissipate heat produced. And the natural convection would configure temperature distribution over the wall. in such case as the wall temperature is decided by the internal natural convection, hence the wall temperature would be set such that the natural convection is optimized.

2) $Bi_S \leq 1$

   In this case the specific Biot number is low that means the external heat transfer coefficient is low and It would demand higher wall temperature from the outside to transfer the heat produced. This situation is not ideal as in such case natural convection does not govern the temperature distribution over the interface and natural convection will not be able to optimize to its full potential.

This could be clearly observed in Figure 4-8.

A cooling mechanism for a heat generating fluid must be designed to operate at Bi_S >1 , such that the natural convection is optimized to its full potential.

Appendix

F. Selection of turbulence model

The whole setup of irradiation loop consists of two fluid domains. The internal domain of uranyl nitrate solution and the external domain of chilled water. During simulation as both flows will be modelled simultaneously, the numerical modeling technique should be able to model both fluids accurately.

Buoyant flow inside a horizontal cylinder remains laminar up to a Rayleigh number of 10^9 (18). i.e. the fluid flow of uranyl nitrate solution would be laminar till the Rayleigh number is below 10^9. For the setup, even if the temperature difference between the bulk fluid and the wall temperature reaches 90 ^{0}C the Rayleigh number of uranyl nitrate solution remains less than 10^9. Hence, for all the operating range envisaged in the irradiation loop the flow inside it would be Laminar.

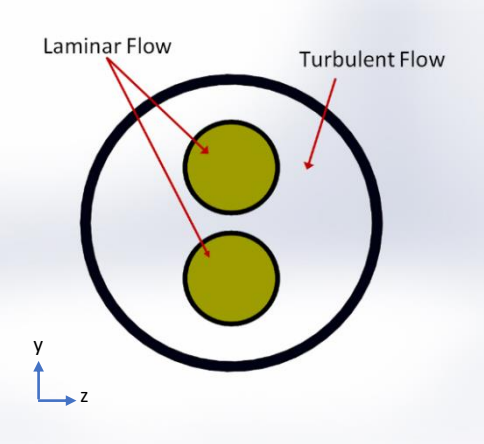

Figure F-1 cross section of setup

However, to achieve the required external heat transfer coefficient, it is envisaged that the flow of chilled water flowing over the surface of irradiation loop Is turbulent in nature. Hence, it was necessary to use turbulent modelling in the entire setup. As the entire setup resembles, a shell and tube type heat transfer device literature survey was carried out to check which turbulence models can simulate turbulent flow of chilled water in DLDR (shell). Mahmood Aslam Bhutta and Nasir Hayat (2011) identified different turbulent models which can simulate heat transfer and flow of a shell and tube heat exchanger effectively (25). In this paper, it is concluded that two equation RANS (Reynolds-averaged Navier-Stokes equation) model (such as RNG k-ε, standard k-ε) with different wall functions can predict the turbulent flow effectively. Hence, a study was carried out with these turbulent models to check its applicability to simulate natural convective (laminar) flow inside the irradiation loop.

Simulation from chapter 3 (Case 4: q''' =1,644,173 W.m-3) was carried out with different turbulence model's & wall functions. The velocity profile's over the vertical line from Figure 3-7(b) were plotted for all simulations. As it can be seen in figure above the RNG k-ε model seems to predict the natural convective flow most effectively, as its profile overlaps with the laminar velocity profile.

Nicholas D. Francis, Jr. and Michael T. Itamura carried out CFD calculation of internal natural convection in the annulus between horizontal concentric cylinders (26). They also suggest the use of RNG k- ε turbulence model for modelling natural convective flow in a horizontal pipe. As most of the critical activity in natural convection is carried out in the near wall region, in their research work they suggest using differential viscosity term in the RNG k-ε equation's. Hence, the differential viscosity term was used with the RNG k-ε model for the given study. Also, as suggested in ANSYS theory guide the "full buoyancy effect" term was activated to add the buoyancy term in the transfer rate (ε) equation.

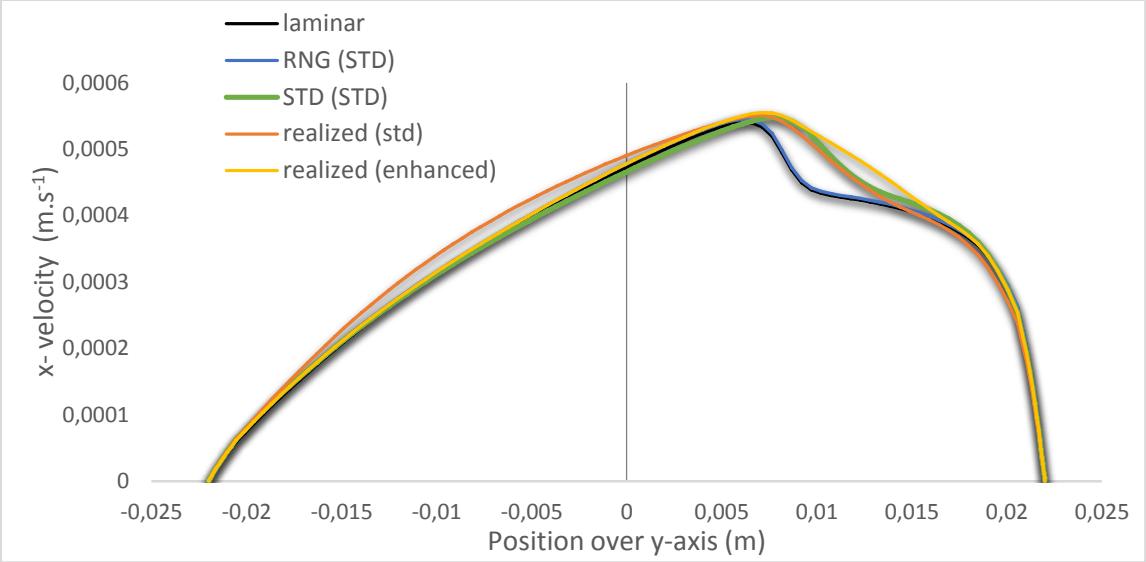

Figure F-2 Comparison of x-velocity for different turbulence model with laminar flow

As the renormalized (RNG) k-ε (RANS) model is appropriate for both internal uranyl nitrate solution's buoyant flow and external chilled waters turbulent flow, it was decided to use RNG k- ε turbulent model for all the simulations carried out in chapter 5 and chapter 6.